First Measurements of Transverse Spin Asymmetries through Single Pion Production at the COMPASS Experiment

To the Faculty of Natural Sciences
of the Friedrich-Alexander-Universität Erlangen-Nuremberg
to obtain the title
"Dr Rer. Nat."

Submitted by
Richard Webb
from Maidstone (Kent) /England

Approved as dissertation by the Faculty of Natural Sciences
of the University of Erlangen-Nuremberg

Date of oral examination:	10th May 2004
Chairman of the Examining Board:	Prof. Dr L. Dahlenburg
First Marker:	Prof. Dr W. Eyrich
Second Marker:	Prof. Dr E. Steffens

Abstract

The COMPASS Experiment, which started running at the European Centre for Nuclear Research, CERN, in Geneva in 2001, is investigating in a wide-ranging programme the spin structure of the nucleon through deep-inelastic scattering (DIS). The experiment possesses a polarised muon beam and a polarised deuterium target, which together allow access to all terms of the polarised DIS cross-section. Two of the most important functions which COMPASS is designed to fulfil are a precision measurement of the gluon polarisation ΔG and the investigation of the transverse polarised quark distribution functions $\Delta_T q_i$. This thesis firstly describes a contribution made to the building and characterisation of hodoscopes made of scintillating fibres in the immediate beam-region of the COMPASS spectrometer. These detectors are indispensible for the detection of muons scattered under very small angles, of importance especially for the measurement of ΔG. Secondly this thesis presents first results from the analysis of transverse spin asymmetries in single pion production (the Collins effect), which should provide access to $\Delta_T q$.

Contents

Chapter 1

Introduction - Physics Motivation

Ever since it became clear in the mid 1960s that protons and neutrons, which up until that point had been regarded as the fundamental, indivisible constituents of the atomic nucleus, exhibit characteristics pointing to their having a structure, the inner life of the nucleon has been the subject of intensive investigation. The currently most successful model of the nucleon structure is given by the field theory of Quantum Chromodynamics (QCD). According to this picture, a protons or neutron consists of three *valence quarks*, particles with one-third integer charge and spin $\frac{1}{2}$, which make up the charge of the nucleon. These are surrounded by a "sea" of further quarks and *gluons* which is in a continuous state of flux. The gluons are in the QCD model the vector bosons of the strong nuclear interaction.

A particularly instructive means of investigating the structure of the nucleon is the deep-inelastic scattering (DIS) of a lepton on a nucleon target. Whilst unpolarised DIS has been extensively studied in the course of the last few decades, many open questions remain in the case of polarised beam and target. In particular, results from the EMC collaboration at CERN in Geneva at the end of the 1980s indicated a contribution of the valence quarks to the total spin of the nucleon significantly below that demanded by theoretical predictions. This *spin crisis* spurred further experimental and theoretical investigations in an attempt to find the missing component of the nucleon spin. Alongside the orbital angular momentum, current interest is focussed on a possible contribution from gluon polarisation, signified as ΔG. The COMPASS[1] Experiment at CERN has been designed to enable a first precision measurement of ΔG. A further – as yet unknown – quantity is the set of transverse quark spin or *transversity* distributions, $\Delta_T q_i(x)$. Their measurement is also one of the main goals of COMPASS.

The theoretical background to the physics investigated by the COMPASS experiment is presented in Chapter 2 of this thesis. Along with a general con-

[1] **Co**mmon **M**uon and **P**roton **A**pparatus for **S**tructure and **S**pectroscopy

sideration of the kinematics and cross-sections of deep-inelastic scattering, the essential features of the parameterisation of the nucleon structure in the naïve and QCD-extended Quark Parton Models are discussed. The background to the gluon-polarisation and transversity measurements at COMPASS is also elucidated.

The COMPASS experiment itself is situated on the M2 beamline of the Super Proton Synchrotron (SPS) at CERN. A polarised 160 GeV μ^+ beam and a polarised ^6LiD target make all terms of the DIS cross-section accessible. Details of this beam and target, and of the COMPASS spectrometer and data acquisition system are presented in Chapter 3.

Chapter 4 is concerned with the work on COMPASS hardware done as part of this thesis. This consisted of a contribution to the building of scintillating-fibre hodoscopes to detect minimally deflected muons. The reliable detection of scattered leptons in the low Q^2 range is essential in order to ascertain ΔG accurately. Very good temporal and good spatial resolution, as well as high-rate capability are required of the detector. The important characteristics of these hodoscopes and their performance are dealt with in this chapter.

A contribution was also made as part of the work described in this thesis to the extraction of the first transverse spin asymmetries from COMPASS data. This was achieved through analysis of single pion production with transverse target polarisation (the *Collins effect*). This analysis is presented in chapter 5. A summary and outlook complete this thesis.

The work described in this thesis was performed in close collaboration between the research groups of Prof. W. Eyrich at the Friedrich-Alexander-Universität Erlangen-Nuremberg und Prof. J. Bisplinghoff at the Helmholtz Institut for Nuclear and Radiation Physics (ISKP) at the University of Bonn. In the course of the transversity analysis a fruitful collaboration with members of the research group of Prof. F. Bradamante at the Italian National Insitute for Nuclear Research (INFN) in Trieste was established.

Chapter 2

Theoretical Background

2.1 Kinematics of Deep-Inelastic Scattering

2.1.1 Inclusive DIS

In inclusive[1] deep-inelastic scattering (DIS) experiments, an incoming beam lepton $\vec{l}$ with four-momentum $k = (E, \vec{p})$ scatters off a target nucleon $\vec{N}$ at rest (Mass M, four-momentum $P \overset{\text{lab}}{=} (M, 0, 0, 0)$) (Figure 2.1). If the beam lepton or target nucleon is polarised, its spin vector is described by $\vec{s}$ or $\vec{S}$ respectively:

$$\vec{l}(k, \vec{s}) + \vec{N}(P, \vec{S}) \rightarrow \vec{l'}(k', \vec{s'}) + X \tag{2.1}$$

The lepton loses part of its energy to the nucleon and continues past with a reduced four-momentum k' (energy E') at an angle of deflection θ. The *a priori* unknown hadronic end-product is indicated by X; if its invariant mass is above the energy range of the nuclear resonances, the scattering event is regarded as a deep-inelastic process.

A series of Lorentz invariables, based on the known kinematic variables of the particles involved, is defined in connexion with a deep-inelastic scattering process [1, 2]:

$$Q^2 \quad := \quad -q^2 = -(k - k')^2 \overset{\text{lab}}{\approx} 4EE'sin^2\left(\frac{\theta}{2}\right) \tag{2.2}$$

$$P \cdot k \quad \overset{\text{lab}}{=} \quad ME \tag{2.3}$$

$$P \cdot q \quad \overset{\text{lab}}{=} \quad M(E - E') := M\nu \tag{2.4}$$

The approximation in (2.2) relates to the assumption of a lepton mass which is negligible in comparison to its momentum. At the COMPASS experiment, with its 160 GeV μ^+ beam, the ratio $m_\mu/p_\mu \approx 0.0007$ validates this assumption for almost all purposes. The relationships in the laboratory system in (2.2) to

[1] A scattering event in which only the scattered particle itself is detected is called an *inclusive* event. If the complete (hadronic) end-product is also measured, the event is *exclusive*. If the hadronic end-product is only partially reconstructed, the measurement is *semi-inclusive*. This last case, which applies at COMPASS, is dealt with explicitly in Section 2.1.2.

(2.4) apply where the initial nucleon four-momentum reduces to its mass (i.e., for a fixed target).

In the energy range covered by COMPASS ($Q^2 < 10^3$ (GeV/c)^2), the lepton-nucleon interaction can be described fully in terms of the electromagnetic force [2]. Q^2 is in this case the negative squared four-momentum of the exchanged virtual photon; $\nu = E - E'$ is its energy. The deep-inelastic regime is generally taken as having $Q^2 > 1$ (GeV/c)^2.

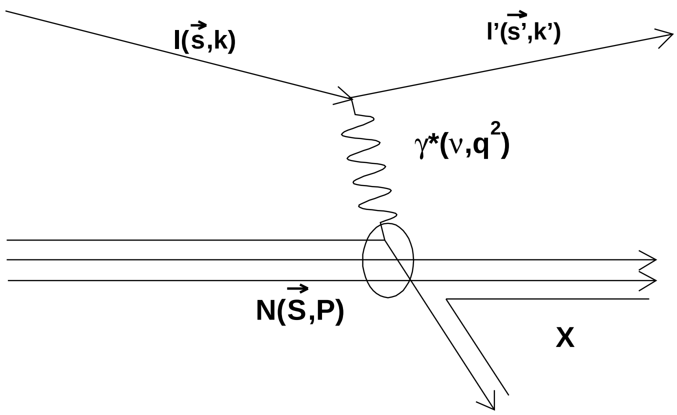

Figure 2.1: Schematic representation of a deep-inelastic scattering process. A lepton l with spin $\vec{s}$ and four-momentum k scatters on a nucleon N ($\vec{S}, P$). A virtual photon γ^* is exchanged with four-momentum q and energy ν. The *a priori* unknown hadronic end-product is indicated by X.

Starting from the Lorentz invariables introduced above, two dimensionless quantities x and y may be defined:

$$x := \frac{Q^2}{2P \cdot q} \stackrel{\text{lab}}{=} \frac{Q^2}{2M\nu} \qquad 0 \le x \le 1 \tag{2.5}$$

$$y := \frac{P \cdot q}{P \cdot k} \stackrel{\text{lab}}{=} \frac{\nu}{E} \qquad 0 \le y \le 1 \tag{2.6}$$

The *Bjørken scaling variable*, x, can be regarded as a measure of the elasticity of a process ($x = 0$ totally inelastic, $x = 1$ elastic). In the Quark Parton Model to be introduced in Section 2.4, x is also interpreted as the fraction of the nucleon momentum carried by the quark struck in the scattering process. y describes the fractional energy transfer via the exchanged photon. Two further important quantities in DIS are the centre-of-mass energy $\sqrt{s}$ and the mass of the hadronic end-product W, whose squares are given by

$$s = (k+P)^2 = \frac{Q^2}{xy} + M^2 \quad (2.7)$$

$$W^2 = (q+P)^2 = \frac{1-x}{x}Q^2 + M^2 \quad (2.8)$$

A complete description of an inclusive DIS process is given by any two of the Lorentz-invariant quantities described above. A common choice, for example in the parameterisation of the nucleon structure functions introduced in Section 2.2, is the pair x and Q^2.

2.1.2 Extension to Semi-Inclusive Processes

The kinematics introduced in the previous section describe inclusive DIS, where the hadronic end-product X is not observed. The COMPASS spectrometer allows the detection of at least part of this end-product: a *semi-inclusive* measurement is performed. The reaction formula (2.1) is augmented to

$$\vec{l}(k, \vec{s}) + \vec{N}(P, \vec{S}) \rightarrow \vec{l'}(k', \vec{s'}) + \vec{h}(P_h) + X \quad (2.9)$$

where $\vec{h}$ is the observed hadronic end-product with four-momentum P_h (energy E_h). P_h represents an additional independent kinematic variable with the help of which two further Lorentz invariables can be constructed. In addition to Q^2, $P \cdot k$ and $P \cdot q$,

$$P \cdot P_h \stackrel{\text{lab}}{=} ME_h = M\nu z \quad (2.10)$$

$$q \cdot P_h \stackrel{\text{lab}}{=} \nu E_h - \vec{q} \cdot \vec{P_h} \quad (2.11)$$

may be defined. For a complete description of a semi-inclusive process, a third scaling variable z is also introduced, which describes the proportion of the photon energy carried by the hadron:

$$z := \frac{P \cdot P_h}{P \cdot q} \stackrel{\text{lab}}{=} \frac{E_h}{\nu} \qquad 0 \leq z \leq 1 \quad (2.12)$$

Using this identity, (2.11) can also be parameterised in terms of the mass of the hadronic end-product m_h and its transverse momentum [3]:

$$\begin{aligned} q \cdot P_h &\stackrel{\text{lab}}{=} \nu^2 z - |\vec{q}||\vec{P_h}|cos\theta_h \\ &= \nu^2 z - |\vec{q}|\sqrt{(z\nu)^2 - m_h^2 - p_{h\perp}^2} \quad (2.13) \end{aligned}$$

2.2 The Deep-Inelastic Cross-Section

The general expression for the differential inclusive DIS cross-section can be written as a product of a leptonic tensor $L_{\mu\nu}$ and a hadronic tensor $W_{\mu\nu}$

$$\frac{d^3\sigma}{dxdyd\varphi} = \frac{y\alpha^2}{2Q^4} L_{\mu\nu} W^{\mu\nu} \tag{2.14}$$

where α is the electromagnetic fine structure constant. This reflects the fundamental assumption in quantum electrodynamics (QED) that such scattering processes can be decomposed into two independent sub-processes: the radiation of the virtual photon by the lepton, and the subsequent absorption of this photon by the nucleon. The leptonic tensor can in QED be represented by the summed linear combination of all kinematic variables as

$$\begin{aligned} L_{\mu\nu} &= 2\left(k_\mu k'_\nu + k_\nu k'_\mu - g_{\mu\nu}(kk' - m^2) + im\epsilon_{\mu\nu\lambda\sigma} q^\lambda s^\sigma\right) && (2.15) \\ &= L^{(S)}_{\mu\nu}(k, k') + iL^{(A)}_{\mu\nu}(k, k', s) && (2.16) \end{aligned}$$

where $g_{\mu\nu}$ is the metric tensor, $\epsilon_{\mu\nu\lambda\sigma}$ the totally asymmetric Levi-Civita tensor, and m is lepton mass. $L_{\mu\nu}$ splits itself through the summation into a symmetric, real term and an anti-symmetric, imaginary term (superscripts $^{(S)}$ and $^{(A)}$ respectively in (2.16)). $L^{(S)}_{\mu\nu}$ is spin-independent; $L^{(A)}_{\mu\nu}$ depends on the lepton spin s.

Since, unlike the leptonic tensor, the hadronic tensor $W_{\mu\nu}$ does not describe an elementary particle, but rather a particle with a *a priori* unknown internal structure, there is no generalised expression for it. The hadronic tensor is parameterised with the help of four initially equally unknown *structure functions*, F_1, F_2, g_1 and g_2 [2], which depend on the kinematic variables x and Q^2 and whose exact functional form must be established:

$$\begin{aligned} W_{\mu\nu} &= 2\Bigg[F_1(x,Q^2)\left(-g_{\mu\nu} + \frac{q^\mu q^\nu}{q^2}\right) + \frac{F_2(x,Q^2)}{Pq}\left(P^\mu - \frac{Pq}{q^2}q^\mu\right)\left(P^\nu - \frac{Pq}{q^2}q^\nu\right) \\ &+ i\frac{M}{Pq}\epsilon^{\mu\nu\lambda\sigma} q_\lambda \left(g_1(x,Q^2)S_\sigma + g_2(x,Q^2)(S_\sigma - \frac{Sq}{Pq}P_\sigma)\right)\Bigg] && (2.17) \\ &= W^{(S)}_{\mu\nu}(P,q) + iW^{(A)}_{\mu\nu}(P,q,S) && (2.18) \end{aligned}$$

The hadronic tensor can according to (2.18) also be split into a symmetric, spin-independent term $W^{(S)}_{\mu\nu}$ and an anti-symmetric term $W^{(A)}_{\mu\nu}$ which depends on the nucleon spin S. Accordingly, the two structure functions $F_1(x, Q^2)$ and $F_2(x, Q^2)$ are associated with unpolarised DIS and $g_1(x, Q^2)$ and $g_2(x, Q^2)$ with polarised DIS. Since the conjugation of an anti-symmetric tensor with a symmetric tensor is zero, the combination of the general expressions for $L_{\mu\nu}$ and $W_{\mu\nu}$ in (2.14) also produces separate symmetric and anti-symmetric terms:

[2] The structure functions are introduced here in their dimensionless form. A second common notation defines four structure functions W_1, W_2, G_1, G_2, which are related to the dimensionless forms through the following formulae: $MW_1 \equiv F_1, \nu W_2 \equiv F_2, M^2\nu G_1 \equiv g_1, M\nu^2 G_2 \equiv g_2$

$$\frac{d^3\sigma}{dxdyd\varphi} = \frac{y\alpha^2}{2Q^4}\left(\underbrace{L^{(S)}_{\mu\nu}(k,k')W^{\mu\nu(S)}(P,q)}_{spin-independent} - \underbrace{L^{(A)}_{\mu\nu}(k,k',s)W^{\mu\nu(A)}(P,q,S)}_{doubly\ spin-dependent}\right) \tag{2.19}$$

The resultant double spin-dependence (on both the lepton spin s and the hadron spin S) of the anti-symmetric part of the cross-section means that this term must be investigated with polarised beam and target. The COMPASS experiment is in a position to perform such investigations.

Since it is only possible to produce a muon beam which is polarised either parallel or anti-parallel ("longitudinally") to the direction of its momentum, it is only the target polarisation which can be chosen without restriction in an experiment such as COMPASS. To take into account this fact, the spin-dependent cross-section is further decomposed into a longitudinally polarised term $d\sigma_{\parallel}$, equivalent to parallel or anti-parallel target polarisation with respect to the beam direction, and a transverse term $d\sigma_{\perp}$ in which the target polarisation is perpendicular to the beam direction. The coordinate system defines the target spin vector S in relation to the scattering plane defined by the momentum vectors of the incoming and outgoing muons ($\vec{k}$ and $\vec{k'}$) using two angles β and φ (Figure 2.2):

$$\frac{d^3\sigma}{dxdyd\varphi} = \frac{d^3\overline{\sigma}}{dxdyd\varphi} - H_l \cos\beta \frac{d^3\sigma_{\parallel}}{dxdyd\varphi} - H_l \sin\beta\cos\varphi \frac{d^3\sigma_{\perp}}{dxdyd\varphi} \tag{2.20}$$

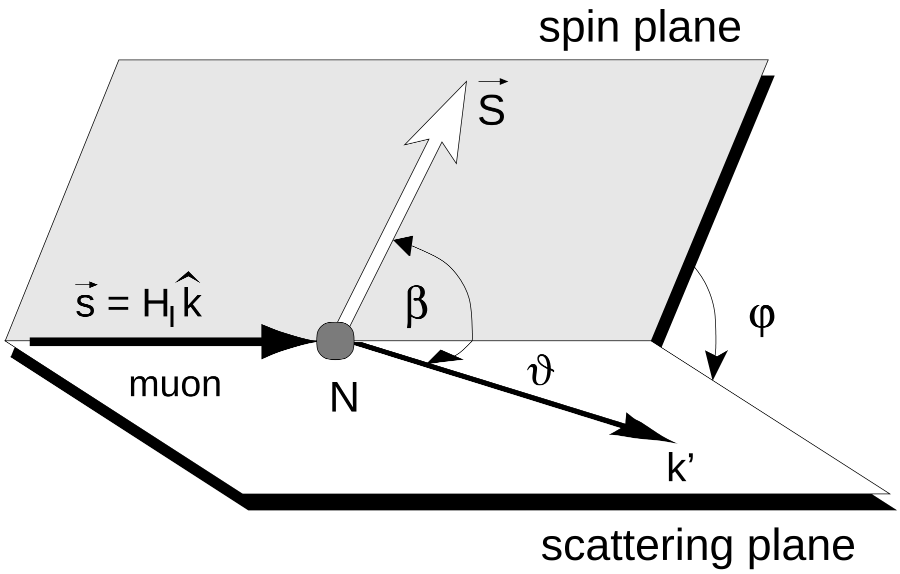

Figure 2.2: Definition of the angles θ, β and φ

$\overline{\sigma}$ is here the unpolarised cross-section and H_l the helicity of the lepton beam $H_l = \pm 1$. The COMPASS target can be polarised both longitudinally and transversely to the beam direction (see Section 3.3); both terms of the polarised cross-section are therefore accessible in separate measurements.

The individual differential cross-sections can be parameterised as follows:

$$\begin{aligned}
\frac{d^3\overline{\sigma}}{dxdyd\varphi} &= \frac{4\alpha^2}{Q^2}\left[\frac{y}{2}F_1(x,Q^2)+\frac{1}{2xy}\left(1-y-\frac{y^2\gamma^2}{4}\right)F_2(x,Q^2)\right] \\
\frac{d^3\sigma_{\parallel}}{dxdyd\varphi} &= \frac{4\alpha^2}{Q^2}\left[\left(1-y-\frac{y^2\gamma^2}{4}\right)g_1(x,Q^2)-\frac{y}{2}\gamma^2 g_2(x,Q^2)\right] \qquad (2.22) \\
\frac{d^3\sigma_{\perp}}{dxdyd\varphi} &= \frac{4\alpha^2}{Q^2}\left[\gamma\sqrt{1-y-\frac{y^2\gamma^2}{4}}\left(\frac{y}{2}g_1(x,Q^2)+g_2(x,Q^2)\right)\right] \qquad (2.23) \\
\text{with} \quad \gamma^2 &= \frac{2Mx}{Ey}. \qquad (2.24)
\end{aligned}$$

The factor γ^2 depends on the nucleon mass M and the beam energy E and can be easily determined for COMPASS conditions [4]:

$$\gamma^2 = \frac{2x}{160y} \approx \frac{1}{80} \qquad (2.25)$$

where the approximation follows from the assumption $x \approx y$. It is clear from (2.22) and (2.23) that the contribution of g_2 to the longitudinal cross-section is heavily suppressed compared to that of g_1, whereas in the transverse case both structure functions appear in the same order of magnitude. This would suggest that g_1 can be determined with a high level of accuracy through measurement with longitudinal polarised target alone; once g_1 is known, g_2 can be determined through a transverse measurement.

Equation (2.23) also suggests that the transverse cross-section is universally suppressed by a factor γ (approximately 10 under COMPASS conditions) compared to the longitudinal cross-section. Polarisation effects generally are also only observed on top of a high unpolarised background. In order to reduce systematic effects such as variable beam quality or acceptance effects in these very sensitive measurements, cross-section asymmetries are normally measured. They are defined as follows in the longitudinal and transverse cases:

$$\begin{aligned}
A_{\parallel}(x,Q^2) &= \frac{d\sigma_{\parallel}^{\leftarrow\Rightarrow}-d\sigma_{\parallel}^{\leftarrow\Leftarrow}}{d\sigma_{\parallel}^{\leftarrow\Rightarrow}+d\sigma_{\parallel}^{\leftarrow\Leftarrow}} \qquad (2.26) \\
A_{\perp}(x,Q^2) &= \frac{1}{\cos\varphi}\frac{d\sigma_{\perp}^{\leftarrow\Uparrow}-d\sigma_{\perp}^{\leftarrow\Downarrow}}{d\sigma_{\perp}^{\leftarrow\Uparrow}+d\sigma_{\perp}^{\leftarrow\Downarrow}} \qquad (2.27) \\
&= \frac{H_l}{\cos\varphi}\frac{d\sigma_{\perp}(\varphi)-d\sigma_{\perp}(\varphi+\pi)}{d\sigma_{\perp}(\varphi)+d\sigma_{\perp}(\varphi+\pi)} \qquad (2.28)
\end{aligned}$$

where $\leftarrow$ etc. represents the beam polarisation, and $\Leftarrow$ etc. the target polarisation. Hence in order to measure longitudinal asymmetries, the target polarisation (or theoretically the beam polarisation, were this not predetermined in the case of a muon beam) must be flipped. The same applies to the transverse case; here there is also according to (2.28) the possibility of comparing the *azimuthal* asymmetry in the counting rates on opposite sides of the detector. The measurement of such an asymmetry is the subject of the analysis of the Collins Effect in Chapter 5.

2.3 Photo-Absorption

The measured polarised asymmetries $A_{\parallel}(x, Q^2)$ and $A_{\perp}(x, Q^2)$ from (2.26) and (2.27) have no intuitive physical interpretation. Through the parameters y and γ^2 they also depend strongly on the beam energy E, making a direct comparison at different energies impossible. For this reason, the asymmetries are often expressed in terms of the flow of virtual photons absorbed by the nucleon, with the beam lepton playing no rôle other than that of a photon source. The hadronic tensor $W_{\mu\nu}$ can also be expressed in terms of the amplitudes

$$T_{\mu\nu} = i \int d^4\xi e^{iq\cdot\xi} \langle PS|\mathcal{T}(J_\mu(\xi)J_\nu(0))|PS\rangle \tag{2.29}$$

in the forwards Compton scattering of a virtual photon on a nucleon $\gamma^* N \rightarrow \gamma^{*\prime} N'$, using the relation

$$W_{\mu\nu} = \frac{1}{2\pi} Im T_{\mu\nu}. \tag{2.30}$$

The imaginary part of the Compton scattering amplitude is also related via the optical theorem to the virtual-photon absorption cross-sections. The following relations between these and the nucleon structure functions may be obtained [5]:

$$\sigma_L^0 = \frac{4\pi^2\alpha}{MK}\left(-F_1 + \frac{F_2}{2x}(1+\gamma^2)\right) \tag{2.31}$$

$$\sigma_T^{1/2} = \frac{4\pi^2\alpha}{MK}\left(F_1 + g_1 - \gamma^2 g_2\right) \tag{2.32}$$

$$\sigma_T^{3/2} = \frac{4\pi^2\alpha}{MK}\left(F_1 - g_1 + \gamma^2 g_2\right) \tag{2.33}$$

$$\sigma_{TL}^{1/2} = \frac{4\pi^2\alpha}{MK}\left(\gamma(g_1 + g_2)\right) \tag{2.34}$$

with the nucleon mass M and a normalisation factor $K = \nu - Q^2/2M$. Equation (2.31) applies to a longitudinally polarised photon; (2.32) and (2.33) to a transversely polarised photon. The indices $\frac{1}{2}$ and $\frac{3}{2}$ represent the relative alignment of the photon and nucleon spins in relation to one another (anti-parallel or parallel). Equation (2.34) is an interference term between transversely and longitudinally polarised photons. Two photon-nucleon asymmetries, $A_1(x, Q^2)$ and $A_2(x, Q^2)$, are also defined:

$$A_1 = \frac{\sigma_T^{1/2} - \sigma_T^{3/2}}{\sigma_T^{1/2} + \sigma_T^{3/2}} = \frac{g_1 - \gamma^2 g_2}{F_1} \approx \frac{g_1}{F_1} \tag{2.35}$$

$$A_2 = \frac{2\sigma_{TL}}{\sigma_T^{1/2} + \sigma_T^{3/2}} = \gamma \frac{g_1 + g_2}{F_1} \tag{2.36}$$

The relations between the measured asymmetries $A_{\|}$ and $A_{\perp}$ and the photon-nucleon asymmetries can be shown using (2.31) - (2.34) to be

$$A_{\|} = D(A_1 + \eta A_2) \tag{2.37}$$

$$A_{\perp} = d(A_2 - \xi A_1) \tag{2.38}$$

with the following definitions of the kinematic factors D, η and ξ:

$$D = \frac{y(2-y)(1+\frac{\gamma^2 y}{2})}{y^2(1+\gamma^2) + 2(1-y-\frac{\gamma^2 y^2}{4})(1+R)} \tag{2.39}$$

$$\eta = \gamma \frac{1-y-\frac{\gamma^2 y^2}{4}}{(1-\frac{y}{2})(1+\frac{\gamma y^2}{2})} \tag{2.40}$$

$$\xi = \gamma \frac{1-\frac{y}{2}}{1+\frac{\gamma^2 y}{2}}. \tag{2.41}$$

The *depolarisation factor* D has a specific interpretation as the proportion of the lepton spin transferred to the photon; R in (2.39) is the ratio of longitudinal to transverse photon cross-section given by:

$$R = \frac{\sigma_L}{\sigma_T} = \frac{F_2(1+\gamma^2) - 2xF_1}{2xF_1} \approx \frac{F_2 - 2xF_1}{2xF_1} \tag{2.42}$$

It can be shown from (2.39) that in the case of a longitudinally polarised photon the polarisation transfer is at its greatest at large values of the kinematic variable y (fractional energy transfer in the scattering process). In the transverse case in contrast, $D = 1$ at $y = 0$ and $D = 0$ at $y = 1$.

2.4 The Quark Parton Model

The discussion of the nucleon structure functions has up till now presumed that they depend on the two kinematic variables, x and Q^2. Measurements in the course of the last few decades of the twentieth century proved however that the structure functions so far measured - F_1, F_2 and g_1 - only exhibit only a very weak Q^2-dependence. This so-called scaling behaviour was predicted at the end of the 1960s by Bjørken for the deep-inelastic limit $Q^2, \nu \to \infty$ with a finite value of the ratio $Q^2/2M\nu$ [6]. A simple explanation of this phenomenon is given by the Quark Parton Model (QPM) discussed in the following sections.

2.4.1 Distribution Functions in the Naïve Quark Parton Model

The Quark Parton Model developed by Feynman at the beginning of the 1960s describes the nucleon as composed of smaller fundamental constituents, which Feynman called *partons* [7]. These building blocks of the nucleon swiftly became identified with *quarks*, the existence of which had been postulated independently by Gell-Mann and Zweig a few years before [8, 9]. Quarks are particles with one-third integer charge and a spin of one-half. The measured properties of all hadrons discovered so far can be described in terms of a quark model.

According to QPM, a deep-inelastic scattering event can be regarded as a superposition of elastic lepton-parton scattering processes. This picture is only valid when the momentum transfer Q^2 of the photon is sufficiently large that the individual partons can be resolved, i.e., in the deep-inelastic limit of lepton-nucleon scattering. The interaction must be of short duration so that the partons cannot interact among themselves. In a frame of reference where it is moving very fast, the nucleon can be regarded as a beam of partons each carrying a proportion ξ of the nucleon four-momentum P ($p_q = \xi P$). In order to calculate the proportion of the nucleon momentum carried by a quark from which a hadronic end-product of invariant mass W^2 is produced, one can write by conservation of momentum (neglecting transverse momentum components and parton masses)

$$(p_q + q)^2 = W^2. \tag{2.43}$$

In the case of an elastic lepton-parton collision, the identity $W^2 = (\xi M)^2$ holds. Equation (2.43) can then be written

$$\xi^2 P^2 + 2\xi Pq + q^2 = \xi^2 M^2 \tag{2.44}$$

which using the identities $q^2 = -Q^2$ and $P = M$ leads to

$$\xi = \frac{Q^2}{2pq} \equiv x. \tag{2.45}$$

Thus the Bjørken variable x can be interpreted as the fraction of the nucleon momentum carried by a single parton before a scattering event (c.f. Section 2.1.1).

In the case of a scattering process on a massless spin-$\frac{1}{2}$ particle, the hadronic tensor $W^{\mu\nu}$ can be calculated explicitly. The following expressions may be found for the four parton structure functions:

$$\begin{aligned} F_1^{parton}(x) &= \frac{1}{2}e_p^2\delta(\xi - x) \qquad F_2^{parton}(x) = e_p^2\xi\delta(\xi - x) \\ g_1^{parton}(x) &= \lambda\frac{1}{2}e_p^2\delta(\xi - x) \qquad g_2^{parton}(x) = 0 \end{aligned} \tag{2.46}$$

where e_p is the parton charge and $\lambda = \pm 1$ expresses the spin direction of the parton in relation to the nucleon spin (the helicity of the parton). The Dirac function δ requires $x = \xi$; i.e., absorption can only take place when the momentum of the photon is equal to that of the parton. It is generally assumed that no quark has spin transverse to the nucleon spin, an assumption which leads to the fourth structure function g_2 having no interpretation with the framework of the naïve QPM.

If the partons are identified with quarks, the nucleon structure functions are given by summing the parton structure functions over all helicity and charge states of the quarks found in the nucleon:

$$\mathcal{F}(x) = \sum_{i,\lambda} \int_0^1 q_i^\lambda(\xi) \mathcal{F}^{parton}(x,\xi) d\xi, \qquad \mathcal{F} \in F_1, F_2, g_1, g_2. \tag{2.47}$$

$q_i^\lambda(\xi)$ are the quark distribution functions which express how many quarks with spin parallel ($^+$) and anti-parallel ($^-$) to that of the nucleon there are in a momentum interval $\delta\xi$. The structure functions F_1 and F_2 apply to an unpolarised nucleon. The nucleon and thereby the quark are not aligned preferentially either parallel or antiparallel in relation to the lepton spin. The quark distribution functions $q_i(x)$ are given simply through the sum of quarks and antiquarks of a particular flavour i whose the spins are parallel or anti-parallel to the nucleon spin. The unpolarised structure functions are given by

$$F_1(x) = \frac{1}{2} \sum_i e_i^2 \left(q_i^+(x) + q_i^-(x) \right) = \frac{1}{2} \sum_i e_i^2 q_i(x) \tag{2.48}$$

$$F_2(x) = x \sum_i e_i^2 \left(q_i^+(x) + q_i^-(x) \right) = x \sum_i e_i^2 q_i(x). \tag{2.49}$$

For scattering on a polarised nucleon, two cases are differentiated. In the first case the nucleon spin, and therefore that of its quarks as well, is longitudinal to the spin of the incoming lepton. The decisive factor for the quark distribution function is the difference in the number of quarks with spin parallel to the nucleon spin compared to the number with anti-parallel spin. The quark spin is then by definition in relation to the lepton spin also parallel or anti-parallel. This distribution function yields the structure function g_1. The fundamental assumption that the spin and momentum vectors of nucleon and quarks are never transverse to one another remains, hence g_2 is not defined:

$$g_1(x) = \frac{1}{2} \sum_i e_i^2 \left(q_i^+(x) - q_i^-(x) \right) = \frac{1}{2} \sum_i e_i^2 \Delta q_i(x) \tag{2.50}$$

$$g_2(x) = 0 \tag{2.51}$$

The second possible case is that nucleon and quarks are transversely polarised with respect to the lepton spin. This is indicated in the quark distribution functions by the indices $\uparrow$ (parallel with respect to the nucleon spin) or $\downarrow$ (anti-parallel). In analogy to (2.50), a structure function h_1 may be defined:

$$h_1(x) = \frac{1}{2}\sum_i e_i^2 \left(q_i^{\uparrow}(x) - q_i^{\downarrow}(x)\right) = \frac{1}{2}\sum_i e_i^2 \Delta_T q_i(x) \tag{2.52}$$

$\Delta_T q_i(x)$ are the transversely polarised quark or *transversity* distributions. Since the structure functions in QPM are solely determined by the quark distribution functions, they depend also only on the Bjørken scaling variable x. It is therefore expected in this model that the structure functions exhibit a scaling characteristic (no Q^2-dependence). The expression associating the two unpolarised structure functions in (2.48) and (2.49):

$$2xF_1(x) = F_2(x) \tag{2.53}$$

is called the *Callan-Gross relation* and is a consequence of the assumption that quarks are particles with half-integer spin. By comparison with (2.42) it is clear that this relation applies when the cross-section σ_L for longitudinally polarised photons is zero. Conservation of angular momentum demands that transversely polarised photons only couple with particles with half-integer spin (fermions); therefore in QPM $R = 0$ (c.f. (2.42)). Substituting (2.48) and (2.50) in (2.35), which neglecting transverse components now fully describes the photon-nucleon asymmetry, one obtains

$$A_1^{\gamma N \to X}(x) = \frac{g_1(x)}{F_1(x)} = \frac{\sum_i e_i^2 \Delta q_i(x)}{\sum_i e_i^2 q_i(x)}. \tag{2.54}$$

In order to parameterise the lepton-nucleon asymmetry, the depolarisation factor D of the photons must also be taken into account:

$$A_{\parallel}^{lN \to l'X}(x) = D\frac{g_1(x)}{F_1(x)} = D\frac{\sum_i e_i^2 \Delta q_i(x)}{\sum_i e_i^2 q_i(x)}. \tag{2.55}$$

The physical background to this correlation can easily be understood with the following picture. The photon radiated by the lepton has whole-integer spin and can therefore – as a result of helicity conservation – only be absorbed by a quark with opposing spin. Recalling the definitions in Section 2.3, the cross-section $\sigma_{1/2}$ corresponds to the anti-parallel configuration of photon and nucleon spin, $\sigma_{3/2}$ to the parallel configuration. Spin conservation demands therefore that in the first case the spin of the absorbing quark is parallel to the nucleon spin, in the second case anti-parallel: i.e., $\sigma_{1/2} \sim q_i^+(x)$, $\sigma_{3/2} \sim q_i^-(x)$. Figure 2.3 illustrates the two cases.

In the case that the quark and nucleon spins are transverse to the lepton spin, the expression for the lepton-nucleon asymmetry is amended with the corresponding structure and quark distribution functions:

$$A_{\perp}^{lN \to l'X}(x) = D\frac{h_1(x)}{F_1(x)} = D\frac{\sum_i e_i^2 \Delta_T q_i(x)}{\sum_i e_i^2 q_i(x)}. \tag{2.56}$$

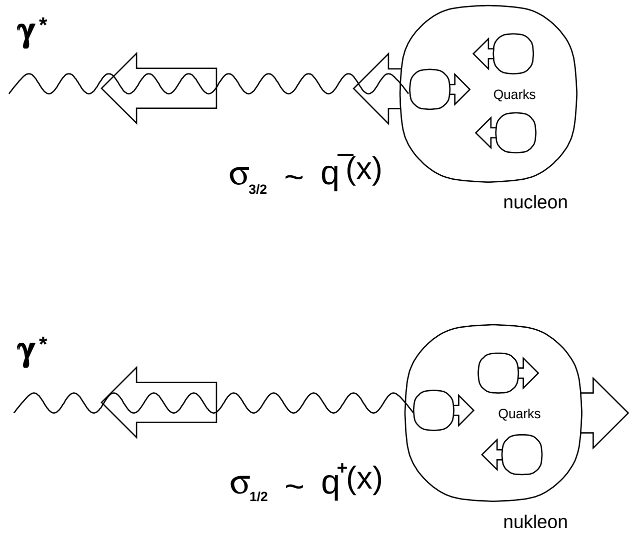

Figure 2.3: Schematic depiction of the absorption of a polarised photon by a quark in the nucleon. Spin conservation demands that photon and the quark have opposite spins: **(above)** photon and nucleon spins are parallel ($\sigma_{3/2}$), quark- and nucleon spins must therefore be anti-parallel ($q_i^-(x)$); **(below)** photon and nucleon spins are anti-parallel ($\sigma_{1/2}$), quark- and nucleon spins must therefore be parallel ($q_i^+(x)$).

2.4.2 Extension to Semi-inclusive Processes: Fragmentation Functions

The Quark Parton Model can be extended to semi-inclusive processes. This demands a closer consideration of the process by which hadrons are produced from the quark struck by the virtual photon. This process is called *fragmentation.* The starting point is the same as that in the previous section, where the nucleon was considered as a unit; in this case however it is the quark that is envisaged as a source of a beam of hadrons, the transverse momentum components of which are negligible. As in the previous case, a quantity η is introduced which represents the fraction of the quark momentum carried by a hadron produced in the fragmentation:

$$P_h = \eta p_q = \eta(xP + q). \tag{2.57}$$

A set of *fragmentation functions* $D_{h/q}(\eta)$ is also defined. $D_{h/q}(\eta)d\eta$ describes the number of hadrons of type h and with momentum in the interval $d\eta$ that is produced in the fragmentation of a quark of type q. By multiplying (2.57) by P, the initial nucleon momentum, the quantity η can be identified with the scaling variable z introduced in Section 2.1.2:

$$\begin{aligned} P \cdot P_h &= \eta P(xP + q) = \eta(xP^2 + P \cdot q) \approx \eta P \cdot q && (2.58) \\ \Rightarrow \eta &= \frac{P \cdot P_h}{P \cdot q} \equiv z \qquad (c.f.(2.12)). && (2.59) \end{aligned}$$

The approximation in (2.58) requires that the nucleon mass ($M = P$ in the laboratory frame) is negligible to the second power. The scaling variable z is now interpreted as the fraction of the fragmenting quark's momentum that is carried by a particular hadron. The parallel between $D_{h/q}(z)$ and the quark distribution functions $q_i(x)$ from the previous section is clear: the latter expresses the number of quarks of type i with a fraction x of the photon momentum in a nucleon, whilst the former represents the number of hadrons of type h and momentum fraction z that are produced in the fragmentation of a quark of type q. Thus the generation of the hadronic end-products in DIS is regarded as a result of two independent processes: the absorption of a photon by a quark, and the fragmentation of the latter to hadrons.

The fragmentation functions depend critically on the type of quark struck as compared to the constituent quarks of the hadron produced. Generally, *favoured* fragmentation functions, where the initial quark is also part of the hadronic product, are distinguished from *unfavoured* fragmentation functions, where the initial quark is not present in the final hadron state. For fragmentation to π^+- (quark content $u\bar{d}$) or π^--mesons ($\bar{u}d$) for example, there are two sets of fragmentation functions:

$$
\begin{aligned}
D_{\pi^+/u} &= D_{\pi^+/\bar{d}} = D_{\pi^-/\bar{u}} = D_{\pi^-/d} \qquad favoured & (2.60)\\
D_{\pi^+/\bar{u}} &= D_{\pi^+/d} = D\pi^-/u = D_{\pi^-/\bar{d}} \qquad unfavoured. & (2.61)
\end{aligned}
$$

Two types of fragmentation are distinguished. If the struck quark fragments to the hadron under consideration, the term *current fragmentation* is used. If the rest of the nucleon fragments, it is called *target fragmentation*. As was the case with the quark distribution functions, the unpolarised, longitudinally polarised and transversely polarised cases are dealt with separately. Writing as $\mathcal{N}_{h/q}(z)$ the probability that a hadron h with a momentum component z is found in a fragmenting quark q, and using the standard notations $\pm$ (longitudinally polarised quark) and $\uparrow\downarrow$ (transversely polarised quark), the fragmentation functions for the three cases are defined as follows:

$$
\begin{aligned}
D_{h/q}(z) &= \mathcal{N}_{h/q}(z) \qquad \textit{unpolarised} & (2.62)\\
\Delta D_{h/q}(z) &= \mathcal{N}^h_{q+}(z) - \mathcal{N}^h_{q-}(z) \qquad \textit{longitudinal} & (2.63)\\
\Delta_T D_{h/q}(z) &= \mathcal{N}^h_{q\uparrow}(z) - \mathcal{N}^h_{q\downarrow}(z) \qquad \textit{transverse} & (2.64)
\end{aligned}
$$

Augmenting the nucleon structure functions (2.48) to (2.52) from Section 2.4.1 by the appropriate fragmentation function, one obtains the hadronic structure functions for semi-inclusive production:

$$F^h_1(x,z) = \frac{1}{2}\sum_q e^2_q q_q(x) D_{h/q}(z) \qquad (2.65)$$

$$F^h_2(x,z) = x\sum_q e^2_q q_q(x) D_{h/q}(z) \qquad (2.66)$$

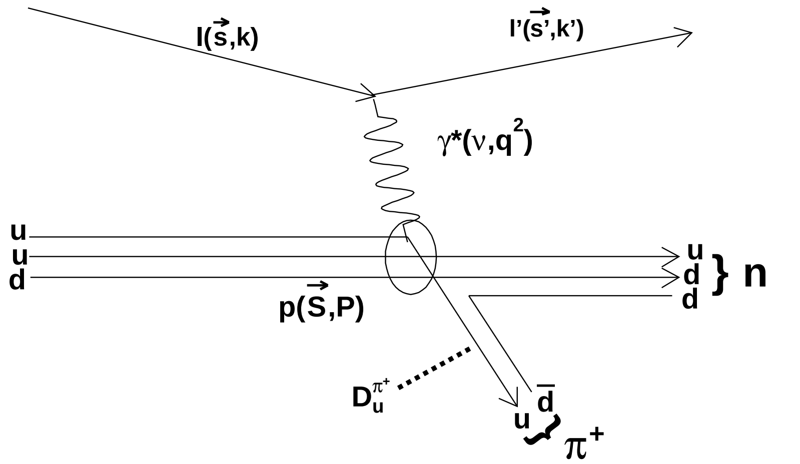

Figure 2.4: Schematic representation of a semi-inclusive DIS process. In this case the virtual proton couples to a u-quark in a proton. A $d\bar{d}$ quark-antiquark pair is produced, and the nucleon fragments into a positive pion and a neutron, which can fragment further. The probability for the fragmentation of a u-quark to a pion is given in this case by the favoured fragmentation function $D_u^{\pi^+}$.

$$g_1^h(x,z) = \frac{1}{2}\sum_q e_q^2 \Delta q_q(x)\Delta D_{h/q}(z) \tag{2.67}$$

$$h_1^h(x,z) = \frac{1}{2}\sum_q e_q^2 \Delta_T q_q(x)\Delta_T D_{h/q}(z) \tag{2.68}$$

Accordingly the expressions for the longitudinal and transverse asymmetries from (2.55) and (2.56) are in the semi-inclusive case

$$A_{\parallel}^{lN\to l'hX}(x,z) = D\frac{g_1^h(x,z)}{F_1^h(x,z)} = D\frac{\sum_i e_i^2 \Delta q_i(x)\Delta D_{h/q}(z)}{\sum_i e_i^2 q_i(x) D_{h/q}(z)} \tag{2.69}$$

$$A_{\perp}^{lN\to l'hX}(x,z) = D\frac{h_1^h(x,z)}{F_1^h(x,z)} = D\frac{\sum_i e_i^2 \Delta_T q_i(x)\Delta_T D_{h/q}(z)}{\sum_i e_i^2 q_i(x) D_{h/q}(z)}. \tag{2.70}$$

2.4.3 Sum Rules in the Quark Parton Model

The theoretical description of the spin structure functions g_1 and h_1 is as yet incomplete. Several models use so-called sum rules to attempt to describe the structure of the nucleon (neutron n or proton p). Generally the first moment Γ_1 of the structure function integrated over the whole range of x is taken

$$\Gamma_1 = \int_0^1 g_1(x)dx \tag{2.71}$$

The polarised quark distribution functions are also integrated over x:

$$\Delta q_i = \int_0^1 \Delta q_i(x)dx \tag{2.72}$$

Conventionally, the distribution functions are defined with reference to the quark distributions in the proton; considering isospin symmetry, the following relations for $\Delta q_{i;p,n} = q^{\uparrow}_{i;p,n} - q^{\downarrow}_{i;p,n}$ can be established:

$$\begin{aligned} \Delta u_p = \Delta d_n &:= \Delta u && (2.73)\\ \Delta d_p = \Delta u_n &:= \Delta d && (2.74) \end{aligned}$$

For the proton (valence quarks uud) and neutron (udd) this leads to the following expressions, starting from the definition of $g_1(x)$ in (2.50):

$$\begin{aligned} \Gamma_1^p \equiv \int_0^1 g_1^p(x)dx &= \frac{1}{2}\left(\frac{4}{9}\Delta u + \frac{1}{9}\Delta d + \frac{1}{9}\Delta s\right) && (2.75)\\ \Gamma_1^n \equiv \int_0^1 g_1^n(x)dx &= \frac{1}{2}\left(\frac{1}{9}\Delta u + \frac{4}{9}\Delta d + \frac{1}{9}\Delta s\right) && (2.76) \end{aligned}$$

Δs encompasses the contribution of strange sea quarks in each nucleon. It is assumed that apart from u- and d- quarks only the lighter s-quarks appear in the sea. Equations (2.75) and (2.76) can also be expressed in terms of the proton matrix elements of the axial vector current a_k as

$$\Gamma_1^{p,n} = \pm\frac{1}{12}\underbrace{(\Delta u - \Delta d)}_{a_3} + \frac{1}{36}\underbrace{(\Delta u + \Delta d - 2\Delta s)}_{\sqrt{3}a_8} + \frac{1}{9}\underbrace{(\Delta u + \Delta d + \Delta s)}_{a_0}, \tag{2.77}$$

where the positive sign in the first term applies to the proton, the negative sign to the neutron. The identities for a_0, a_3 and a_8 are only valid with the assumption of non-interacting point partons – i.e., only in QPM. a_3 and a_8 are connected to the weak decay constants F and D through

$$a_3 = F + D = \left|\frac{g_A}{g_V}\right|, \qquad \sqrt{3}a_8 = 3F - D \tag{2.78}$$

where $|g_A/g_v|$ is the ratio of axial vector to vector coupling constant in the Cabibbo theory of the weak interaction [10]. Measurements from hyperon decay produce the values

$$F = 0.477 \pm 0.012, \qquad D = 0.756 \pm 0.011. \tag{2.79}$$

It is also known from measurements of neutrino decay that

$$\left|\frac{g_A}{g_V}\right| = 1.2573 \pm 0.00028, \tag{2.80}$$

meaning that a_3 and a_8 are known to a good accuracy. The matrix element a_0, where

$$a_0 = \Delta u + \Delta d + \Delta s := \Delta\Sigma \tag{2.81}$$

is equivalent to the total quark helicity contribution $\Delta\Sigma$ (also known as the *axial charge*) in QPM. It is however not associated with any reaction and thus in the first instance unknown. The first sum rule, devised by Bjørken, predicts the difference between the proton and neutron first moments [6], and can be read off directly from (2.77):

$$\Gamma_1^p - \Gamma_1^n = \frac{1}{6}a_3 = \frac{1}{6}\left|\frac{g_A}{g_V}\right| \tag{2.82}$$

The lack of suitable neutron targets meant that $\Gamma_1^p - \Gamma_1^n$ was for a long time experimentally inaccessible. Ellis and Jaffe postulated therefore their sum rule, in which they neglect the contribution of strange quarks ($\Delta S = 0$) and write $a_0 = \sqrt{3}a_8$ and therefore [11]

$$\Gamma_1^{p,n} = \frac{1}{12}\left|\frac{g_A}{g_V}\right|\left(\pm 1 + \frac{5}{3}\frac{3F/D - 1}{F/D + 1}\right). \tag{2.83}$$

Whilst first experimental results seemed to confirm the Ellis-Jaffe sum rule, the extension of the accessible kinematic range to lower values of x at the EMC experiment at the end of the 1980s revealed a significant discrepancy, with the measured value for the total helicity contribution, $\Delta\Sigma = 0.12 \pm 0.17$, lying well beneath the 0.579 ± 0.026 predicted by the sum rule [12, 13]. More recent results increase the best experimental value to 0.23 ± 0.07 [14], but it remains to be explained where the missing contribution comes from. It is clear, however, that the naive QPM is not sufficient to achieve a complete picture of the structure of the nucleon.

2.4.4 The QCD-extended Parton Model

An more-or-less complete description of the nucleon according to current knowledge is given by the field theory of quantum chromodynamics (QCD). QCD introduces gluons as vector bosons conveying the strong nuclear interaction. In the QCD-extended Parton Model, quarks can radiate gluons, which can themselves either be re-absorbed by the quarks, produce quark-antiquark pairs or radiate further gluons. These further partons constitute a “cloud” around the initial quark.

In this model, the quark is no longer a well-defined object and loses the point-like nature which it gained in the naïve QPM. How a quark is “seen” by the outside world depends on the resolving power of the electromagnetic probe used to investigate it – i.e., whether it can resolve the partons surrounding the struck quark or not (Figure 2.5). The resolution that can be achieved in a DIS experiment is essentially given by the momentum transfer through the virtual photon as represented by the variable Q^2. The dependence is of the form $1/\sqrt{Q^2}$; thus the greater the momentum exchange, the larger the number of partons which can be resolved. The average momentum fraction x of each resolved parton

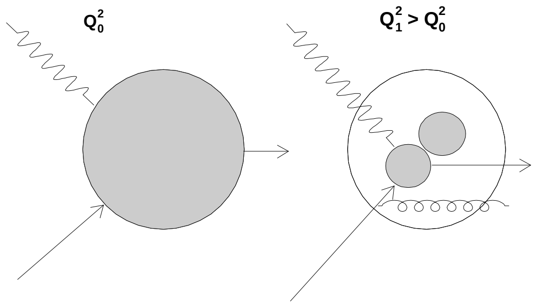

Figure 2.5: Illustration of the background to scaling violation. If the virtual photon transfers only a small momentum Q_0^2, it resolves only larger structures (left). At higher momentum transfer, the photon has a greater resolving power: smaller structures also become visible. The average momentum fraction of the resolved objects falls accordingly, a phenomenon known as scaling violation.

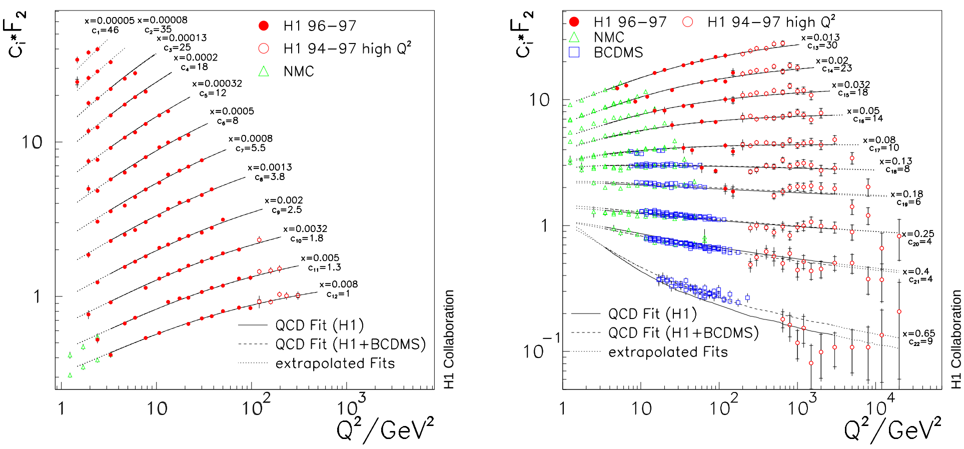

Figure 2.6: Scaling violation of the structure function f_2 (data from the H1 collaboration [15]). For small x, the value of the structure function increases with growing Q^2; from $x \sim 0.25$ upwards the value sinks with growing Q^2.

would then fall. This explains the phenomenon known as *scaling violation* - the fact that the nucleon structure functions in addition to their x-dependence also in general depend on Q^2 (Figure 2.6). Various experiments had shown that the scaling behaviour predicted by Bjørken on the basis of QPM did not hold strictly for the entire kinematic range. For small values of x, the structure functions grow with Q^2; for larger values of x, they sink with growing Q^2. This behaviour is exactly that expected from the QCD-extended Parton Model.

A general expression for the nucleon spin S that takes in account possible contributions from gluon spin ΔG and the orbital angular momentum of the quarks and gluons (L_q and L_g), as well as the helicity contribution $\Delta\Sigma$ already discussed, may be written

$$S = \frac{1}{2} = \frac{1}{2}\Delta\Sigma + \Delta G + L_q + L_g. \tag{2.84}$$

First measurements aimed at quantifying the contribution of gluon polarisation ΔG to the total spin of the nucleon have been performed by the HERMES collaboration at DESY in Hamburg, and point to a positive, but small value [16]. A precision measurement of the gluon polarisation is one of the main tasks of the COMPASS experiment, and is discussed in the next section.

2.5 Determining the Gluon Polarisation

Previous measurements of the gluon polarisation ΔG have focussed on its indirect measurement through the analysis of the scaling behaviour of the longitudinally polarised structure function g_1. This effect has proved however to be relatively small in the kinematic range measured so far; this, coupled with an insufficient number of measurements, mean that the range of possible values for ΔG has been only minimally constrained. One aim of the COMPASS experiment is to measure gluon polarisation through the process of photon-gluon fusion (PGF), in which the virtual photon in a DIS event couples with a gluon radiated from the nucleon (Figure 2.7). The identification of the most energetic or *leading* hadron in a semi-inclusive scattering process allows inferences to be drawn via the fragmentation functions as to what quarks were involved in the primary process (c.f. Section 2.4.2). Two methods are available to COMPASS allowing the selection of PGF events though suppression of background – so-called *open charm production* on the one hand and the production of hadron pairs with high transverse momentum on the other.

2.5.1 Open Charm Production

Since there is no charm-quark component in the nucleon in leading order, a charm quark can only have been produced "outside" the nucleon through the production of a charm-anticharm quark pair in PGF. This channel is therefore particularly free of background. The centre-of-mass energy for the production

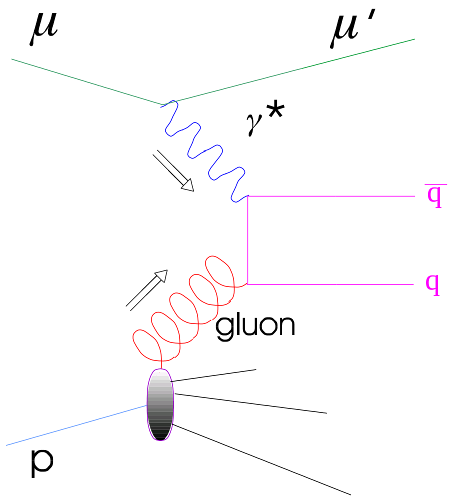

Figure 2.7: Generalised portrayal of a photon-gluon fusion process. A virtual photon γ^* couples via a quark-antiquark pair $q\bar{q}$ to a gluon.

of a charm-anticharm quark pair is $4m_c^2$, or approximately 9 GeV. The cross-section for photoproduction is given by

$$A_{\gamma N}^{c\bar{c}}(E, y) = \frac{\Delta\sigma^{\gamma N \to c\bar{c}X}}{\sigma^{\gamma N \to c\bar{c}X}} = \frac{\int_{4m_c^2}^{2M\nu} \Delta\sigma(\hat{s})\Delta G(x_G, \hat{s})}{\int_{4m_c^2}^{2M\nu} \sigma(\hat{s})G(x_G, \hat{s})} \tag{2.85}$$

where $\Delta\sigma(\hat{s})$ and $\sigma(\hat{s})$ are the polarised and unpolarised photon-gluon cross-sections, and ΔG and G the polarised and unpolarised gluon distributions. The differential total cross-section in muoproduction is given by

$$\frac{d^2\sigma^{\mu N \to c\bar{c}X}}{dQ^2 d\nu} = \Gamma(E, Q^2, \nu) \frac{\sigma^{\gamma N \to c\bar{c}X}(\nu)}{\left(1 + \frac{Q^2}{M_0^2}\right)^2} \tag{2.86}$$

with the kinematic variables as defined in Section 2.1 and M_0 as a empirically determined parameter [17]. The pre-factor Γ describes the photon flux as a function of the beam energy as

$$\Gamma(E, Q^2, \nu) = \frac{\alpha_e}{2\pi} \frac{2(1-y) + y^2 + Q^2/2E^2}{Q^2(Q^2 + \nu^2)^{1/2}} \tag{2.87}$$

For finite energy transfer ν, Γ rises steeply at low Q^2. In order to gather enough events it is therefore imperative to measure the entire photon spectrum down to the quasi-real region at $Q^2 \approx 0$ [18]. Since this region corresponds to events where the muon was scattered at very small angles, fast detectors with high-rate capability are required for the detection of the scattered particle for a precision measurement of the gluon polarisation. To this end, hodoscopes using scintillating fibres were developed for COMPASS. Details of their construction and their properties are given in Chapter 4 of this thesis.

COMPASS expects a yield of around 1.2 D^0 and $\bar{D}^0$ events per charm event [17]. In the simplest decay channel, $D^0 \rightarrow K^-\pi^+$, the participating kaons and pions fly at large angles away from each other in the centre-of-mass system, enabling them to be easily distinguished from mesons produced in target fragmentation using kinematic cuts.

2.5.2 Hadron Pairs with Large Transverse Momentum

The second method employed by COMPASS to determine the gluon polarisation requires the semi-inclusive detection of two hadrons of opposite charge in PGF events of the archetype $\gamma g \rightarrow q\bar{q} \rightarrow h^+h^-X$. These hadrons fly almost in opposite directions from each other with a large transverse momentum component with respect to the momentum of the virtual photon. The reaction signature is therefore unambiguous, allowing the suppression of background. A significant background contribution of around 30% remains however from QCD Compton scattering, $\gamma^\star q \rightarrow qg$, which must be taken into account in Monte Carlo simulations [19]. The asymmetry in muoproduction is given by

$$A^{\mu N \rightarrow hh} \approx \langle \hat{a}^{\gamma g \rightarrow q\bar{q}} \rangle \frac{\Delta g}{g} \frac{V}{1+V} + \langle \hat{a}^{\gamma q \rightarrow qg} \rangle A_1 \frac{1}{1+V} \tag{2.88}$$

where $\hat{a}^{\gamma g \rightarrow q\bar{q}}$ and $\hat{a}^{\gamma q \rightarrow qg}$ are the PGF and QCD Compton asymmetries respectively, and V the ratio of the two reaction probabilities.

In the hadron-pair channel the effect is also expected to be maximal at small Q^2, meaning that here too detectors for the measurement of minimally deflected muons are indispensable.

2.6 Transverse Spin Effects

The experimental knowledge of polarised DIS has up till now related almost without exception to the case where the target nucleon spin is longitudinal (parallel or anti-parallel) with respect to the direction of motion of the beam. The investigation of transverse spin effects was for a long time both theoretically and experimentally disregarded, since they are suppressed by a kinematic factor γ (c.f. (2.22) and (2.23)) and can therefore be neglected in leading order. Only in the course of the last decade has the significance of transverse effects been reassessed, with the result that their categorical neglect is now regarded as impermissible. In particular the transverse quark polarisation or *quark transversity* is neither kinematically or dynamically suppressed and represents in some hadronic processes the largest contribution. It is also expected that the structure function $h_1(x)$ connected to these spin distributions will exhibit a quite different behaviour as the equivalent longitudinal and unpolarised functions, since no gluon contribution is expected [20]. No scaling behaviour (see Section 2.4.4) is therefore expected with h_1.

A new series of experiments, of which COMPASS is one, has as its goal a better and deeper understanding of this area of spin physics. A contribution was made as part of the work described in this thesis to the analysis of a possible transverse spin asymmetry in single pion production, the so-called *Collins effect*, which would allow access to the transverse quark distributions. In this section the theoretical background to transversity is discussed.

2.6.1 Notation and Terminology

Distribution Functions

Three quark distribution functions (DFs) for each quark flavour were introduced in Section 2.4.1. In this context, $q(x)$ describes the unpolarised quark distribution and Δq the longitudinal or *helicity* distribution. $\Delta_T q(x)$ is the transversely polarised distribution function or *transversity* distribution:

$$q(x) = q_+(x) + q_-(x) \tag{2.89}$$
$$\Delta q(x) = q_+(x) - q_-(x) \quad \textit{helicity distribution} \tag{2.90}$$
$$\Delta_T q(x) = q_\uparrow(x) - q_\downarrow(x) \quad \textit{transversity distribution} \tag{2.91}$$

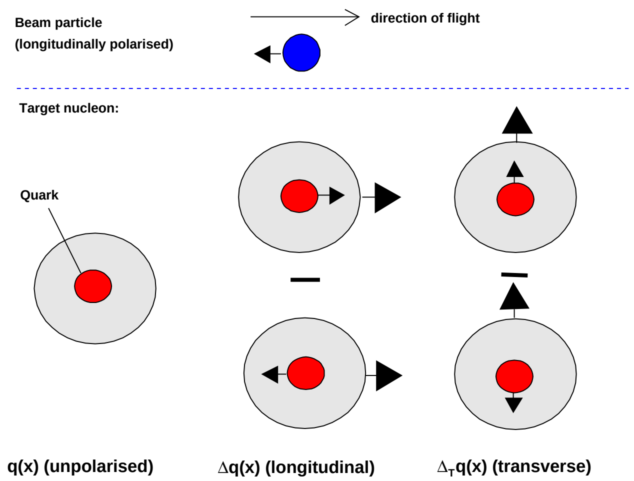

Figure 2.8: Schematic representation of the quark distribution functions $q(x)$, $\Delta q(x)$ and $\Delta_T q(x)$. The beam particle (top) moves from right to left and is longitudinally polarised. **(a)** The distribution function $q(x)$ corresponds to the case of an unpolarised target nucleon. **(b)** The nucleon is longitudinally polarised with respect to the direction of motion of the beam particle. The function $\Delta q(x)$ is the numerical difference in the number of quarks in this nucleon the spins of which are parallel and anti-parallel with respect to that of the nucleon. **(c)** The nucleon is transversely polarised with respect to the beam particle; the function $\Delta_T q(x)$, is defined exactly as $\Delta_T q(x)$ with the difference that the quark spin is transverse with regard to the direction of motion of the beam particle. The general assumption is made that quarks with transverse spin with respect to their parent nucleon do not exist.

Neglecting quark momentum components which are transverse to the momentum of the nucleon, these three DFs suffice for a complete description of the internal dynamics of the nucleon. This restriction was introduced as a consequence of the naive Quark Parton Model (Section 2.4.1) and results in the

Distribution Functions (DFs)			
Quark Spin	Nucleon Spin	$k_\perp$-integrated	$k_\perp$-dependent
0	T	$\Delta_0^T q$	$f_{1T}^\perp$
L	T	$\Delta_L^T q$	g_{1T}
T	0	$\Delta_T^0 q$	$h_1^\perp$
T	L	$\Delta_T^L q$	$h_{1L}^\perp$
T	T	$\Delta_T^T q$	$h_{1T}^\perp$

Table 2.1: Summary of DF notations

missing definition of the second polarised DIS structure function g_2. Permitting a finite transverse quark momentum $\vec{k}_\perp$ leads to a multiplication of the number of DFs according to the spin alignment of the nucleon and its constituent quarks. Following the convention in [21], two notations are introduced as summarised in Table 2.1, one for DFs integrated over $\vec{k}_\perp$ and one for $\vec{k}_\perp$-dependent functions:

- The first notation, for $\vec{k}_\perp$-integrated DFs, extends the already familiar notation with a superscript according to the polarisation of the nucleon and a subscript for that of the quarks. Both can be either 0 (unpolarised), L (longitudinally polarised) or T (transversely polarised).

- The second notation originates in [22, 23] and pertains to the $\vec{k}_\perp$-dependent DFs. Using the same convention as the DIS structure functions, it takes the letters f, g and h to signify the polarisation of the quarks (unpolarised, longitudinal, transverse). For a longitudinally (transversely) polarised nucleon a subscript L (T) is added. The notation also makes reference to the *twist* of the function. This is the parameter t in the kinematic factor Q^{-t+2} and is connected to the lowest order to which an effect is present in the DIS cross-section; *twist-two* is also known as *leading twist* and corresponds to an effect that appears in leading order. For historical reasons twist-two is signified by a subscript 1. Finally, a superscript $\perp$ indicates that transverse momentum components are present in the distribution.

Fragmentation Functions

A similar notation is used for the fragmentation functions (FFs). The three basis FFs (neglecting transverse quark momentum) are defined as in (2.62) - (2.64). $k_\perp$-integrated and $k_\perp$-dependent FFs are also introduced, with the difference that the index which indicated the polarisation of the initial nucleon applies here to the polarisation of the hadron h produced in the fragmentation of a quark q. Instead of the scheme f, g and h, the letters D, G and H are used for the unpolarised, longitudinal and transverse functions respectively. Table 2.2 summarises these notations.

Fragmentation Functions (FFs)			
Quark Spin	Nucleon Spin	$\vec{k}_\perp$-integrated	$k_\perp$-dependent
0	T	$\Delta_0^T D$	$D_{1T}^\perp$
L	T	$\Delta_L^T D$	G_{1T}
T	0	$\Delta_T^0 D$	$H_1^\perp$
T	L	$\Delta_T^L D$	$H_{1L}^\perp$
T	T	$\Delta_T^T D$	$H_{1T}^\perp$

Table 2.2: Summary of FF notations

2.6.2 The Transversity Distribution $\Delta_T q(x)$

As mentioned in the previous section, the transversity distribution $\Delta_T q(x)$ supplies together with the unpolarised DF $q(x)$ and the helicity distribution $\Delta q(x)$ a complete picture of the nucleon in leading order. The hadronic tensor, which describes the dynamics of the nucleon in DIS, is associated with the imaginary part of the virtual forwards Compton scattering amplitude (c.f. (2.29), (2.30)). In this context the various quark distribution functions can also be understood in terms of scattering amplitudes in a process in which a nucleon radiates and re-absorbs a quark, which then itself interacts with an incoming virtual photon. These scattering amplitudes are generally expressed in the quark-nucleon helicity basis in the form $\mathcal{A}_{hH,h'H'}$, where h and H represent quark and nucleon helicities before emission and h' and H' the helicities after the re-absorption. Of the 16 mathematically possible combinations remain, following the requirement that the total helicity be conserved,

$$h + H = h' + H', \tag{2.92}$$

only six variations, i.e.

$$\mathcal{A}_{++,++}, \mathcal{A}_{--,--}, \mathcal{A}_{+-,+-}, \mathcal{A}_{-+,-+}, \mathcal{A}_{+-,-+}, \mathcal{A}_{-+,+-}. \tag{2.93}$$

Invariance under time-reversal swaps initial and final states $\mathcal{A}_{hH,h'H'} = \mathcal{A}_{h'H',hH}$ and therefore does not limit the number of amplitudes further. Parity invariance demands however that $\mathcal{A}_{hH,h'H'} = \mathcal{A}_{-h-H,-h'-H'}$ and reduces the number of permissible amplitudes further to three:

$$\begin{aligned} \mathcal{A}_{++,++} &= \mathcal{A}_{--,--} \\ \mathcal{A}_{+-,+-} &= \mathcal{A}_{-+,-+} \\ \mathcal{A}_{+-,-+} &= \mathcal{A}_{-+,+-} \end{aligned} \tag{2.94}$$

The first two amplitudes contain no helicity-flip and can be associated via the optical theorem with the unpolarised and longitudinal quark distribution functions:

$$q(x) \sim Im(\mathcal{A}_{++,++} + \mathcal{A}_{+-,+-}) \tag{2.95}$$
$$\Delta q(x) \sim Im(\mathcal{A}_{++,++} - \mathcal{A}_{+-,+-}). \tag{2.96}$$

The third amplitude $\mathcal{A}_{+-,-+}$ contains a helicity-flip of nucleon and quark and corresponds to the transverse case:

$$\Delta_T q(x) \sim Im\mathcal{A}_{+-,-+} \tag{2.97}$$

$\Delta_T q(x)$ is said to possess odd *chirality*[3]. This has far-reaching consequences for the experimental investigation of transverse spin effects. It means that inclusive DIS can supply no information on $\Delta_T q(x)$ (in contrast to the unpolarised and longitudinal DFs), since no mechanism exists to produce the helicity flip of the quark. A second chiral-odd function, such as a second distribution function from another hadron or a fragmentation function, has to take part in the reaction, so that the process as a whole is chiral-even. Figure 2.9 illustrates this principle.

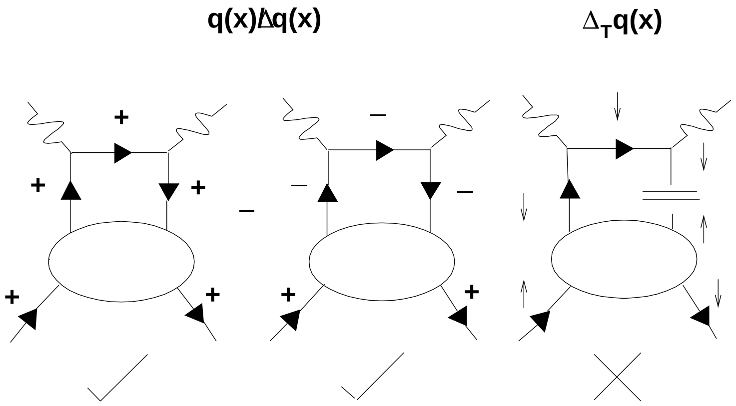

Figure 2.9: "Handbag" diagram for quark-nucleon scattering. In the unpolarised and longitudinally polarised cases (left/centre) nucleon (incoming/outgoing line at the bottom of each diagram) and quark (lines above) retain their initial helicity state. These cases may be investigated in normal inclusive DIS. In the transverse case (right) however both quark and nucleon spins flip. A second process with attendant function is required to achieve this. The transverse case decouples from inclusive DIS.

Consideration of the relative magnitudes of the scattering amplitudes $\mathcal{A}_{hH,h'H'}$ in quark-nucleon scattering allows important relations to be established between the three leading-order DFs for a quark flavour i. As well as the requirements

$$q_i(x) \geq 0 \tag{2.98}$$
$$q_i(x) \geq |\Delta q_i(x)|, \tag{2.99}$$

[3]Generally chirality is used to express the "handedness" of a particle in the spinor solutions to the Dirac equation [24]. In the relativistic limit $m/E \to 0$, chirality is equivalent to helicity; mass corrections for quarks are twist-three effects ($\mathcal{O}(m/\sqrt{Q^2})$ [25] and therefore not significant in leading order in DIS. In this context however chirality is used solely as a property of a DF or FF, with odd chirality representing a helicity-flip channel.

the so-called *Soffer bound* emerges for the transversity distribution [26], namely

$$q_i(x) + \Delta q_i(x) \geq 2 \mid \Delta_T q_i(x) \mid . \tag{2.100}$$

It is expected that the helicity and transversity distributions will be approximately equal in their order of magnitude. For non-relativistic quarks they should be equal:

$$\Delta q_i(x) = \Delta_T q_i(x) \qquad (non-relativistic) \tag{2.101}$$

It is clear therefore that a measured difference between transversity and helicity distributions should allow access to the relativistic properties of quarks. First lattice-QCD calculations point to significantly larger values for the transversity distributions as for their helicity counterparts. Defining a new quantity, the *tensor charge* $\Delta_T\Sigma$, a value

$$\begin{aligned} \Delta_T\Sigma &= \Delta_T u(x) + \Delta_T d(x) + \Delta_T s(x) \\ &= 0.84 + (-0.23) + (-0.05) \\ &= 0.56. \end{aligned} \tag{2.102}$$

is obtained [27]. Calculations on the basis of QCD sum rules [28, 29] and the chiral quark model [30] yield similar results, albeit with large errors. The comparable result for the analogous function in the helicity basis, the axial charge introduced in Section 2.4.3, is

$$\begin{aligned} \Delta\Sigma &= \Delta u(x) + \Delta d(x) + \Delta s(x) \\ &= 0.64 + (-0.35) + (-0.11) \\ &= 0.18, \end{aligned} \tag{2.103}$$

which is in good agreement with the experimental data. The helicity contribution from lattice calculations is clearly suppressed compared to the expectation from the sum rules. In contrast, the transversity result is comparable with the result from the sum rules.

2.6.3 Experimental Access to Transversity Distributions

As indicated by the discussion in the previous section, the transverse spin distributions must be investigated in reactions in which at least one other hadron is involved in addition to the initial hadron state. This additional mass term brings a second chiral-odd function into the process, making the helicity-flip of the quark possible. This suppresses the process generally by a factor $\mathcal{O}(1/Q^2)$, making the detection of transverse effects considerably more difficult. There are several possibilities of introducing a second hadron into the reaction which shall be discussed here in the following paragraphs.

The Polarised Drell-Yan Process

In this process two polarised hadrons (protons or antiprotons) A and B scatter off one another. A lepton-antilepton pair is produced, as well as two unobserved hadronic end-states known collectively as X (Figure 2.10):

$$A^{\uparrow}(P_A) + B^{\uparrow}(P_B) \to l^{+}(l) + l^{-}(l') + X \tag{2.104}$$

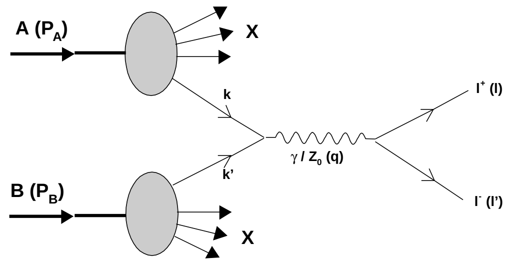

Figure 2.10: Schematic representation of the Drell-Yan process. A lepton-antilepton pair l^+l^- is produced in the scattering of two polarised hadrons A, B. The mediator of the reaction is a virtual photon or Z^0-Boson with four-momentum $q > 0$ corresponding to the invariant mass of the lepton-antilepton pair.

The cross-section for this reaction contains in leading order linear combinations of the product $\Delta_T q_A(x)\Delta_T q_B(x)$, thereby fulfilling as the product of two chiral-odd functions the requirement of a total chiral-even process. Although this mechanism allows a relatively clean extraction of the transversity distributions, the transverse asymmetry measured is expected to be extremely small and therefore subject to a large uncertainty. Experimental measurements using the transversely polarised Drell-Yan process are expected in the course of the next years from the detectors PHENIX and STAR at the relativistic heavy ion collider RHIC at the Brookhaven National Laboratory (BNL) in USA [31, 32]. New estimates suggest an asymmetry in this channel at PHENIX of 1-2% with a comparable statistical error [33].

Hadroproduction with a Transversely Polarised Target

In contrast to the Drell-Yan process only one of the hadrons in the initial state must be polarised here; instead a part h of the final state must be detected (semi-inclusive measurement):

$$A^{\uparrow}(P_A) + B(P_B) \to h(P_h) + X \tag{2.105}$$

The observation of a significant energy dependence in the single spin asymmetry

$$A_N = \frac{d\sigma^{\uparrow} - d\sigma^{\downarrow}}{d\sigma^{\uparrow} + d\sigma^{\downarrow}} \tag{2.106}$$

in this configuration at a beam energy of 200 GeV by the E704 collaboration at the beginning of the 1990s [34, 35] (Figure 2.11) triggered intense theoretical discussion as to the origin of the effect. More recent results from the E925 experiment at BNL seem to confirm the effect at a lower centre-of-mass energy of 22 GeV [36].

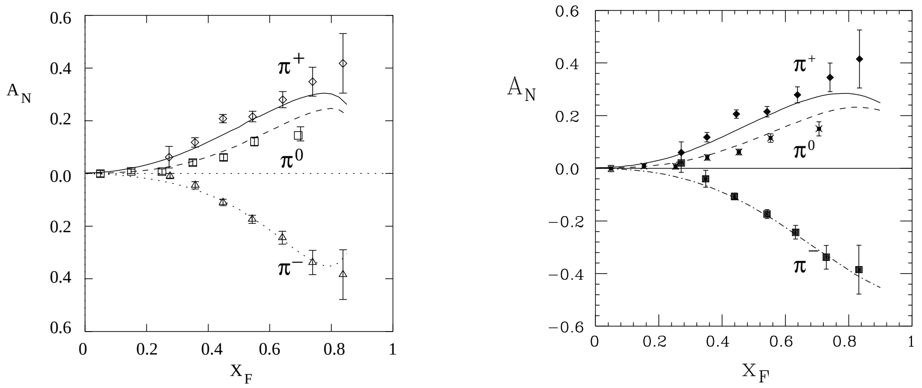

Figure 2.11: The single spin asymmetry measured by the E704 collaboration fitted for the Collins effect **(left)** and the Sivers effect **(right)**.

It remains unclear what mechanism is responsible for the effect measured by E704 and what combination of functions is contained in the asymmetry since it is expected from QCD that single spin asymmetries disappear at leading twist. One possible candidate is the mechanism suggested by Collins [37, 38] in which polarised quarks with finite transverse momentum fragment to unpolarised hadrons. In this case the asymmetry measured would be

$$A_N \sim \Delta_T q_i(x) H_1^{\perp}(z, \vec{k}_{\perp}^2) \tag{2.107}$$

where the individual functions are defined as in Section 2.6.1. In this case the transversity distribution would be made accessible through their coupling to the T-odd[4] Collins fragmentation function $H_1^{\perp}(z, \vec{k}_{\perp}^2)$[5]. The E704 asymmetry however exhibits a strong $\vec{k}_{\perp}$-dependence which cannot be explained fully by the Collins mechanism, although this effect otherwise describes the data well [39]. Another possible explanation is given by the so-called Sivers effect, which ascribes the observed asymmetry to an asymmetry in the transverse momentum of unpolarised quarks in a transversely polarised nucleon [40]:

$$A_N \sim f_{1T}^{\perp}(x, \vec{k}_{\perp}^2) D(z) \tag{2.108}$$

The T-odd distribution function $f_{1T}^{\perp}(x, \vec{k}_{\perp}^2)$ couples here with the unpolarised fragmentation function $D(z)$; should the Sivers mechanism be responsible for the asymmetry observed, then the E704 result would allow no access to the

[4]T-even (T-odd) refers to a function that is invariant (not invariant) under time-reversal

[5]The Collins effect is also the effect investigated though semi-inclusive DIS at COMPASS and will be dealt with more thoroughly in Section 2.6.4.

transversity distributions. Further experimental investigations are required using a third class of reactions where transversity should play a role, namely semi-inclusive leptoproduction. It is expected that in this channel the Sivers effect plays little or no role [21]; were an asymmetry to be measured here, it would most likely involve the transversity distributions.

Semi-inclusive Leptoproduction

There are four possibilities for gaining access to the transversity distributions through semi-inclusive DIS with a lepton beam [21]:

1. through the production of a transversely polarised hadron from a transversely polarised target nucleon;

2. through the production of an unpolarised hadron from a transversely polarised target nucleon;

3. through the production of two hadrons from a transversely polarised target nucleon;

4. through the production of an unpolarised or polarised spin-1 hadron from a transversely polarised target nucleon.

Previous experimental investigations in this area have concentrated on the second possibility, i.e. the measurement of azimuthal asymmetries in single pion production (the Collins effect). Such asymmetries have been measured at the SMC experiment at CERN with transversely polarised deuterium and proton targets [41] and by HERMES at DESY with a longitudinally polarised proton target [42, 43]. The latter does not allow access to the transversity distributions themselves, but does measure the Collins fragmentation function $H_1^{\perp}(z, k_{\perp}^2)$ which is of great importance for the phenomenology of transversity. Both measurements yielded first indications for a measurable Collins asymmetry which however must be regarded as inconclusive (see Figure 2.12). Measurements at HERMES with a transversely polarised target from 2002 and the data from COMPASS, the analysis of which is presented in Section 5, should produce more conclusive results.

2.6.4 The Collins Effect

Definition of the Collins Angle

Collins' eponymous effect, postulated by him in 1993 [37], deals with a possible asymmetry in the distribution of the transverse momentum vector $\vec{P}_{h\perp}$ of hadrons produced in a DIS process, an asymmetry which would allow inferences to be drawn concerning the transverse quark polarisation in a transversely polarised nucleon. For this effect to be observed, at least part of the hadronic end-product must be measured; a semi-inclusive measurement is required:

$$\vec{l}(k, \vec{s}) + \vec{N}(P, \vec{S}) \rightarrow \vec{l'}(k', \vec{s'}) + \vec{h}(P_h) + X \tag{2.109}$$

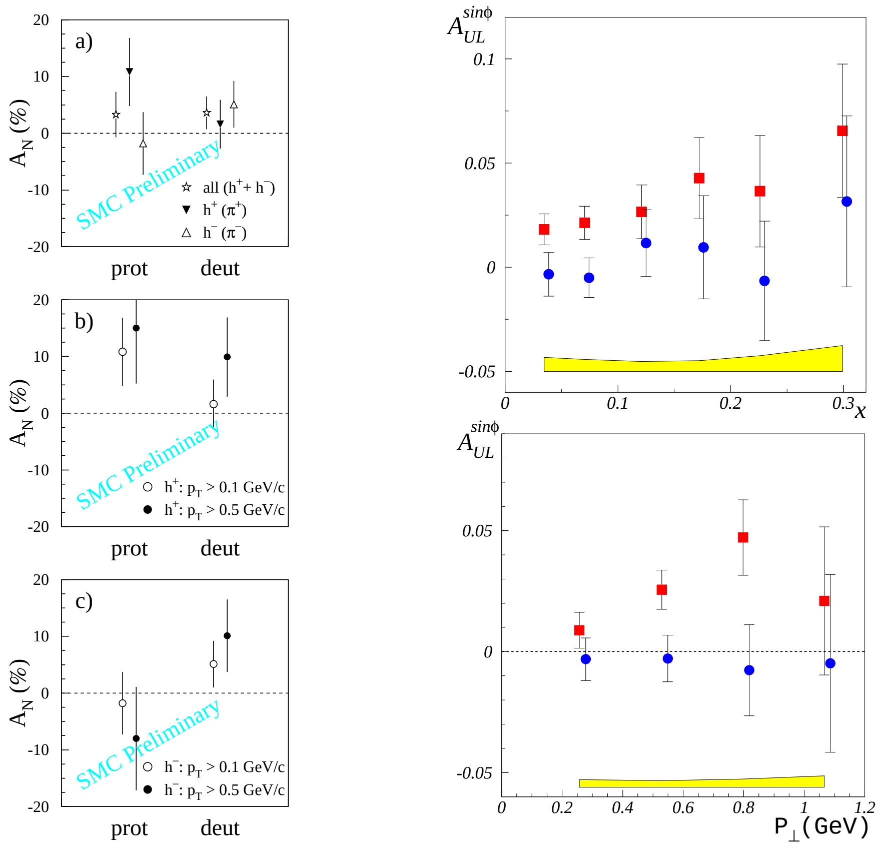

Figure 2.12: Previous measurements of the Collins asymmetry **(left)** SMC measurement: (top) $\pi^{\pm}$ in the entire kinematic range, (middle) π^{+} for $p_t > 0.1$ and $p_t > 0.5$, (bottom) π^{-} for $p_t > 0.1$ and $p_t > 0.5$; each for transversely polarised proton and deuterium target (left and right respectively in each picture) **(right)** HERMES measurement with longitudinally polarised proton target for π^{+} (squares) and π^{-} (circles): (above) versus x, (below) versus p_t; the systematic error is shown at the bottom of each plot.

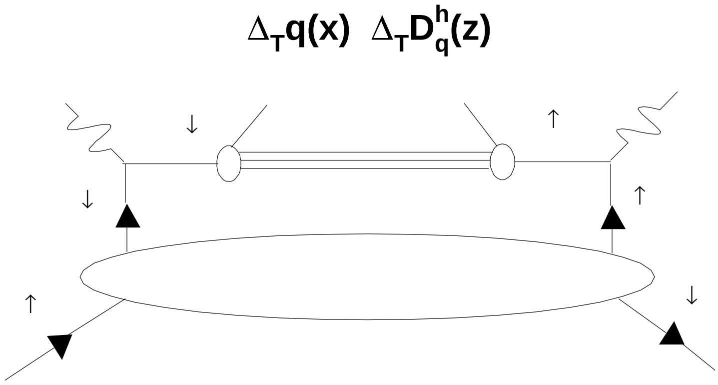

Figure 2.13: Access to the transversity functions through the detection of the hadronic end-product in DIS. The fragmentation process (upper loop in diagram) represents a second chiral-odd process, allowing the measurement of the helicity-flip channel.

In the terms of the discussion in Section 2.6.2, the observed hadron represents the source of a second chiral-odd function, enabling a total chiral-even process to be measured (Figure 2.13). This function, the Collins fragmentation function $H_1^{\perp}(z, \vec{P}_{h\perp}^2)$, corresponds to the fragmentation of a transversely polarised quark to an unpolarised hadron and is invariant under time-reversal (a T-odd function). Writing the probability of finding a hadron h with energy fraction z and transverse momentum $\vec{P}_{h\perp} = -z\vec{k}_{\perp}$ as $\mathcal{N}_{h/q}(z, \vec{P}_{h\perp})$, the Collins function can be expressed on the parton level by

$$\mathcal{N}_{h/q\uparrow}(z, \vec{P}_{h\perp}) - N_{h/q\downarrow}(z, \vec{P}_{h\perp}) = \frac{|\vec{k}_{\perp}|}{M_h} sin(\phi_k - \phi_{s\prime}) H_1^{\perp}(z, \vec{P}_{h\perp}^2) \qquad (2.110)$$

where ϕ_k and $\phi_{s\prime}$ are the azimuthal angles of the quark momentum and spin respectively in the hadronic end-product [21]. We choose a frame of reference in which $\vec{P}_h$ points along the z-axis. The angle $sin(\phi_k - \phi_{s'})$ is then given by

$$\sin(\phi_k - \phi_{s\prime}) = \frac{(\vec{k} \times \vec{P}_h) \cdot \vec{s\prime}}{|\vec{k} \times \vec{P}_h||\vec{s\prime}|} := \sin \phi_c \qquad (2.111)$$

and is known as the *Collins angle*. The azimuthal angle of the quark momentum in the final state is equivalent to that of the hadron with the largest momentum component of all hadrons produced in the fragmentation. This angle ϕ_h is in principle measurable. QED calculations can be used to show that the components of the quark spin in initial and final state ($\vec{s}$ and $\vec{s\prime}$) are related by [21]

$$s'_x = -D_{NN} s_x, \qquad s'_y = D_{NN} s_y \qquad (2.112)$$

where the factor

$$D_{NN} = \frac{2(1-y)}{1+(1-y)^2} \tag{2.113}$$

is the depolarisation factor familiar from (2.39) for the transverse case with the terms in γ suppressed. It follows from (2.112) that

$$\begin{aligned} \phi_{s\prime} &= \pi - \phi_s \\ \Rightarrow \phi_c &= \pi - \phi_s - \phi_h. \end{aligned} \tag{2.114}$$

Disregarding transverse quark motion in the target nucleon, in initial state the quark spin is parallel to the nucleon spin S; thus $\phi_s = \phi_S$ and

$$\phi_c = \pi - \phi_S - \phi_h \tag{2.115}$$

where ϕ_c is now defined entirely in terms of experimentally accessible quantities (Figure 2.14).

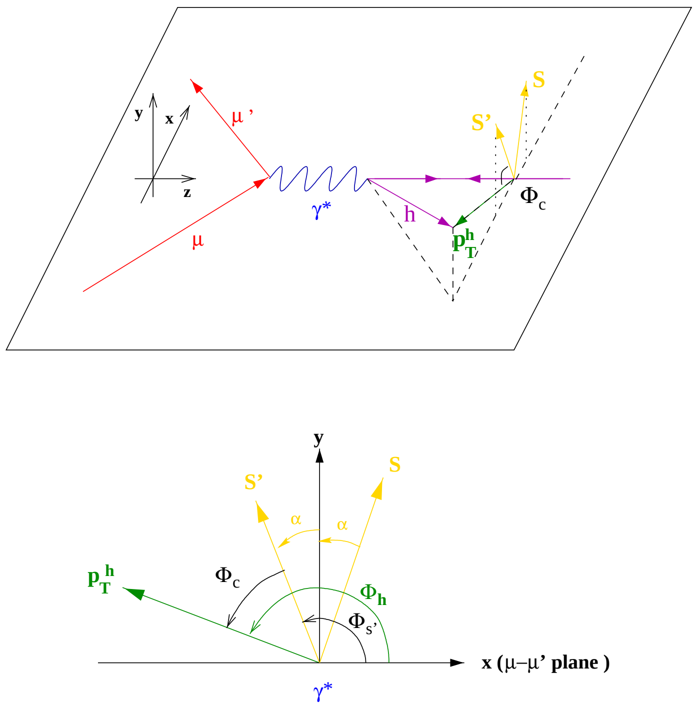

Figure 2.14: Angle definitions in the analysis of the Collins effect: **(above)** general view; **(below)** view along the x-axis.

Cross-section and Asymmetry in the Collins Effect

In order to obtain the cross-section asymmetry in the Collins process, one writes the DIS cross-section extended for a semi-inclusive process without integration over the hadron momentum $\vec{P_h}$ as (c.f. (2.14))

$$\frac{d^5\sigma}{dxdyd^3\vec{P}_h} = \frac{y\pi\alpha^2}{2E_h Q^4} L_{\mu\nu} W^{\mu\nu}. \tag{2.116}$$

The kinematic variables are those defined in Section 2.1. If the transverse component of the hadron momentum $\vec{P}_{h\perp}$ is small in comparison to the hadron energy E_h, the hadron momentum can be reduced to [21]

$$\frac{d^3\vec{P}_h}{2E_h} = \frac{1}{2z} dz d^2\vec{P}_h. \tag{2.117}$$

The azimuthal-dependent cross-section can thus be written

$$\frac{d^5\sigma}{dxdydzd^2\vec{P}_{h\perp}} = \frac{y\pi\alpha^2}{2zQ^4} L_{\mu\nu} W^{\mu\nu}. \tag{2.118}$$

The final hadron state is assumed to have either non-existent or unknown spin; through substitution of the appropriate lepton and hadronic tensors the expression

$$\begin{aligned} \frac{d^5\sigma}{dxdydzd^2\vec{P}_{h\perp}} &= \frac{s4\pi\alpha^2}{2zQ^4} \sum_i e_i^2 x \Big(\frac{1}{2}(1+(1-y)^2) q_i(x) D_i(z, \vec{P}^2_{h\perp}) \\ &+ \quad (1-y) \frac{|\vec{P}_{h\perp}|}{zM_h} |\vec{S}_\perp| sin(\phi_s + \phi_h) \\ & \qquad \times \Delta_T q_i(x) H^\perp_{1,i}(z, \vec{P}^2_{h\perp}) \Big) \end{aligned} \tag{2.119}$$

is obtained, where the summation is over all quark flavours. The transverse single spin asymmetry

$$\begin{aligned} A^h_T &:= \frac{d\sigma(\vec{S}_\perp) - d\sigma(-\vec{S}_\perp)}{d\sigma(\vec{S}_\perp) + d\sigma(-\vec{S}_\perp)} \\ &= \frac{2(1-y)}{1+(1-y)^2} \frac{\sum_i e_i^2 \Delta_T q_i(x) \Delta^0_T D_i(z, \vec{P}^2_{h\perp})}{\sum_i e_i^2 q_i(x) D_i(z, \vec{P}^2_{h\perp})} |\vec{S}_\perp| sin(\phi_s + \phi_h) \end{aligned} \tag{2.120}$$

may then be derived (c.f. (2.70)). It is plain to see that the factor $\sin(\phi_s + \phi_h)$ is also the sine of the Collins angle defined in (2.115). The fragmentation function measured, $\Delta^0_T D_i(z, \vec{P}^2_{h\perp})$, is related to the Collins fragmentation function through

$$\Delta^0_T D_i(z, \vec{P}^2_{h\perp}) = \frac{|P_{h\perp}|}{zM_h} H^\perp_{1,i}(z, \vec{P}^2_{h\perp}). \tag{2.121}$$

Disregarding unfavoured fragmentation functions (see Section 2.4.2) and assuming that the transverse sea quark polarisation is negligible, the following expressions for the fragmentation of a quark to a pion may be found using charge and isospin symmetry [44] (c.f. (2.60), (2.61)):

$$
\begin{aligned}
D_{\pi^+/u} &= D_{\pi^+/\bar{d}} = D_{\pi^-/\bar{u}} = D_{\pi^-/d} \equiv D_{\pi/q} && (2.122)\\
2D_{\pi^0/u} &= 2D_{\pi^0/\bar{d}} = 2D_{\pi^0/\bar{u}} = 2D_{\pi^0/d} \equiv D_{\pi/q} && (2.123)\\
D_{\pi^+/\bar{u}} &= D_{\pi^+/d} = D\pi^-/u = D_{\pi^-/\bar{d}} \approx 0 && (2.124)
\end{aligned}
$$

The Collins asymmetry from (2.120) simplifies in single pion production (pion charge $i \in \{+, 0, -\}$) therefore to

$$
A_T^{\pi^i} = D_{NN} \frac{\Delta_T q(x)}{q(x)} A_q^{\pi^i}(z, p_t) |\vec{S}_\perp| \sin \phi_C \tag{2.125}
$$

where the depolarisation factor D_{NN} is defined according to (2.113) and the *analysing power* of the reaction, $A_q^\pi(z, p_t) = |\Delta_T^0 D_{\pi/q}|/D_{\pi/q}$, is defined as the ratio of transverse and unpolarised fragmentation functions. The measured quantity is therefore a product of a z-dependent fragmentation function and the desired transversity distribution $\Delta_T q(x)$ (normalised to the unpolarised distribution function $q(x)$), a function of x. This factorisation allows the measurement of the transversity distributions up to a normalisation given by the analysing power. Measurements of the analysing power are discussed in the next section.

Analysing Power

The Soffer bound introduced in (2.100) represents an upper limit for the ratio $\Delta_T q(x)/q(x)$ with the help of which a lower bound for the analysing power can be found using the experimental data from SMC and HERMES mentioned in Section 2.6.3 (Figure 2.12). The SMC data yield a value [44, 41]

$$
|A_q^\pi(\langle z \rangle, \langle p_t \rangle)| \geq 0.26 \pm 0.14, \qquad \langle z \rangle \sim 0.45, \langle p_t \rangle \sim 0.65 GeV/c \tag{2.126}
$$

and HERMES [42, 43]

$$
|A_q^\pi(\langle z \rangle, \langle p_t \rangle)| \geq 0.20 \pm 0.04(stat.) \pm 0.04(sys.), \qquad z \geq 0.2. \tag{2.127}
$$

These values suggest a significant Collins effect. In [45, 46] an equivalent value is cited on the basis of the HERMES results and the chiral soliton model:

$$
|A_q^\pi(\langle z \rangle, \langle p_t \rangle)| = \frac{\langle H_1^\perp \rangle}{\langle D \rangle} \geq 0.138 \pm 0.028, \qquad \langle z \rangle \sim 0.4 \tag{2.128}
$$

It should be noted that the theoretical situation regarding the HERMES measurement has not yet, because of the longitudinal target polarisation and possible twist-three effects which could also be responsible for the asymmetry, been completely understood.

An independent measurement of the Collins fragmentation function is achieved with data from semi-inclusive two hadron production in electron-positron scattering $e^- e^+ \rightarrow h_1 h_2 X$ [21]. The differential cross section for this reaction

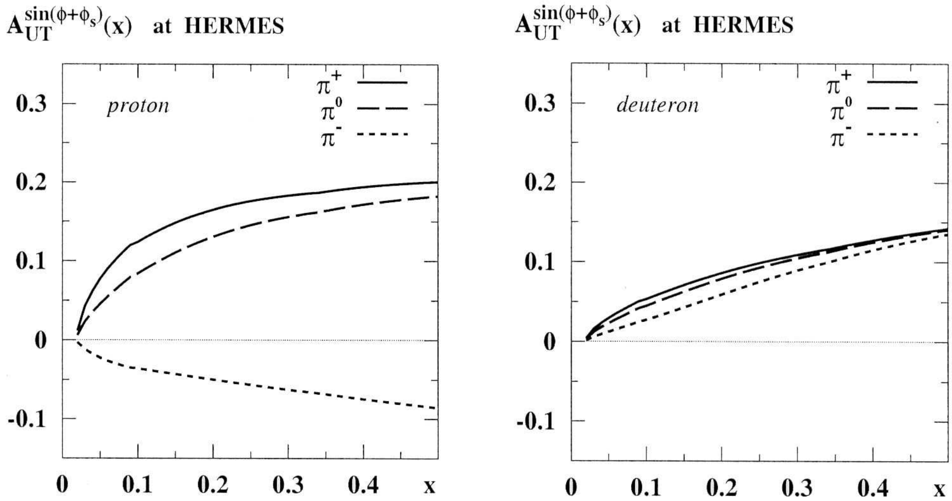

Figure 2.15: Predictions for the x-dependence of the Collins asymmetry at HERMES with a transversely polarised proton **(left)** and deuteron **(right)** target [47]. Measurements were performed with a proton target in the HERMES run in 2002.

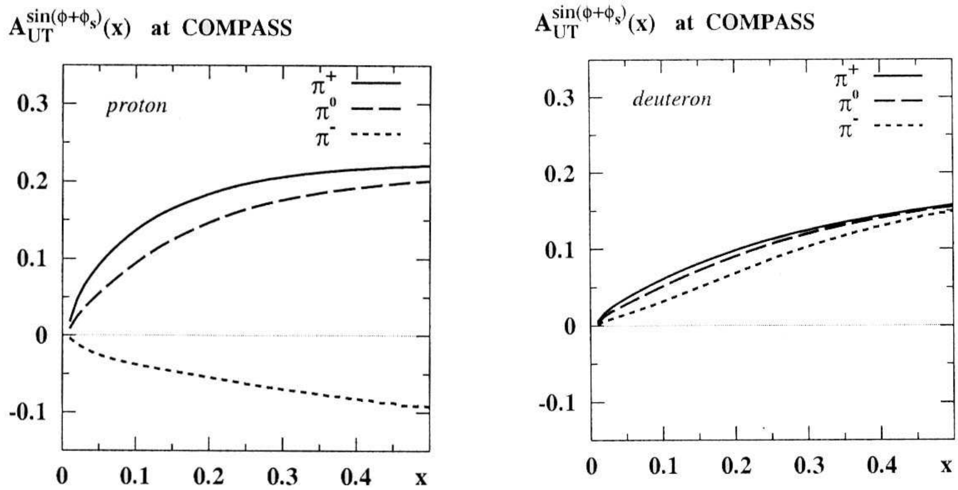

Figure 2.16: Predictions for the x-dependence of the Collins asymmetry at COMPASS with a transversely polarised proton **(left)** and deuteron **(right)** target [47]. Measurements were performed with a proton target in the COMPASS run in 2002.

depends on the product of two Collins fragmentation functions for the two hadrons involved. Using data from the DELPHI experiment at CERN, a value for the analysing power of

$$|A_q^\pi(\langle z \rangle, \langle p_t \rangle)| = \left| \frac{\langle H_1^\perp \rangle}{\langle D \rangle} \right| \geq 0.0125 \pm 0.014, \qquad \langle z \rangle \sim 0.4 \tag{2.129}$$

is obtained.

Experimental Predictions

According to (2.125) an counting rate asymmetry in the angle of production of a pion of a particular charge is expected which should show a sine-dependence when plotted against the Collins angle ϕ_C. The amplitude of this sine wave corresponds to the pre-factor in (2.125) which contains the target polarisation (known or calculated experimentally), the depolarisation factor (to be calculated from the kinematics of the scattering process), the analysing power and the normalised transversity distribution. These four quantities are all smaller than one; a raw asymmetry greater than a few percent would therefore be surprising [44]. It can also be qualitatively predicted that the asymmetry should become larger [37, 38]

- at larger values of x, since in this case the fragmenting quark is highly polarised;
- at larger values of z, since here with high probability the quantum numbers of the hadron follow those of the fragmenting quark;
- for π^+ production with a proton target, since here the target nucleon and the hadron have a common u valence quark.

The only theoretical calculations specific to the HERMES and COMPASS experiments deal with the x-dependence of asymmetry [47] and are shown in Figures 2.15 and 2.16.

Chapter 3

The COMPASS Experiment

COMPASS is a fixed-target experiment on the M2 beam-line of the Super Proton Synchrotron (SPS) at the European Nuclear Research Centre, CERN, on the Franco-Swiss border near Geneva. Measurements are planned with high energy muon and hadron beams [17]. In the first phase of the experiment, which began in Summer 2002 after installation of the equipment in 2000 and 2001 and is planned to continue until the SPS pause in 2005, only the muon beam will be used, apart from in a short hadron beam test-phase in 2004. The following discussions restrict themselves therefore to those elements with are of importance for the muon physics programme. Following an initial discussion of the beam and accelerator properties, the COMPASS polarised target will be introduced. Further sections deal with the various types of detectors employed for particle tracking and identification. The chapter ends with a description of the trigger and data acquisition systems.

3.1 The SPS 160 GeV Polarised Muon Beam

The SPS is the second largest accelerator ring at CERN with a circumference of some 7 km (Figure 3.1). A proton beam with 26 GeV energy and a rate of $3.4 \cdot 10^{13}$ per cycle is initially injected from the smaller Proton Synchrotron (PS) into the SPS, in which it is accelerated over several cycles to approximately 400 GeV, extracted, and directed onto the T6 Beryllium target head. One SPS cycle lasts 16.8 seconds, consisting of 11.7 s injection and acceleration time and 5.1 s extraction time, the so-called "spill".

The length of the T6 target is under normal experimental conditions 500 mm, but can be reduced in steps from the control-room of the experiment down to 40 mm [48], when for example detector studies demand a lower beam intensity. A secondary beam, consisting principally of protons, kaons and pions, is produced in the target [49]; these are then fed into the M2 beam-line where they are selected for momentum by a first spectromagnet. Over a length of 600 m the majority of the kaons and pions decay to muons. The other hadrons are filtered out by a beryllium absorber with a total length in the direction of the beam of 10 m. The intensity of the muon beam, now with a hadronic impurity

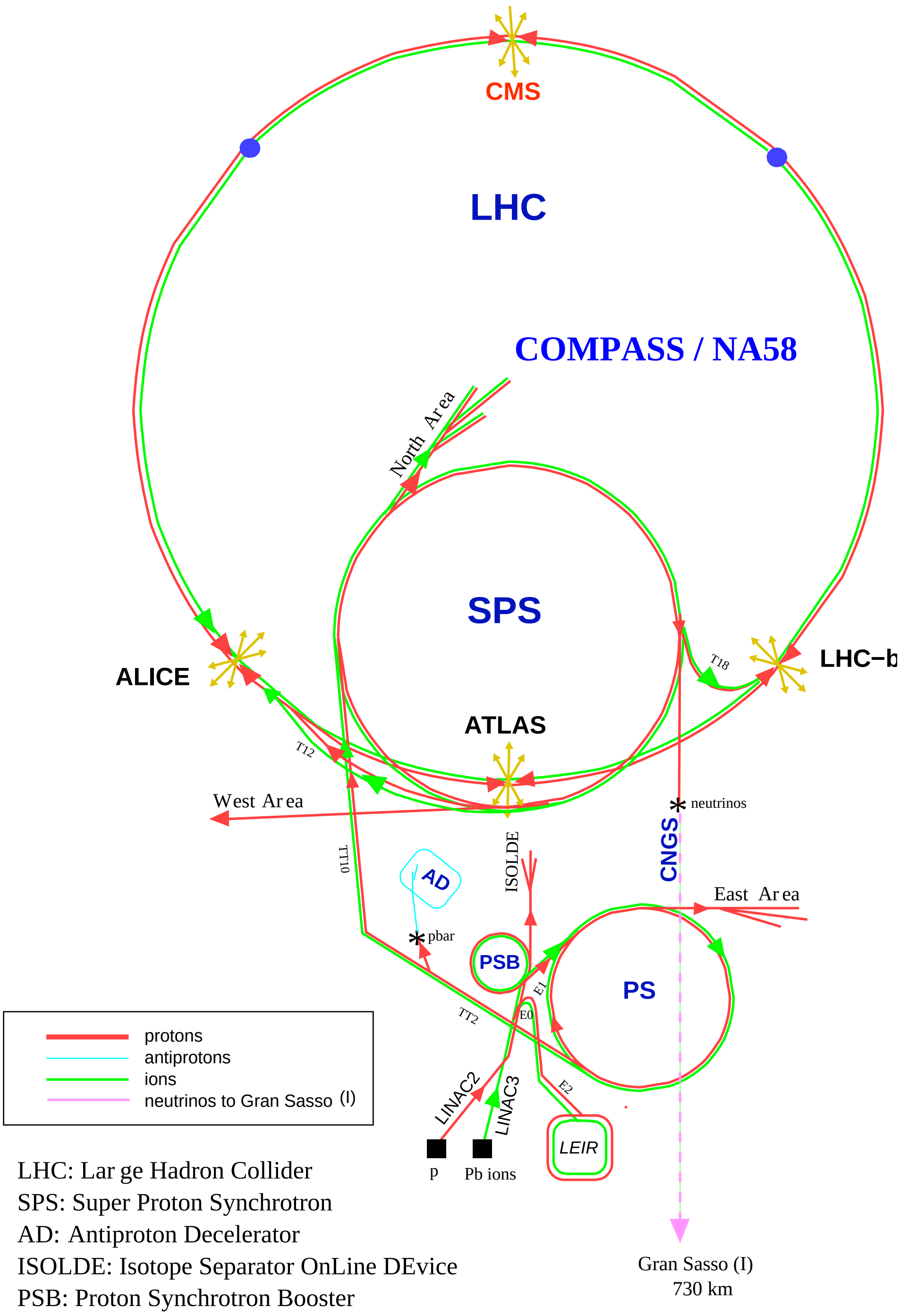

LHC: Large Hadron Collider
SPS: Super Proton Synchrotron
AD: Antiproton Decelerator
ISOLDE: Isotope Separator OnLine DEvice
PSB: Proton Synchrotron Booster
PS: Proton Synchrotron
LINAC: LINear ACcelerator
LEIR: Low Energy Ion Ring
CNGS: Cern Neutrinos to Gran Sasso

Figure 3.1: The CERN accelerators (not to scale). The COMPASS Experiment is on the M2 beam-line of the second largest accelerator, the SPS.

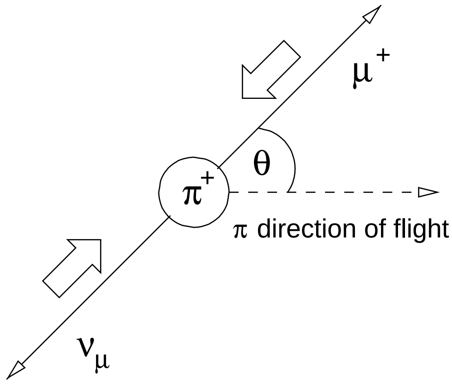

Figure 3.2: Maximal parity violation in the weak decay of a pion. The left-handedness of the neutrino determines the helicity of the muonic decay product.

of only approximately 1%, is about $2 \cdot 10^8$ particles at full target length. After further momentum selection by magnets in the 800 m long beam tunnel leading to the COMPASS experimental hall in Building 888 in the North Area of the CERN site at Prevessin (France) the average energy of the beam particles is around 160 GeV.

The maximal parity violation of the weak decay of kaons and pions to muons, e.g. $\pi^+ \to \mu^+\nu_\mu$ determines the direction of polarisation of the muons produced. As a consequence of the left-handedness of the neutrino (momentum and spin antiparallel, helicity $= -1$), the spin and momentum of the muon must also be antiparallel in the rest-frame of the decaying pion in order to maintain spin and momentum conservation for the decay (Figure 3.2) [50, 51]. The value of the naturally-occurring polarisation of the muon beam depends on the relative energy of muon and pion through

$$P_\mu = \frac{m_\pi^2 + m_\mu^2(1 - \frac{2E_\pi}{E_\mu})}{m_\pi^2 - m_\mu^2}, \tag{3.1}$$

where $E_{\pi,\mu}, m_{\pi,\mu}$ are the energy and the mass of the muon and the pion respectively. With beam momenta calculated from Monte Carlo simulations, $p_\pi = 177GeV/c$ and $p_\mu = 160GeV/c$ [52], a value $E_\mu/E_\pi \approx 0.9$ is found together with an average polarisation

$$P_\mu = -0.75 \pm 0.04. \tag{3.2}$$

Since the calculated values are in good agreement with the values measured at COMPASS' precursor, the SMC experiment [53, 54], the beam polarisation is not measured independently at COMPASS.

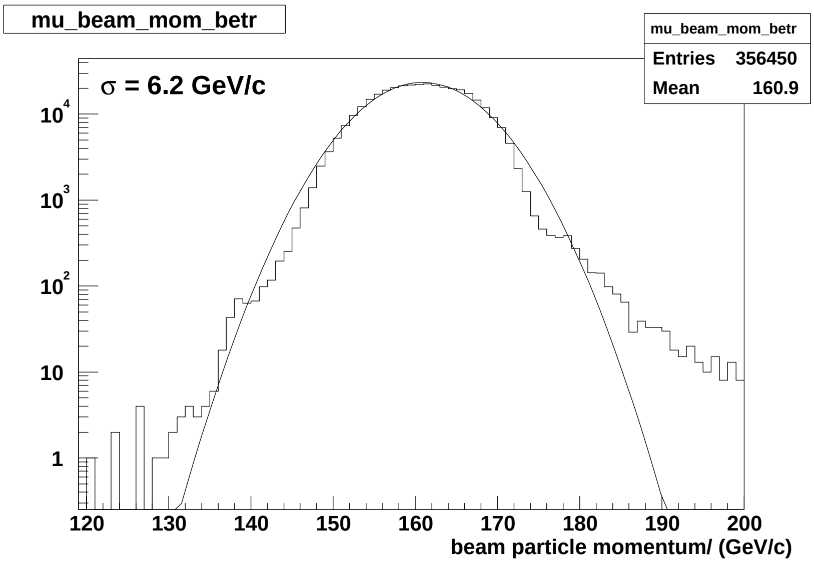

Figure 3.3: Logarithmic depiction of the momentum distribution of the beam particles as measured by the Beam Momentum Station, with superimposed Gauss fit. The average momentum of the beam particles is $160GeV/c$, the 1σ-width of the fit $6GeV/c$

3.2 Measurement of the Beam Properties

In order to determine precisely the momentum of each incoming muon, the beam must be measured before it hits the COMPASS target. Four planes of the Beam Momentum Station (BMS) perform this task, two before and two after the last bending magnet in the mouth of the tunnel where the beam is guided up a slight incline into the experimental hall. These planes consist of plastic-scintillator hodoscopes each with 64 channels orthogonal to the beam direction, which are read out by single-channel photomultipliers. The curvature of the tracks in the magnetic field can be used to ascertain the particle momentum to an accuracy of around 0.5%.

During the 2002 beam-time it was discovered that the BMS stations, which had been to a great extent taken over unmodified from the precursor SMC experiment, exhibited a relatively low efficiency with often only two or three co-ordinates could be determined from a passing particle. Although three spatial points are sufficient to determine a particle's momentum, a test of the compatibility of the points through the calculation of a spatial χ^2 requires an additional co-ordinate. As a result, only in around 47% of all events could a track be unambiguously reconstructed. In a further 22% of the cases there was more than one possibility; in the remaining 31%, no track could be reconstructed.

By swapping sub-optimal photomultipliers during the beam-time in 2003, it was possible to improve the situation somewhat. In order to improve the redundancy, a fifth plane between the first two was commissioned towards the end of the beam-time; this plane's photomultipliers exhibited however a relatively bad time-resolution of $\sigma \approx 900ps$. The construction of further BMS planes with multi-anode photomultipliers as used at COMPASS in the scintillating-fibre hodoscopes (see Chapter 4) is planned.

3.3 The Polarised Target

Access to all terms of the DIS cross-section can only be achieved with polarised beam and target (c.f. Section 2.2). At COMPASS the deployment of two different solid targets is planned for the different physics programmes: an ammonium (NH_3) target for the proton-physics programme and a lithium deuteride (^6LiD) deuterium target for the muon programme. In the first phase of COMPASS only the ^6LiD target is used.

3.3.1 Construction and Operation

The target material is contained within two cells separated by a microwave-impermeable wall. The cells are cylindrical with a radius of 15 mm and a length of 600 mm each. They are surrounded by a homogenous 2.5 T magnetic field maintained by a superconducting solenoid magnet. Following continuing difficulties with the completion of a specially-developed apparatus, COMPASS is using the SMC target magnet in the first few years of running. This magnet has a significantly smaller acceptance of ±70 mrad as against the ±160 mrad originally planned [55, 56]. This setback was partially compensated by raising the beam energy to 160 GeV from 100 GeV, so that the acceptance for e.g. open-charm production is still 73% as opposed to the 100% intended.

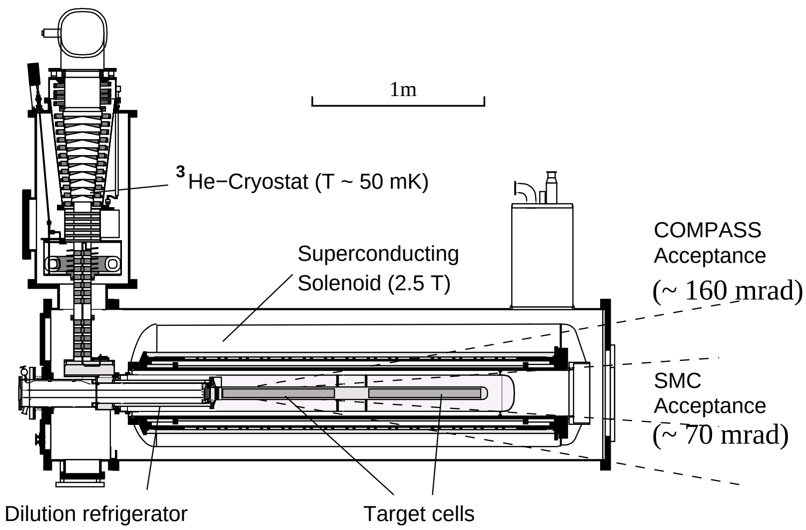

Figure 3.4: The COMPASS polarised target (cross-section). The acceptance achieved with the SMC magnet compared to the planned acceptance is shown.

The entire target apparatus is enclosed in a cryostat with a working temperature of about 50 mK (Figure 3.4) [57]. Low temperature T and a strong magnetic field B are important preconditions for achieving a maximal polarisation P of the target material, since this is given by Curie's Law through

$$P = tanh(\frac{\mu B}{kT}), \tag{3.3}$$

where μ is the magnetic moment of the polarisable target particle (proton or electron), and k is the Boltzmann constant. Thus the degree of polarisation of an electron at a temperature of a few hundred mK and a magnetic field of 2.5 T is almost 100%, whereas that of the proton, because of its variant magnetic moment, is only 0.5%

The polarisation is itself is performed by the method of dynamic nuclear polarisation (DNP) [58]. In preparation, 20 MeV electrons are injected into the target material at a temperature of 200-300 mK. The high electron polarisation can be transferred to the protons through microwave irradiation of a suitable frequency close to the spin resonance frequency of the electron. This process continues for so long as all proton spins are pointing in the same direction as the electron spins. Once the desired polarisation has been achieved, the spin configuration can be "frozen" by cooling the target to 50 mK.

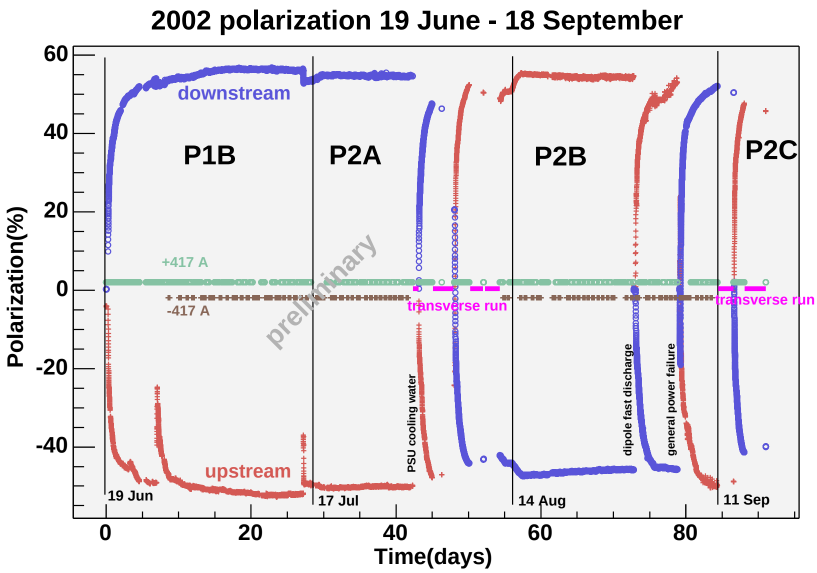

Figure 3.5: Evolution of the polarisation during the 2002 beam-time (from [59]). The various polarisation losses are in part due to preparation for transverse measurement; a water leakage and a general power-cut also led however to short losses of polarisation. N.B.: The periods P1B etc. are SPS periods, and do not correspond to the similarly-named COMPASS data-taking periods mentioned in the analysis section.

The two target cells are always operated with opposing polarisation, in the normal longitudinal case parallel or antiparallel to the beam direction. This reduces false asymmetries which arise through long-term variations in the beam intensity if one measures in two long periods with the same configuration. Other sources of error which could be caused by this mode of operation, for example from the variant acceptance and differing elementary constituents of the two cells, are reduced to a minimum by reversing the polarisation of the two cells occasionally. In normal, undisturbed experimental operation this is performed around every eight hours through simultaneous flipping of the magnetic field in both cells. In this way stable polarisations of around +57% and -49% could be achieved during the beam-time in the Summer of 2002 (Figure 3.5) [60].

3.3.2 Transverse Polarisation

At COMPASS it is also possible to polarise the target nucleons transversely to the beam direction using a 0.5 T transverse dipole-magnet field. The target polarisation is first brought up to a stable high level in longitudinal mode before the dipole field is switched on. Since the nucleons are frozen at 50 mK, their very long relaxation time may be used to measure with transverse polarisation. Through reversal of the dipole field the polarisation can be flipped simultaneously in both cells.

The data for the measurement of the Collins asymmetry, the analysis of which is the subject of Chapter 5 of this thesis, were taken in the transverse target configuration.

3.4 Detectors for Track Reconstruction

The layout of the COMPASS experiment with its two spectrometer stages is shown in Figure 3.6[1]. The large-angle spectrometer immediately after the target detects reaction particles that have been scattered at large angles of up to 180 mrad. The small-angle spectrometer investigates particles of higher energy that have been scattered at smaller angles of under 30 mrad. Both spectrometer stages are equipped with detectors for track reconstruction and particle identification as discussed in the following sections. Each spectrometer stage also possesses a magnet for momentum selection, SM1 and SM2 respectively. SM1 enables the measurement of particles of lower momentum and has an integrated field-strength of 1.0 Tm. SM2, in accordance with the higher momentum of the particles with which it has to deal, has a higher integrated field-strength of 4.4 Tm.

As a result of the varying demands made on, among other things, temporal and spatial resolution in different areas of the spectrometer, a wide range of different

[1] This and following discussions use the COMPASS co-ordinate system, in which z is the direction along the beam axis, and x and y are the horizontal and vertical transverse axes respectively. The terms *Salève* and *Jura* are also used to describe the right and left sides of the hall (in beam direction); the names are taken from the mountain ranges in the Geneva region which are to be found at some distance on the respective sides of the hall.

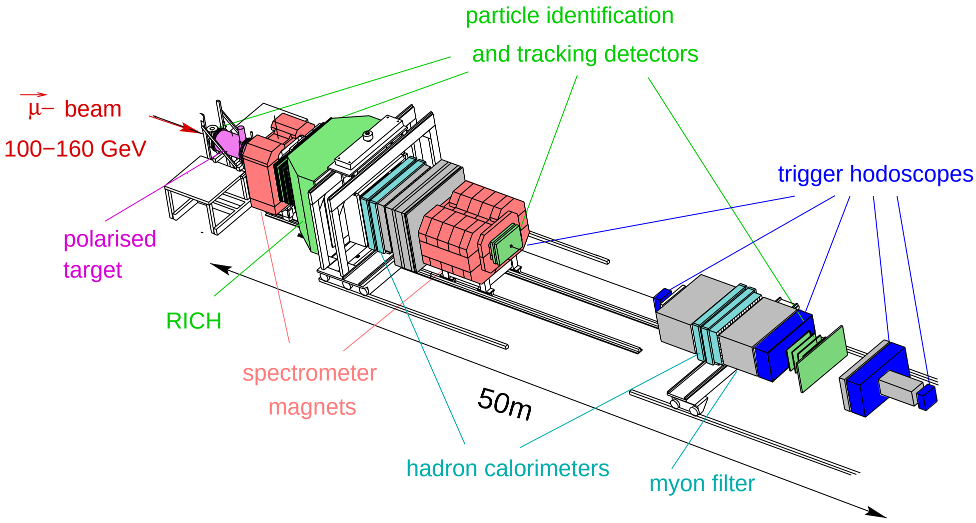

Figure 3.6: The COMPASS Spectrometer : layout for the first phase 2002-4. For the second phase of the experiment from 2006, the installation of further detectors is planned.

detector technologies is deployed in COMPASS. These are roughly divided into three groups according to the angular range in which they operate [17].

1. Detectors situated directly in the beam region for the detection of particles deflected at very small angles, the *very small area tracking* (VSAT) detectors. These require good time-resolution and short dead-time because of the high rates they have to withstand. In the area around the target they must also possess a good spatial resolution of around 50 μm, in order to be able to reconstruct interaction vertices as precisely as possible. These duties are performed at COMPASS by scintillating-fibre hodoscopes and silicon micro-strip detectors.

2. *Small area tracking* (SAT) detectors are used for particles deflected at slightly larger angles, where the requirements especially for time resolution are not so stringent. Two similar novel detector technologies are used: micro-mesh gas detectors (*Micromegas*) and gas electron multipliers (*GEMs*)

3. Finally, particles deflected at greater angles are detected by the *large area trackers* (LAT). A combination of multi-wire proportional chambers (*MWPCs*) and drift chambers, including the novel *Straw* drift-tube detectors is used.

The various detector types are introduced in more detail in the following sections.

3.4.1 Scintillating-Fibre Hodoscopes (SciFis)

There are altogether eight hodoscope stations (abbreviation "FI") using scintillating-fibre technology placed throughout the COMPASS spectrometer, the task of which is to detect minimally deflected particles. Two of these (FI01 and 02) are immediately in front of the target, two (FI03 und 04) immediately behind it. Two more are situated in the middle spectrometer region between the spectrometer magnets SM1 and SM2, and two behind SM2. Since work towards the commissioning and maintenance particularly of the hindmost four stations forms a significant part of this thesis, the construction and operating principles of these detectors are dealt with more closely in Chapter 4.

3.4.2 Silicon Micro-Strip Detectors

A total of three silicon micro-strip detector stations are situated in the immediate target vicinity. The determining factor in their use at COMPASS is their excellent spatial resolution of about 14.4 μm, brought about by their closely spaced anode structures (15 μm distance between strips, 50 μm strip width). Each of three stations consists of two planes and each plane of two projections that are read out simultaneously. The second projections are rotated by 2.5° in order to obtain additional spatial information for the resolution of combinatorial ambiguities. Two planes one after the other therefore cover a stereo angle of 5° [61]. The active area covers 70 mm x 50 mm.

As a result of the drift time of the electrons, the time-resolution of the silicon detectors is only moderate, around 3ns. For this reason they are placed together with the SciFi detectors, which possess a higher time-resolution, so that the demands on both spatial and temporal resolution can be fulfilled in the beam region.

3.4.3 Micromega Detectors

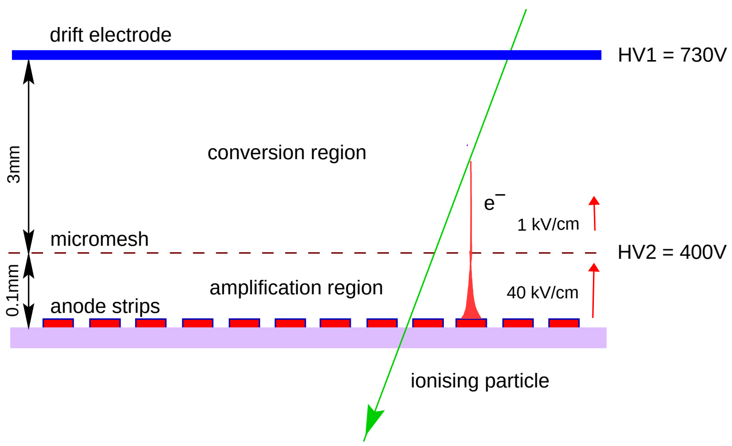

Figure 3.7: Sketch of a Micromega detector. Electron-ion pairs are produced in the conversion region before passing the micro-mesh and generating an electron avalanche in the amplification region.

The Micromega detectors also use micro-strips; they are however gas-filled rather than semiconductor detectors. The technical innovation of the Micromega detectors developed in Saclay (Paris) rests with the micro-mesh that divides the detector's interior into two regions. The space charge induced by the passing particle is first collected in a 2.5 mm thick conversion region and guided to the the micro-mesh by a moderate electric field of around 1 kV/cm. On the other side of the micro-mesh is the 100 μm thick amplification region, which underlies a much higher potential difference of some 50 kV/cm . An electron avalanche is initiated in this area, reaching the read-out strips within a very short time ($\approx 100\ ns$). The advantage of this method is that the signal length on the cathode is maximally equal to this drift-time in the amplification region [62, 63], so that the micromegas exhibit an improved rate-capability and a time-resolution of around 8 ns.

There are three Micromega stations in the area behind the target, each with x- and y-projections and u- and v-projections rotated by 45^o. The total active area covered by the projections of a station measures 40 cm x 40 cm.

3.4.4 GEM Detectors

The GEM detectors are similar in their construction to the Micromegas described in the preceding section. They also work according to the principle of electron multiplication in a strong electric field. Instead of the micro-mesh they have in their interior up to three capton foils of 50 μm thickness, each covered with 5 μm copper coating. A "honeycomb" system of 70 μm-diameter holes is cauterised into these foils at a spacing of 140 μm. The ionising particles passing through the first drift volume are multiplied several times in the region of the holes in a very strong electric field (the two sides of a foil are under a potential difference of 200V) up to a factor of twenty. The resultant electron avalanche arrives on anode strips with a pitch of 400 μm that are read out in two dimensions. The spatial resolution of the GEMs is around 50 μm, the time-resolution around 15 ns as a result of the slow secondary multiplication processes [64].

10 GEM stations are to be found throughout the spectrometer. Each has two planes and thereby four projections with simultaneous read-out. Their active area measures 316 mm x 316 mm. The supply voltage is reduced in the central area with high rates to avoid damage to the chambers [65].

3.4.5 Multi-Wire Proportional Chambers (MWPCs)

MWPCs are used throughout the rear of the COMPASS spectrometer to detect particles that have been scattered at large angles. Three chambers are to be found in the large-angle spectrometer between the two magnets SM1 and SM2, three immediately behind SM2 and a further five right at the back of the small angle spectrometer. An x projection and two projections rotated by 45^o, u and v, are read out from each station; these are part of the same mechanical structure or hang separately but in immediate juxtaposition.

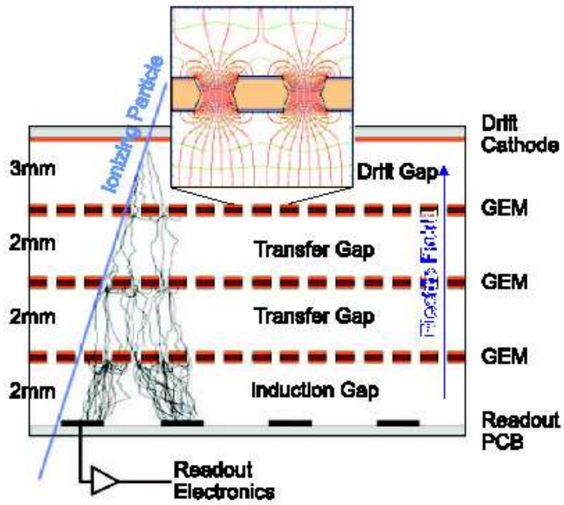

Figure 3.8: A GEM detector. Electron-ion pairs are produced in the drift volume and multiplied by the high field gradient in the holes of the canton foil so that a measurable signal is produced.

The MWPCs use the principle of the formation of a charge-cloud when an ionising particle travels through a counting gas (74% Ar, 20% CF_4, 6% CO_2) and its conversion to an electronic pulse in anode wires suspended between two cathode planes. The spatial resolution is around 700 μm with a spacing between wires of 2 mm. Because of the low rates in the areas covered by the MWPCs outside the beam region, exact time information is not required. In order to save on read-out electronics for the over 24 000 channels, only the number of the channels where hits have been registered is recorded. A dead region of a few centimetres' diameter masks the beam itself.

3.4.6 Drift Chambers

COMPASS uses in the large-angle spectrometer three "Saclay" drift chambers with four projections each. Their active area measures 1.2 m x 1.2 m with a wire spacing of some 7 mm. The mixture of Ne (45%), C_2H_6 (45%) and CF_4 (10%) gases makes amplification by a factor around $2 \cdot 10^4$ and a drift-time of 70 ns possible with a supply voltage of 1750 V. A dead region of 30 cm diameter covers the beam. For the COMPASS beam-time in 2003 four "W4-5" drift chambers originally used in the EMC experiment were installed behind SM2. They consist of four projections with a dead region of between 0.5 and 1.0 m diameter around the beam.

detector type	channels	time-resolution	spatial resolution
SciFi (target region)	1152	450 ps	120 μm
SciFi (spectrometer)	1420[2]	370 ps	200 μm
Silicon	6144	2-4 ns	14 μm
Micromegas	12288	9.4 ns	92 μm
GEMs	21504	12 ns	50 μm
Drift Chambers	1526	-	250 μm
Straws	2688	-	300 μm
MWPC	24576	-	500 μm
W 4-5	2000	-	1900 μm

Table 3.1: Overview of detectors for track reconstruction with their temporal and spatial resolution in the beam-time of 2003. No time information is demanded from the large angle detectors.

3.4.7 Straw Drift Tubes

The novel "Straw" detectors use the same principle as normal drift chambers, with the difference that the anodes take the form of wires held taut in a conducting tube of graphite-coated capton foil with a diameter of 6.04 mm (in the inner region close to the beam) or 9.51 mm (outer region). They operate with the same gas mixture as the MWPCs (74% Ar, 20% CF_4, 6% CO_2). A dead region with a size determined by the active area of the neighbouring GEM detectors (around 30 cm) spans the immediate beam region [66].

The Straw layers are compounded to double layers with one displaced by half the diameter of a tube. Planes reading out in x and y are combined with a third plane rotated at 10° to the vertical to form a station. The active area of the x-planes measures 3.25 m x 2.44 m, of the other planes 3.25 m x 2.77 m. The spatial resolution is a few hundred micrometres.

3.5 Detectors for Particle Identification

The detectors described in the previous section all measure points in space and some cases time; using this information together with the expected deflection of particle tracks in the fields of the spectrometer magnets SM1 and SM2, the momentum of the particles concerned can be determined. In order to be able to distinguish particles of different types, knowledge of their energy or velocity is also however required. A range of different detectors introduced in the following sections perform this task. A RICH[3] detector allows the determination of the velocity of the particles in transit and thereby their mass, provided their momentum is known. Hadron calorimeters are used to determine hadron energies. So-called muon filters allow the unambiguous identification of muons.

[2]detector channels; with double-precision 2840 read-out channels

[3]**R**ing **I**maging **Č**erenkov

3.5.1 The RICH Detector

A particle moving at a speed v greater than the speed of light in a particular medium produces a cone of photons. The angle, θ_C, at which this Čerenkov-Licht is emitted is given by

$$cos\theta_C = (\beta \cdot n)^{-1} \tag{3.4}$$

where n is the refractive index of the material and $\beta = v/c$ (speed of light *in vacuo* c). If the momentum of a particular particle is known, its mass can thus be determined by measuring θ_C.

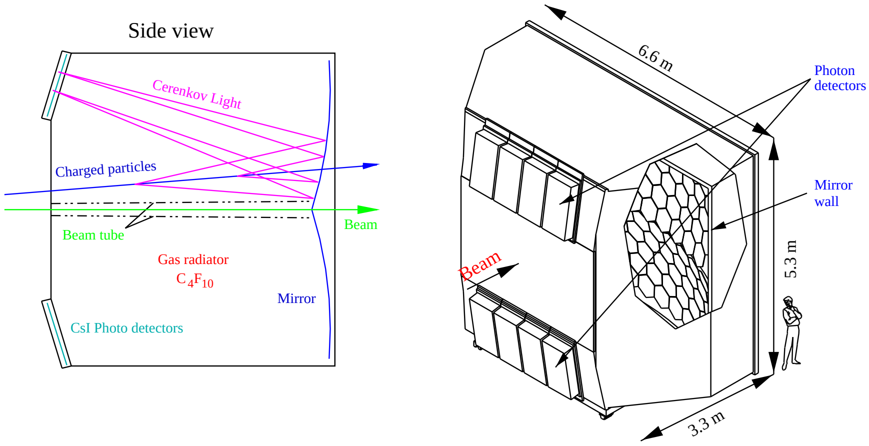

Figure 3.9: The RICH Detector (side and outside views). Čerenkov light is emitted in the direction of flight of the particle and mapped via the mirror wall as a ring onto the detector layers.

The COMPASS RICH detector must be capable of separating kaons, pions and protons up to energies of 60 GeV [67, 68]. The interior of the RICH is approximately 3.3 m long in the beam direction, with a width of 6.6 m and a height of 5.3 m (Figure 3.9), and is filled with C_4F_{10} gas with a refractive index of 1.00153. The threshold energy for the emission of Čerenkov light is 2.5 GeV for pions, 8.9 GeV for kaons and 17 GeV for protons. The back wall of the RICH interior ("downstream" in the direction of the beam) is slightly curved and covered in mirrors. Photons are emitted at a angle characteristic of a particular type of particle are reflected on this wall and thereby focussed onto the front wall. This is coated with photo-sensitive CsI divided into pixels measuring 8mm x 8 mm. Electrons are produced via the photo-effect at those pixels where a photon arrives and are converted into a measurable signal by multi-wire proportional chambers. The activated pixels form a ring, the radius r of which is determined by the transit speed of the original particle through the detector according to

$$r = \frac{R_s}{2} \arccos(\frac{1}{\beta n}), \tag{3.5}$$

where R_s is the radius of curvature of the mirror wall [69]. A typical ring is shown in Figure 3.10.

Currently only the large-angle spectrometer of COMPASS is equipped with a RICH. For the second phase of the experiment a further RICH of similar construction but with photomultiplier read-out is planned for the second spectrometer stage.

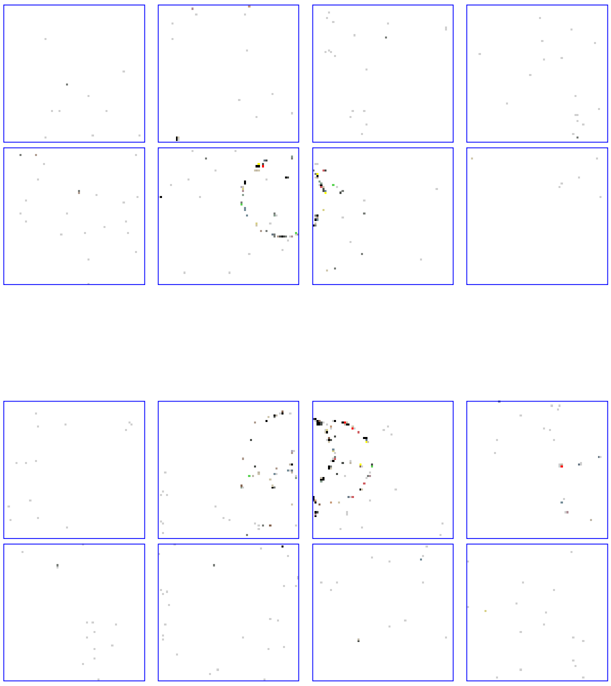

Figure 3.10: A typical RICH-event from the beam-time 2002. The individual fields are the read-out fields on the back wall of the RICH, 2 x 4 above and below the beam plane. The radius of the ring is characteristic for the type of particle which originally emitted the Čerenkov light.

3.5.2 The Hadron Calorimeters

At the back end of each spectrometer stage, a hadron calorimeter absorbs incident hadrons and measures the energy they deposit. The calorimeter consists of several layers of iron and of scintillating material, alternating in the beam direction and each covering a transverse area of 4 m x 3 m. Inelastic reactions in the iron plates cause a cascade of secondary particles that trigger light pulses in the scintillator layers which are converted by photomultipliers into electronic signals. The integral of all light signals is a measure of the energy deposited in the calorimeter.

The quick response of the scintillators in the hadron calorimeter makes it suitable as an energy trigger signal for the spectrometer as a whole. For the trigger on photon-gluon fusion events a minimum energy deposition in the calorimeters is demanded (see Section 3.6.1).

3.5.3 Muon Identification

Muons are identified unambiguously at the rear of each spectrometer stage by taking advantage of their far greater penetration in material compared to hadrons. The relevant detectors each consist of an absorber followed by the detecting element. In the large-angle spectrometer (Muon Wall 1) four layers of plastic Iarocci tubes covering an area 400 cm x 200 cm hang behind a 60 cm thick iron wall. A particle able to penetrate this wall is regarded as a scattered muon. The beam itself passes through a hole in the middle of this detector and is not detected. Muon Wall 2, at the back of the small-angle spectrometer uses the same principle, this time with steel drift tubes filled with an $Ar : CH_4$ 25%:75% gas mixture behind a 2.4 m thick concrete wall. Minimally-deflected muons which flew though the beam hole in the first Muon Wall can be detected here.

3.6 The Trigger System

In order to form an event from those pieces of information from individual detectors which belong together, an activating signal must be distributed to the read-out of all detectors. This *trigger* signal gives the command to process all data collected within a specified time-window around it. Since the ability to buffer data is restricted as a result of the high data-rates, this trigger signal must be available as quickly as possible. The bottleneck at COMPASS is the ADC read-out of the calorimeters, which are buffered solely by a 600 ns delay cable [4]. To ensure the availability of a trigger signal within this timescale, the trigger system is based on fast scintillation detectors read out by photomultipliers.

The trigger logic must also decide whether all the appropriate characteristics are present in an event to justify a trigger signal. These characteristics depend on the reaction under investigation. Naturally as few "interesting" events should be thrown away as possible; equally important, however, is that as few events as possible that do no fulfill the right physical criteria are stored, since event recorded requires disc space and represents additional expense.

At COMPASS two classes of reaction are differentiated the kinematics of which are very different but which are both of interest to the physics investigated by the experiment: photon-gluon fusion events and inclusive deep-inelastic scattering events.

3.6.1 Trigger on Photon-Gluon Fusion Events

Photon-Gluon Fusion (PGF) events are of central importance to the open charm programme for the determination of ΔG at COMPASS (see Section 2.5). Important characteristics of this class of reaction are a small momentum transfer to the exchanged photon (quasi-real domain) and a correspondingly small muon scattering angle of under 10 mrad. A high degree of polarisation, D, of the exchanged photon is also required. Since this last quantity vanishes at small fractional energy transfer y (c.f. (2.39)), a minimum value of $y = 0.2$ is required.

Muons scattered under very small angles are detected by several scintillator hodoscopes situated to the Jura side of the beam behind a muon filter made of concrete. According to their exact construction and position with respect to the beam, the trigger hodoscopes are given different names. The kinematic region covered by each of these – the outer, inner, middle and ladder hodoscopes – can be seen in Figure 3.13.

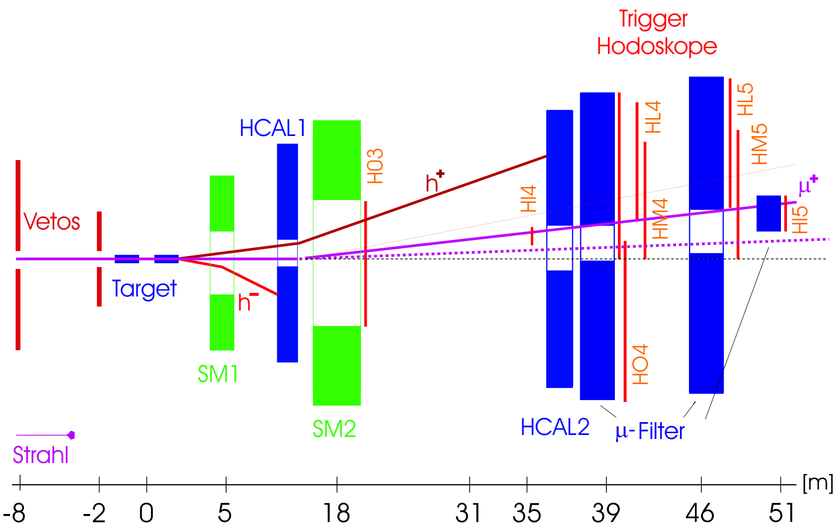

Figure 3.11: A generalised view of an event in the COMPASS spectrometer. Muons are deflected to a degree determined by their momentum by the spectrometer magnets SM1 and SM2. In the case depicted, correlated signals in the hodoscopes HI4 (station H4, inner trigger), HM4 (station H4, middle trigger) and HI5 (station H5, inner trigger) form a trigger signal.

The requirement that a scattered muon must have lost at least 20% of its energy means that the particle must be detected in two such detectors at different positions in z along the beam. The trigger hodoscopes are therefore organised in two groups, H4 and H5, with each plane in each group consisting of 32 plastic scintillator strips positioned vertically with respect to the beam direction. The two groups are approximately 40 and 50 m downstream of the target respectively (Figure 3.11) [70].

The read-out channels of these hodoscopes form a 32 x 32 matrix. Since muons of differing energy are deflected by different amounts in field of the spectrometer magnets, thereby causing signals in different channels of the the trigger hodoscopes, a diagonal can be drawn over this trigger matrix corresponding to a certain energy loss (Figure 3.12). Only when an element of the combination matrix corresponding to an energy loss of more than 20% is activated is a trigger signal produced. This suppresses background events caused by halo or beam muons that pass the spectrometer with little energy loss.

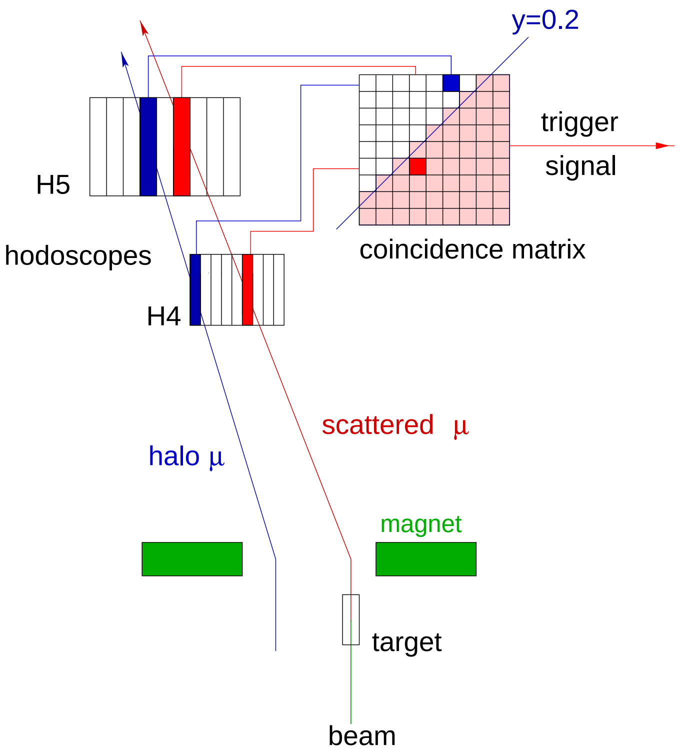

Figure 3.12: Schematic representation of the coincidence matrix in the energy-loss trigger. A muon is deflected to a different degree in x (to the left or right) according to its loss of energy in the primary scattering process. The combination of channels passed by the muon corresponds to an element in the trigger coincidence matrix. A diagonal is drawn though this matrix and only muons that exhibit a relative energy loss $y > 0.2$ initiate a trigger signal. Halo and other muons can be removed from the data sample in this way.

Because of the momentum spread of the incoming muon beam, but also as a result of other processes such as Bremsstrahlung or elastic electron-muon scattering, it is also possible that a muon that was not party to a reaction in the target has an energy more than 20% lower than the nominal value. To avoid such complications a minimum energy deposit in a hadron calorimeter is additionally required to ensure that a hadron was involved in the scattering process [4].

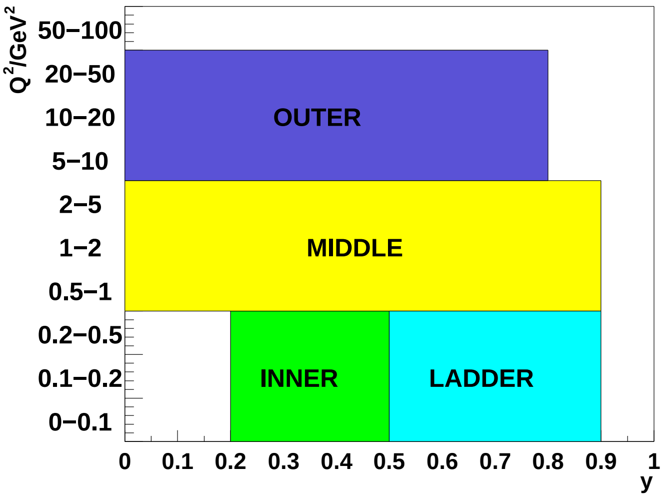

Figure 3.13: The kinematic regions in the $Q^2 - y$-plane covered by the different triggers (from [4]).

3.6.2 Trigger on Deep-Inelastic Scattering Events

In contrast to the trigger on PGF events, a large momentum transfer, $Q^2 > 0.5$ $(\mathrm{GeV}/c)^2$, is required for deep-inelastic events. A large range of y, $0 \leq y \leq 0.9$ should also be covered. Since the energy loss of the scattered muon, and therefore its deflection in the magnetic field, is of no interest, a plane resolving in the horizontal co-ordinate x is not required. The hodoscopes used here consist of horizontally mounted plastic scintillators covering a wide range to the side of the beam. Since the trigger must also detect inclusive scattering reactions – i.e. processes in which no hadron is detected – no signal may be demanded from the hadron calorimeter. In order by other means to suppress signals from halo muons that did not participate in an interaction in the target but that still possess or affect the angle of 4 mrad corresponding to the minimum acceptance of the trigger, several veto counters are to be found in the pre-target region. The active area of these counters covers only the area outside the beam. If a signal is registered in one of these counters, a halo muon is presumed to have been involved and the event is discarded. This configuration is supplemented by a veto trigger based on analogue signals taken from the two scintillating-fibre hodoscopes in front of the target. If a combination of channels is registered in these stations corresponding to a gradient in space incompatible with an interaction in the target, the event is also discarded.

3.7 The Read-Out Concept

With over 200 000 channels to be read out and a trigger rate of up to 4 kHz at full beam intensity ($2 \cdot 10^8 \mu^+$ per 5.1 s Spill), the COMPASS read-out (DAQ[4]) system must be able to cope with a data flow never before produced in a particle physics experiment [71, 72]. To get to grips with this challenge, an entirely new read-out concept was designed and realised. Instead of feeding each signal from every channel through amplifiers and discriminators onto ADC or TDC[5] modules, with the digitalisation of the signals and their merging to events occurring only at the end of the DAQ chain, COMPASS works from the principle that all signals be digitalised as soon as possible on so-called *front-end* (FE) boards mounted on the detector itself (Figure 3.14).

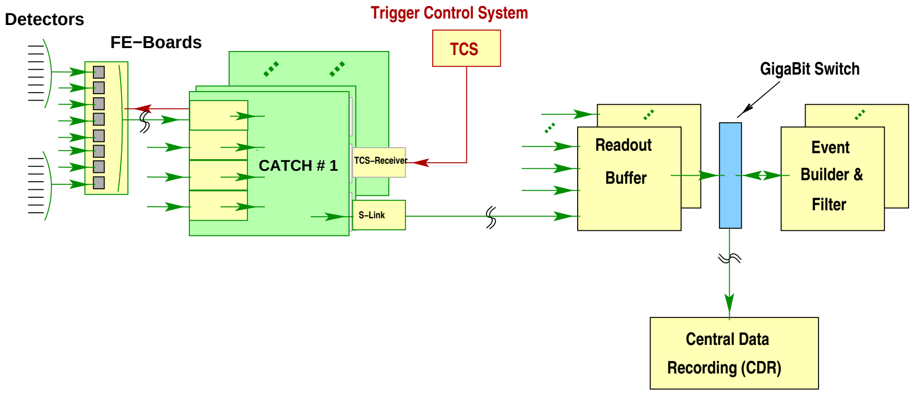

Figure 3.14: The DAQ system of the COMPASS experiment (from [73]). The data flow from the detectors via the CATCH system to the *read-out buffers* and the *event-builders*, which then finally transfer them to CERN's computing centre with the CDR system.

The core of the DAQ system, the CATCH[6] module, receives the trigger signal from the Trigger Control System (TCS) at 38.88 MHz frequency [74]. The trigger times are referenced against an experiment-wide clock also working at 38.88 MHz. If a trigger signal is available, the CATCH module "fetches" all hits stored on the front-end board that were registered within a user-specified time-window around the trigger signal. The CATCH modules are also placed as near as possible to the detectors themselves and collect data from a certain number of boards (the exact number depending on the type of detector) [75, 76]. The data-bits belonging to a trigger are combined at the CATCH to a "local" event (*sub-event building*) and piped further using the S-LINK protocol developed at CERN to the central read-out buffers (ROBs). The ROBs are commercial PCs with a Linux operating system, each containing four *spill-buffers* with 512 MB RAM. These spill-buffers are capable of storing the data from more than one spill simultaneously. This enables the DAQ to use the SPS

[4]**D**ata **A**cquisition
[5]**A**nalogue-to-**D**igital Converter, **T**ime-to-**D**igital Converter
[6]COMPASS **A**ccumulate **T**ransfer and **C**ontrol **H**ardware

down-time of 11.8 s between spills to achieve a more uniform load in the system.

The data are distributed from the ROBs to up to twelve *event-builders* working in parallel, where they are combined to global events. In the beam-time in 2002 and 2003, 100 SPS-spills were normally combined to form a *run* identified by a unique number. These runs consist of around 100 *chunks*, individual data-files of around 1 GB size which are stored on the event-builders for a short time before being finally written centrally onto tape. The ROBs and event-builders are monitored by the DATE programme developed by the ALICE collaboration at CERN [77]. Important supplementary data to each run, such as magnetic field strengths and target polarisations as well as special comments, are entered in an online log-book with a database software based on *MySQL*.

3.8 Data-Analysis at COMPASS

In each of the beam-times 2002 and 2003 between 200 and 250 TB raw data were written to tape, corresponding to a data flow in normal beam operation of some 40 - 50 MB/s [78]. The systems administering access to these data must be appropriately powerful and capable of fulfilling the requirements of many users. The first step in the handling of the data is the so-called *production*, where the raw data are used to reproduce particles and tracks. Only after this process is completed is the data of use to analysis groups interested in the different physical questions under investigation. The following sections present some details of processes and programs used in the COMPASS data-analysis.

The COMPASS Computing Farm and CASTOR

Files containing COMPASS raw data are registered by the Central Data Recording (CDR) system at the end of a run and transferred to the COMPASS Computing Farm (CCF) using the CERN-standard RFIO protocol. They are stored on hard-disc 20 servers with 500 GB capacity each were available in 2002) for a short period of several hours to several days according to system load before being written to tape. Access to data on tape is through the CASTOR[7] system, which presents the user with a directory structure and commands for the writing, reading, opening and closing of the files. When a file on tape is required, CASTOR downloads a copy onto disc provided the file in question is not already there having been requested by another user. According to the number of simultaneous requests this process takes up to several minutes. Files that are no longer being used are deleted from tape by CASTOR after a certain time. Databank functionalities in accessing the data are provided by the commercial software *Oracle*.

Files not containing data from from the spectrometer, but which are nevertheless necessary for their interpretation, such as geometry and alignment files and detector mappings (see Section 4.2.3), are stored separately on disc. Detector

[7] **C**ERN **A**dvanced **STOR**age

calibrations such as the SciFi time calibrations discussed in Section 4.4 are held ready in a *mySQL* database structure.

CORAL and the Production Process

The software used by COMPASS for the extraction of physical objects from the raw data and to a lesser extent for analysis is the internally-developed CORAL[8] suite. This is an object-oriented collection of class libraries in the C++ programming language.

The production process starts with the selection of “good” runs according to such criteria as magnetic fields, target polarisation, number of spills, correct timing information from the Beam Momentum Station etc. These data are entered into a mySQL databank in the course of a run. If a run passes this quality check, its chunks are downloaded from tape. The attendant calibration and mapping files with the help of which the raw data are *decoded* are fetched from the appropriate databank. The following steps are followed in the production procedure using CORAL:

- **Track reconstruction:** The spectrometer is divided into three regions divided by the two spectrometer magnets. Within each region straight tracks are assumed, and hit patterns are sought which correspond to such tracks. A bridging algorithm taking into account the magnetic fields between the regions, which uses a library of possible hit combinations from Monte Carlo simulations, combines tracks from the three regions iteratively according to the greatest probability. These proto-tracks are called *helices*.

- **Particle identification:** CORAL uses several algorithms for the identification of helices as beam or scattered muons or as another particle. The direction of curvature of the track in the magnetic field gives the charge of the particle; RICH data can also be included to calculate the probability that the particle is of a particular type. As far as one exists, the calorimeter cluster closest to a track is ascribed to that particle. If there are calorimeter clusters with no associated track, it can be conjectured than an uncharged particle has passed though. Particles which can be identified as beam or scattered muons are specially flagged as such in the output.

- **Vertex reconstruction:** Tracks beginning or ending very near to a common point suggest the existence of a vertex (interaction point). Geometric and kinematic variables of the individual tracks are combined to achieve a global χ^2-Fit, which acts as a measure of the probability of a particular vertex. The fit parameters, vertex co-ordinates and associated tracks are linked in the data output.

[8] **CO**MPASS **R**econstruction and **A**na**L**ysis

The CORAL output (a collection of physical objects such as tracks, particles and vertices) is stored in mDST[9] format. The format is that of an *ntuple* legible by ROOT [79]. In comparison with the raw data size of around 1 GB per run, the mDSTs contain only around 60-70 MB, i.e. 6-7% of the original quantity. Standard histograms and log-files can also be created in the production, with the help of which the stability of the data and the spectrometer can be monitored.

PHAST

The main tool for physics data-analysis at COMPASS is the internally-developed program PHAST[10]. The program reads in all objects from the mDSTs and uses ROOT routines for the production of histograms etc. The user can also select the events of interest to a particular analysis and write them out as a ROOT tree that may then in an iterative process be read in by PHAST again. This allows each user to tailor the data individually. The analysis of the COMPASS transversity data discussed in Chapter 5 was performed with PHAST.

[9]**m**ini **D**ata **ST**orage

[10]**PH**ysics **A**nalysis **S**oftware and **T**ools

Chapter 4

SciFi Hodoscopes at COMPASS

The eight hodoscope stations with scintillating fibres[1] are an integral part of the detector system for track reconstruction in the beam-region at COMPASS. Their high-rate capability, excellent time-resolution and good spatial resolution make them highly suited to this task. Of the eight SciFi stations at COMPASS, four in the region immediately around the target (FI01-FI04) were constructed by a group from the of University of Nagoya in Japan, and four (FI05-08) were developed and built by the groups of Prof. J. Bisplinghoff at the Helmholtz Institute for Nuclear and Radiation Physics (ISKP) at the University of Bonn and of Prof. W. Eyrich at the Physics Institute of the University of Erlangen-Nuremberg. In the following sections the construction principles of these last four stations is sketched. Program routines for the monitoring of the SciFis during running time, and for their calibration and the calculation of their efficiency using data from the beam-times 2002 and 2003, will also be presented.

4.1 SciFis in the COMPASS Spectrometer

Of the total of eight SciFi stations in the COMPASS spectrometer, the first two (FI01 and FI02) are positioned in front of the target and deliver precise timing information from the incoming beam. Stations FI03 and FI04 cover the spectrometer section immediately behind the target. Further back, but still in the large-angle spectrometer between the two spectrometer magnets SM1 and SM2, are the stations FI05, which is mounted on the front wall of the RICH detector, and FI06. The configuration is completed with two further stations FI07 and FI08 behind SM2 in the small-angle spectrometer. The task of these last two stations is to detect scattered positive muons deflected by the magnetic field of SM2 to the Jura side (left in the direction of the beam). These hodoscopes are therefore displaced from the central axis in x – in the case of FI08, because of its position some 10 m downstream of SM2, by some 7 cm. Thus the undeflected beam is only seen on the very edge of the active area of

[1] In the following sections the abbreviation “SciFis” or the official COMPASS abbreviation *FI* will be used for the scintillating-fibre hodoscopes.

Station -planes	z-position	Ø total	Ø active	pitch [2]	fibres per channel	active area (side)	channels (X/Y)	channels (U/V)
	$[m]$	$[mm]$	$[mm]$	$[mm]$		$[mm]$		
FI01-XY	-8.0	0.50	0.44	0.41	7	39.4	96	-
FI02-XY	-3.0	0.50	0.44	0.41	7	39.4	96	-
FI03-XYU	1.0	0.50	0.44	0.41	7	52.5	128	128
FI04-XYU	2.2	0.50	0.44	0.41	7	52.5	128	128
FI05-XY	5.9	0.75	0.66	0.525	6	84	160	-
FI06-XYV	15.0	1.00	0.88	0.70	4	100	143	176
FI07-XY	21.3	1.00	0.88	0.70	4	100	143	-
FI08-XY	31.0	1.00	0.88	0.70	4	123	176	-

Table 4.1: Overview of the scintillating-fibre hodoscopes in the COMPASS spectrometer. The origin of the z co-ordinate is in the middle of the second target cell. The total diameter includes the *cladding* of the fibre (see Section 4.2.1). The active area of the station is a square with the given side.

the projection FI08X.

All COMPASS SciFi stations are equipped with planes (projections) that resolve in the x and y co-ordinates. Stations FI03, FI04 and FI06 are also furnished with a diagonal layer ("u" or "v") supplying a further point in space to reduce combinatorial ambiguities in the track reconstruction. The number of detector planes is therefore in total 19, of which nine were constructed in Bonn/Erlangen. The active area of the stations increases the further back the detector is the spectometer to take into account the increasing dispersion of the beam beyond its focal point in the target, an effect caused among other things by scattering on the material of the spectrometer itself. Similarly, the diameter of the fibres employed also grows the further away from the target the detector is; this is to ensure as uniform a rate-exposure for the individual channels as possible. An overview of the most important data concerning the SciFis is to be seen in Table 4.1.

4.2 The Detector Concept

The demands made on detectors in the beam region represent, because of the very high rates involved, a technical challenge. Specifically, the SciFis must:

- withstand a rate of $2 \cdot 10^8 \mu$ per SPS spill (5.1s plus 11.7s down-time) – i.e., a radiation dose over an estimated 100 days beam-time per year of around 31 kGy – without significant deterioration of response;
- exhibit a time-resolution of the order of 1 ns or less, in order to be able to separate correlated hits from combinatorial background with on average one beam-particle arriving every 25 ns;
- possess a spatial resolution of the order of 1mm;

[2] by *pitch* the distance between the midpoints of two neighbouring fibres is understood.

- exhibit a high detection efficiency in all stations to ensure a high track reconstruction efficiency in the whole spectrometer;

- since they are positioned in the beam, possess as little material as possible in order to reduce the number of secondary reactions.

Only with the development in the past decade of multi-anode photomultipliers and optimised scintillator materials in the form of fibres has it become possible to fulfil the requirements listed above. The complementary components used by the hodoscopes developed in Bonn and Erlangen, as well as distinctive features of their construction, will be elucidated in the following sections.

4.2.1 Properties and Geometry of the Scintillating Fibres

A scintillating material is characterised by atoms which become excited at the passage of an ionising particle, and then de-excite emitting light in the ultraviolet range [80]. In a scintillating fibre this happens in the so-called *core* of plastic surrounded by at least one outer layer, the *cladding*, of a plastic with a different refractive index. Thus a fraction of the light produced in the scintillator is trapped by total internal refection and transmitted as in an optical fibre (Figure 4.1). In the fibres made by the firm Kuraray used at COMPASS the core is made of Polystyrol. The cladding, which in this case consists of two layers, consists of Polymethylmethacrylat (PMMA) [81]. Since the absorption region of the core is also in the UV range, this is doped with a wavelength-adjuster that absorbs the scintillation light and re-emits it in the visible spectrum, thus avoiding auto-absorption. This also allows advantage to be taken of the fact that the efficiency of most photomultipliers reaches a maximum in the visible.

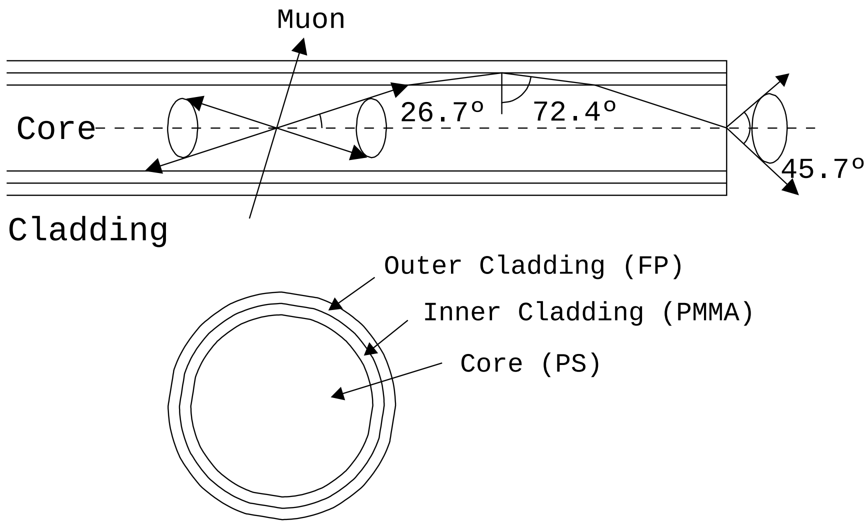

Figure 4.1: Longitudinal and cross-section views of the Kuraray SCSF-78MJ fibre used in the COMPASS SciFis.

The number of photo-electrons excited at the photomultiplier cathode, N_{PE}, is directly proportional to the number of photons produced in the scintillator in a minimally-ionising event [82]. In order to achieve the time-resolution σ_t of under 1 ns required by COMPASS, a large number of photons is required, since

$$\sigma_t \sim \frac{1}{\sqrt{N_{PE}}}. \tag{4.1}$$

The use of scintillating fibres of a larger diameter would however affect the spatial resolution, σ_x, which is given by

$$\sigma_x = \frac{x_p}{\sqrt{12}} \tag{4.2}$$

where x_p is the fibre pitch (the geometrical distance between the mid-points of two neighbouring channels). In order to avoid such a deterioration, the light output is increased by arranging several fibres belonging to one channel behind one another [83]. In the first four stations FI01-04, seven fibres are used per channel; for station FI05, six; and for the hindmost three stations FI06-08, four fibres. An arbitrarily large number of fibres cannot be used since the material in the beam region must be kept to a minimum: a compromise must be found between low material density and good time-resolution.

The diameter of the fibres used increases the further back the SciFi station is in the spectrometer; this reflects the importance of a more exact determination of spatial points in the target area, where many interaction vertices and large number of closely-spaced tracks are to be expected, as well as the need to reduce the rate on any individual channel. The spatial resolution of the SciFis built in Bonn/Erlangen is further improved by placing the fibre columns of neighbouring channels not directly next to each other, but displaced slightly, so that a "honeycomb" structure is formed (Figures 4.2, 4.3). This reduces the effective pitch between two channels and thus improves (c.f. (4.2)) the spatial resolution of the detector.

The requirement that there be as little material as possible in the beam region, along with the in some cases large fringe-fields of the spectrometer magnets means that the photomultipliers and their attendant electronics must be located to the side of the spectrometer away from the beam-axis [85]. For the stations at the rear of the spectrometer, this distance is somewhat more than 1 m, and must be bridged with optical fibres. This represents a better solution than scintillating fibres throughout, since the light-loss over the same distance in a scintillator is of the order of a factor three greater due to auto-absorption effects [86].

The point of contact of scintillating and optical fibre must be established through the welding of the two, investigations having shown that conventional glues became cloudy and the optical properties at the junction compromised when exposed to high rates of radiation for a longer period [87]. In adjacent

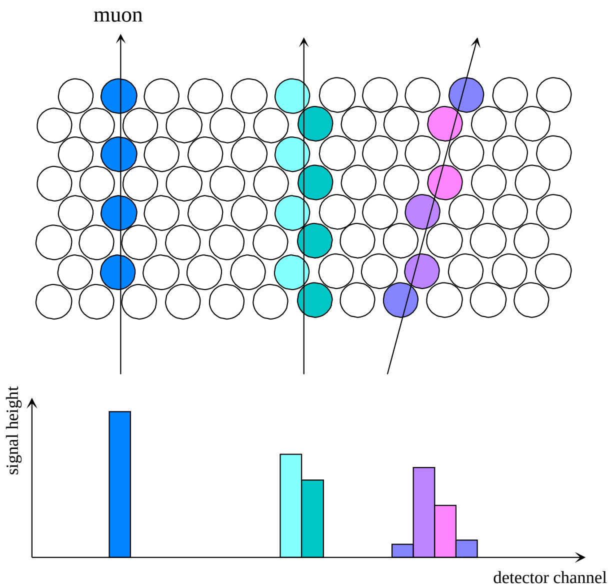

Figure 4.2: **(above)** Cross-section through a SciFi detector layer. A detector channel comprises several fibres arranged one after the other in order to increase the light output from a particle in transit. **(below)** Response of the individual detector channels in the different scenarios in the upper picture [from [84]].

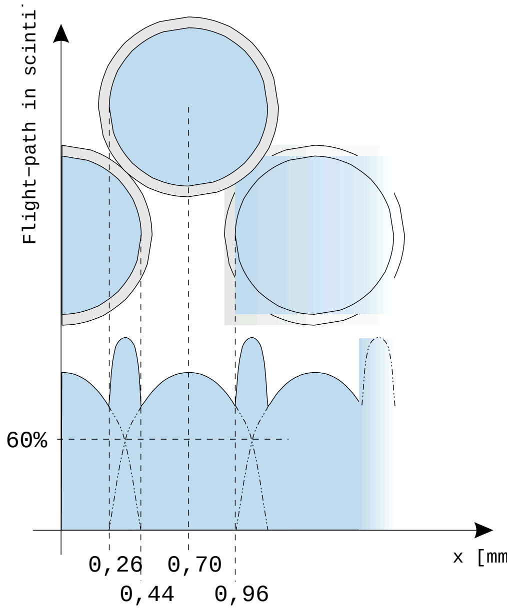

Figure 4.3: Overlap between neighbouring fibres (example of fibre hodoscopes FI06-08 with fibre diameter of 1.0 mm). Every particle traverses at least 60% of the maximum path in the scintillator [from [84]].

channels this welding point is shifted by a few millimetres so that no mechanically weak point is created [84].

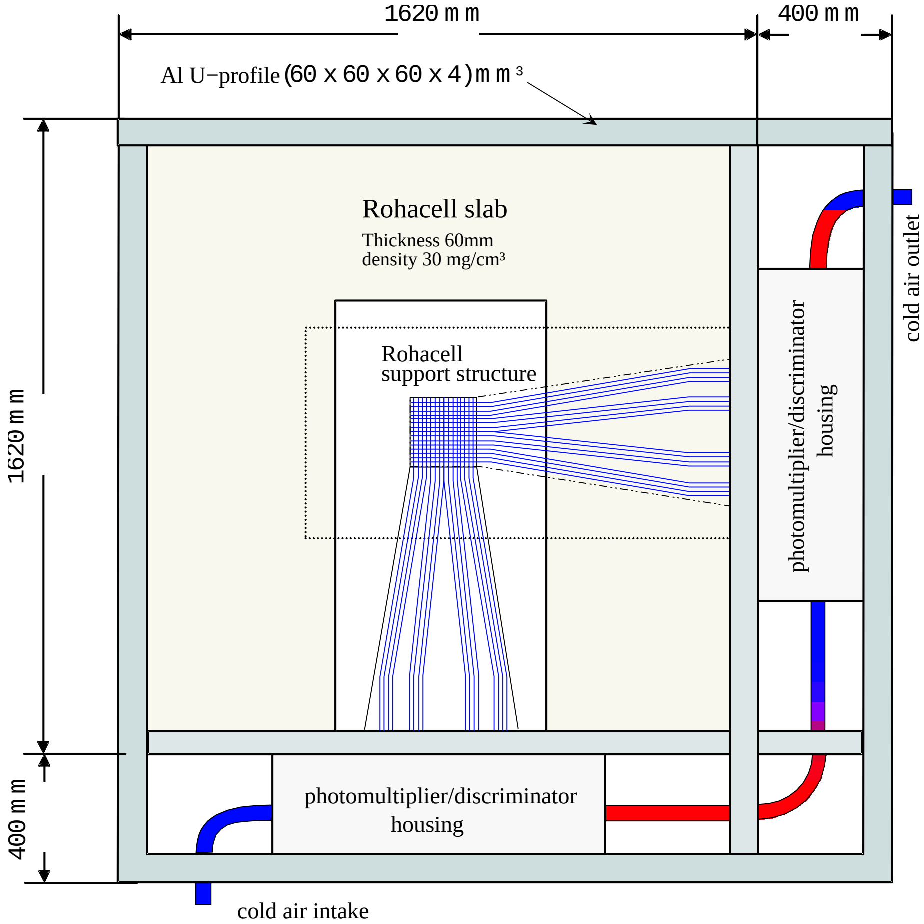

Figure 4.4: Schematic representation of the support-structure for a fibre hodoscope together with its photomultipliers, discriminator and cooling in the COMPASS beam-line at CERN.

4.2.2 The Hamamatsu H6568 Photomultiplier

16-channel photomultipliers of the model H6568 from the Japanese firm Hamamatsu [88] are employed in the fibre hodoscopes developed in Bonn/Erlangen. These photomultipliers are characterised compared to their predecessors by their good noise and crosstalk characteristics, as well as a relatively uniform amplification over all channels [89].

The 16 channels of the H6568 photomultiplier are arranged in a 4 x 4 matrix (Figure 4.5). Each photocathode possesses an active area of 4 mm x 4 mm with spacing of 0.5 mm between neighbouring cathodes. Their spectral sensitivity lies in the range 300 nm to 650 nm, with a maximal quantum efficiency[3] of 20%

[3] ≈ the probability that an incident photon ejects an electron

at around 420 nm. Each photomultiplier channel consists of an independent twelve-stage dynode chain with which an amplification of up to $5 \cdot 10^7$ can be achieved.

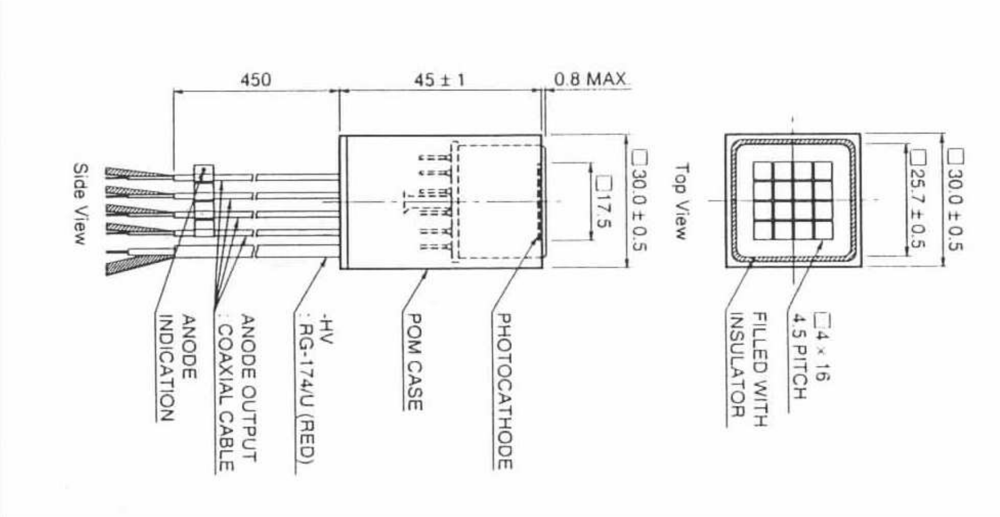

Figure 4.5: The 16-channel photomultiplier H6568 with its 4 x 4 cathode arrangement.

The high amplification led initially to the supply voltage to the last few dynode stages breaking down as a result of the high electron current on the dynodes themselves. Following extensive investigation, this problem was overcome in cooperation with Hamamatsu by supplying the last three dynodes with an additional independent voltage supply (the so-called *booster base*) [86, 84].

4.2.3 Read-Out of the SciFi Stations

The read-out concept of the COMPASS experiment envisages that all signals be digitalised as close as possible to their origin and transferred on as hit and/or time information (see Section 3.7). The discriminator cards of the SciFi detectors are to be found in boxes hanging on the side of each station. The maximum cable length from photomultiplier output to the discriminator board is around 40 cm. The digitalised hit information is buffered on the discriminator board until a trigger signal is received by the CATCH module (see Section 3.7). If no signal comes, the information is discarded. Two distinctive features of the Bonn/Erlangen SciFi read-out should be discussed at this point: double-threshold discrimination and double-precision read-out mode.

Double-Threshold Discrimination

The channels of the Bonn/Erlangen SciFis have in general two discriminator thresholds, *high* and *low*. The only exception in the beam-time in 2002 and 2003 was the diagonal plane FI06V. The peak-sensing discriminator boards used were chosen on account of their better time-resolution and double-pulse resolution[4] of 450 ps and 15 ns respectively. The peak-sensing mode, which ascribes in the case of coincident signals on neighbouring channels the event to the channel with the higher amplitude, was not however used, since it was desirable to discard no hit information at this stage [84].

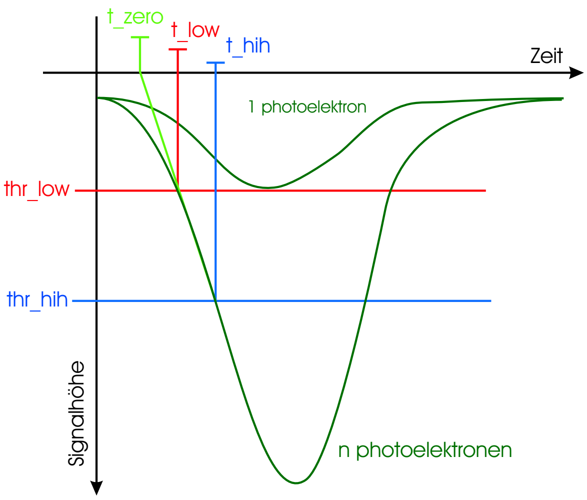

Figure 4.6: Double-threshold discrimination. Using two thresholds at different pre-determined fractions of the signal height makes an improvement of the accuracy of the timing information through time-zero extrapolation possible [from [84]].

Two advantages are expected from the two-threshold method:

1. Since an ADC read-out had to be foregone on grounds of cost, the double-threshold readout may be used to monitor the amplitude of the analogue signals. A collapse in signal height can be noticed through a widening of the time-gap between the two thresholds. Through shifts in the recorded $t_{high} - t_{low}$ spectrum, the amplitude can be determined to an accuracy of around 5% [87], more than sufficient for online monitoring.

2. An additional possibility is to use the double-threshold read-out to improve the time-resolution in particular categories of event using the time-zero extrapolation method (Figure 4.6). For exhaustive studies of this effect see [84, 90].

The individual thresholds for each detector channel were laid down at the beginning of the beam-time in 2003 [5]. In special runs before physics data-taking began, the low thresholds were increased in 20 mV steps starting at 20 mV,

[4]= the minimum time between two incoming analogue signals for the discriminator to produce two separate outgoing logic signals

[5]Should the signal height alter dramatically, an adjustment of the threshold is in principle possible at any time. During running however changes in the apparatus should be avoided as far as possible so as not to influence the sensitive asymmetries being measured.

while the high thresholds were reduced in 20 mV steps from 240 mV. The counting rates for each channel for each threshold were extracted and plotted. The resulting curves should exhibit in the ideal case a plateau at middling threshold between the region of electrical noise and the signal amplitude where the counting rate remains almost constant. A line can be drawn from the first point of deflection of the curve to the point where the rate falls to 10% of the starting level, a point assumed to be a measure of the signal height. This fit allowed the appropriate thresholds to be determined, set for each channel at 20% and 37% of the calculated signal height (t_{low} and t_{high} respectively).

Double Precision Read-Out and CATCH Assignment

In normal operating mode, up to eight hits may be stored per channel while waiting for the trigger signal. *Double precision* mode allows this number to be increased to 16. This is connected with an improvement of the time-resolution in the TDC from around 130 ps to 65 ps per bin. In order for the CATCH to be able to cope with the flow of data, each incoming channel is split onto two neighbouring CATCH inputs.

The association between the electronic channel in which the hit information is dealt with by the CATCH and the real physical detector channel that was activated is made by a so-called *mapping*. These mappings are centrally-stored files in XML-format used in the data-analysis to re-establish the topographical distribution of hits in the detector planes. For the Bonn/Erlangen SciFis it is important to note that as a result of double-precision and double-threshold one detector channel as a rule takes up four electronic channels. The mapping lines representing the first eight channels of 6X, for example, read as follows:

```
<!-- 6X: DThr, DP -->

<!--Low threshold:-->
    FI06X1__  160    4  0x114   0  4      8      0     7  1  -1
    FI06X1__  160    4  0x114   1  4      8      0     7  1  -1

<!--High threshold:-->
    FI06X1__  160    4  0x114   2  4      8      0     7  1   1
    FI06X1__  160    4  0x114   3  4      8      0     7  1   1
```

Table 4.2 explains the meaning of the individual columns of the mapping.

4.3 Online Monitoring of the Hodoscopes

4.3.1 Monitoring of Online Spectra with *COOOL*

The real-time monitoring of all detector stations at COMPASS is performed with the internal ROOT-based [79] *COOOL* software. This program takes a proportion of all events as a statistical sample. Within the structure of COOOL

Column	e.g.	meaning
1	FI06X1__	official name of the detector plane
2	160	CATCH ID no.
3	4	CATCH port no. (0,4,8 oder 12)
4	0x114	"geographical" ID of CATCH
5	0	first port input represented by this line
6	4	incrementing step of inputs represented
7	8	no. of inputs represented
8	0	ID of the first detector channel represented
9	7	ID of the last " " "
10	1	incrementing step of channels
11	-1	channel-specific information, here -1 = low threshold

Table 4.2: Composition of a COMPASS XML mapping file, using the first line of the excerpt in the text as an example. This line reads therefore: "CATCH 160, port 4: input 0 and then every 4th further input, 8 altogether, correspond to detector channel FI06X1__ 0 to 7, low threshold".

it is the job of each detector group to decide which quantities and spectra should be monitored. For the Bonn/Erlangen SciFis these are:

1. the beam profiles of each plane, separately for the low and high thresholds of each channel (e.g. Figure 4.7);

2. timing information from high and low channels;

3. the multiplicity of the recorded events;

4. for the monitoring of amplitudes (see Section 4.2.3), the spectrum of the time-differences $t_{high} - t_{low}$;

5. the *stat* variable indicating how many signals exceeded only the low threshold ($stat = +1$), how many both high and low ($stat = 0$) and how many high only ($stat = +1$). The fact that signals can cross the high threshold and seemingly not the low threshold is due to the high occupancy in the low channels, so that some hits are not registered there. This is true in almost 2% of all cases (Figure 4.8). High and low timing information are brought into connection with one another by looking for "high" times which satisfy the condition (in TDC channels) $t_{low} - 25 \leq t_{high} \leq t_{low}+50$. In double-precision mode this is equivalent to a condition $t_{low} - 1.6$ ns $\leq t_{high} \leq t_{low} + 3.2$ ns.

It is also possible to use the COOOL software to write out the raw data for further analysis in the form of a *ROOT-tree*, a kind of ntuple. For each event the channels of the hits, the timing (high or low times) and the *stat* variable are stored. A ROOT-tree can also be created from any raw-data file on tape. The data for the detector-specific calibrations and studies presented in the following sections were produced in this way.

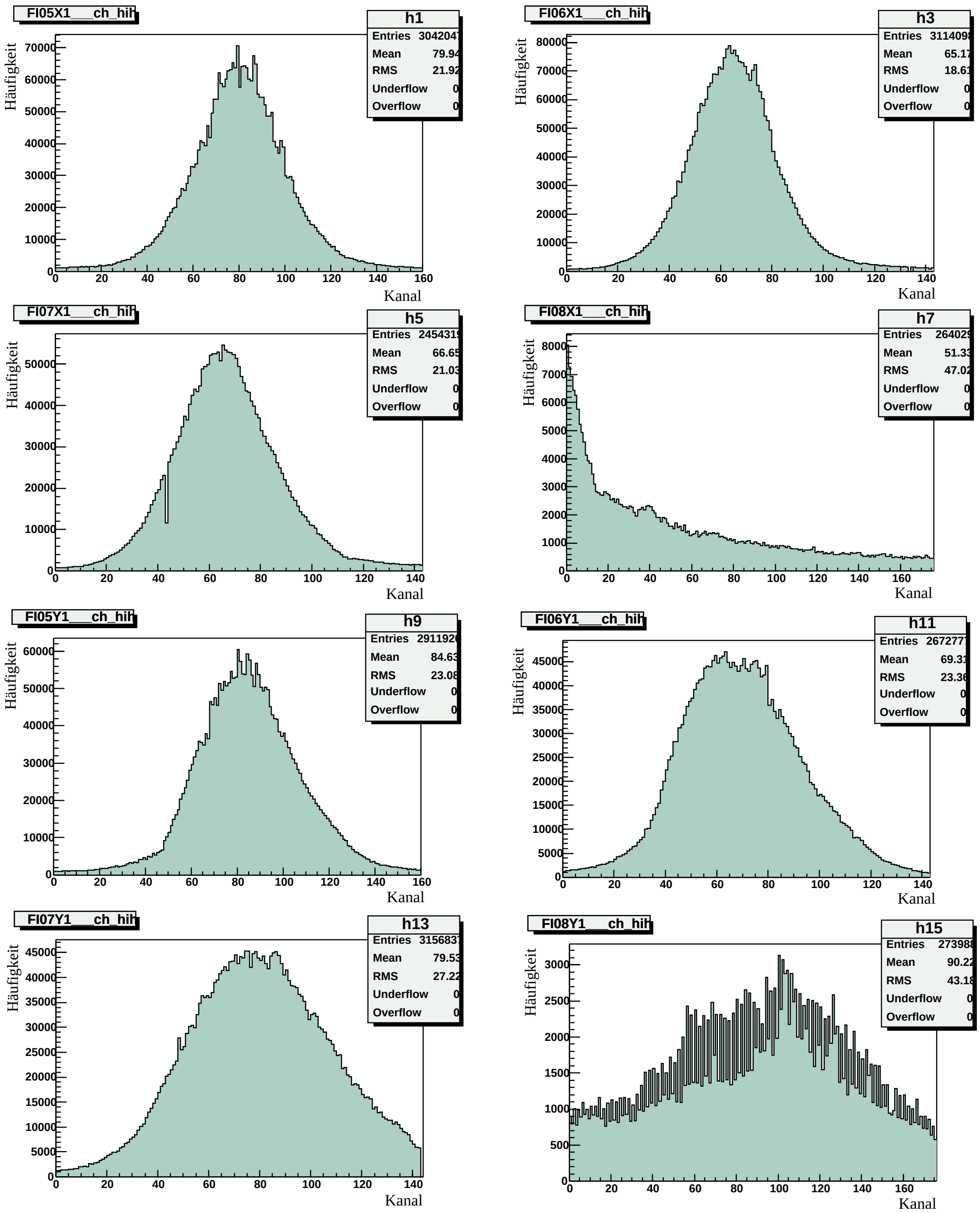

Figure 4.7: Beam profiles of the SciFi stations FI05-08, X (top four) and Y (bottom four) recorded by the COOOL program after threshold optimisation. The active area of station FI08 is situated on the edge of the beam in order to detect scattered muons in the rear spectrometer region, as can be seen in the spectrum of FI08X. This also explains the staggering effect in the plane FI08Y - the beam only touches the edge of the active area, revealing the shift of the welded joint between scintillator and optical fibre in every second channel (see Section 4.2.1).

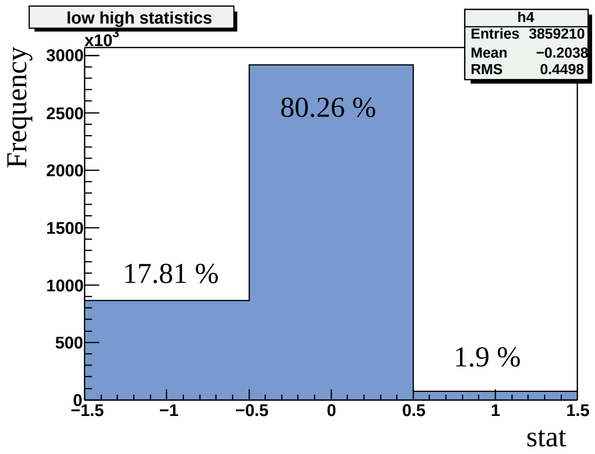

Figure 4.8: Frequency distribution of *stat* variable. In approximately 2% of all cases only a "high" time is recorded due to high occupancy in the buffers of the low channel.

4.3.2 Monitoring of High-Voltage Supply and Temperature with the DCS System

A further possibility of monitoring and remotely controlling the SciFi hardware is offered by the *Detector Control System*, DCS. This computer is capable of controlling the high and booster supply-voltages of the individual photomultipliers. A series of acoustic and visual alarms warns of excess voltage, low current and high temperature around the discriminator cards.

4.4 t0-Calibration

4.4.1 Philosophy

In order to take account varying delays in the individual scintillating fibres, as well as in the photomultipliers, cables and electronics of each detector channel, it is necessary at regular intervals to perform a *t0*-calibration. The aim of this calibration is to ascertain the average time by which the hits in a channel differ from the predetermined trigger time (which is for an event the same in all detector channels). Once these constants are subtracted from the time-spectrum of each channel, a distribution around zero remains. This compensates for systematic differences specific to each channel and leaves a purely statistical distribution of the delays to each signal which is in the main a function of the point in the fibre at which the particle passed through and of the finite time-resolution of the detector. Only those hits recorded within a certain time-window around the middle of the distribution (*trigger-correlated* events) are used in the analysis, since they are likely to correspond to a physical event. The principle of the calibration process is shown in Figure 4.9.

The systematic differences in channel delays for which a t0-calibration is intended to compensate should remain constant throughout the beam-time, pro-

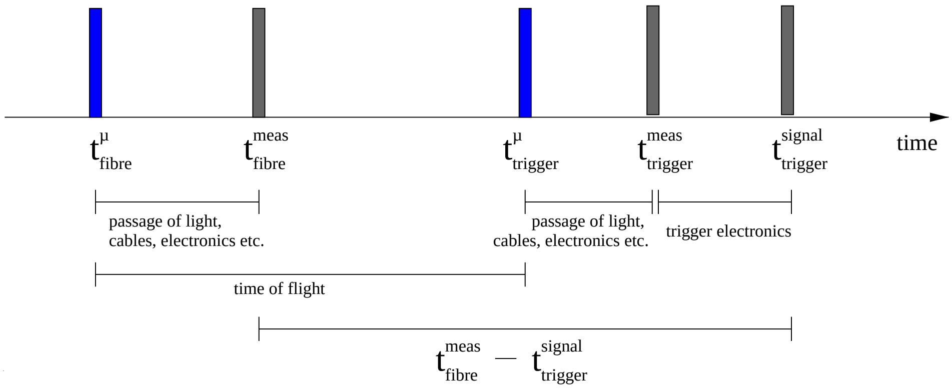

Figure 4.9: If a muon flies with almost light-speed through the spectrometer, the time-of-flight between SciFi and Trigger signals t^{μ}_{fibre} - $t^{\mu}_{trigger}$ can be assumed to be constant. The processing time of the trigger $t^{\mu}_{trigger} - t^{signal}_{trigger}$ is also constant. The measured time-difference $t^{meas}_{fibre} - t^{signal}_{trigger}$ should be a δ function; because of varying delays in the individual SciFi channels a normal distribution is formed. The calibration process ascertains the average time-difference.

vided the hardware does not change. In spite of this it is advisable to perform new calibrations regularly, since for example temperature changes over the course of a run can affect the effective cable-lengths. In the summer of 2003 it was discovered that the calibration constants of the BMS exhibited a day-night effect, mainly as a result of the coaxial cables of some 40 m length that led the signals through the beam-tunnel. Although such drastic effects are not to be expected in the SciFis with the much shorter distances involved, a new calibration was performed at least once a week. Where hardware was changed (for example the swapping of a CATCH module as occurs several times during a beam-time) a re-calibration was also performed. In 2002 the calibrations were made retrospectively at the end of the beam-time using several runs. Twelve calibrations were performed in total, equivalent to approximately one per week of physics data-taking. During the beam-time in 2003, the calibration process occurred largely parallel to the data-taking. 20 calibrations were made in all, more frequently in the first weeks where some hardware improvements were still being completed. All scintillating-fibre hodoscopes, those built in Bonn/Erlangen and the Japanese-built stations, were calibrated concurrently.

4.4.2 The Calibration Algorithm

At regular intervals during the beam-time 2003, on average every two to four days, data-files from one run, preferably from several event-builders, were decoded using COOOL and ROOT-trees written. These single trees were then combined to a larger tree. In order to obtain the statistics necessary for a reliable calibration, at least 250 000 events were required. This ensured that even those channels in plane FI08X standing outside the beam (with a consequently low rate) contained an adequate number of hits abd required the decoding and merging of on average ten data-chunks of around 1 GB size.

For the calibration itself, C++-based scripts for the ROOT environment were written which automatised the process to a large extent. For each SciFi channel the spectrum of trigger-related timings was produced for both thresholds. A normal distribution riding on a constant background was fitted to the trigger-correlated peak of each channel; in order to calculate the background, the average of all entries over 100 TDC channels each side of the peak was taken. The mean value of each fit produced in this way was taken as the calibration constant. This was then subtracted from all times at that threshold in this channel to produce a time-spectrum centred around zero (Figure 4.10).

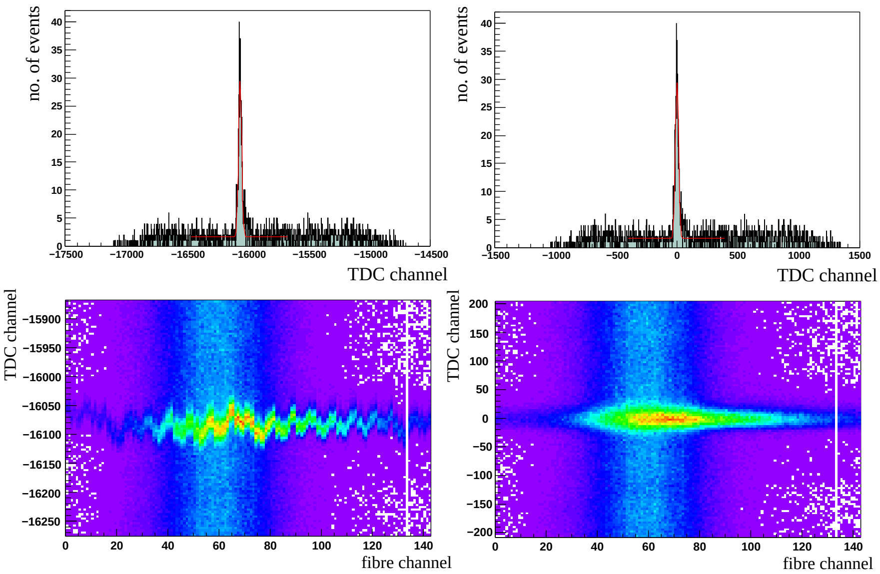

Figure 4.10: Before **(left)** and after **(right)** time-calibration of the SciFi plane FI06X. The process compensates for differing delays between channels.

4.4.3 Flagging of "Bad" Detector Channels

It is important that in addition to the constant itself, information is supplied as to the status of a channel as the time of calibration, in order to assess whether the data from the channel are usable. The official COMPASS format uses an additional flag for each channel, usually set to 0, for this purpose. Other flag-settings are:

- **flag = 2** indicates a bad fit, with σ less than 4 or greater than 20 TDC channels ($\sigma \approx 10$ is expected);
- **flag = 3** indicates a noisy channel that can however be calibrated. The condition is a number of entries fewer than 200 times as big as the background per histogram bin, together with a peak with fewer than three times as many entries as the background;

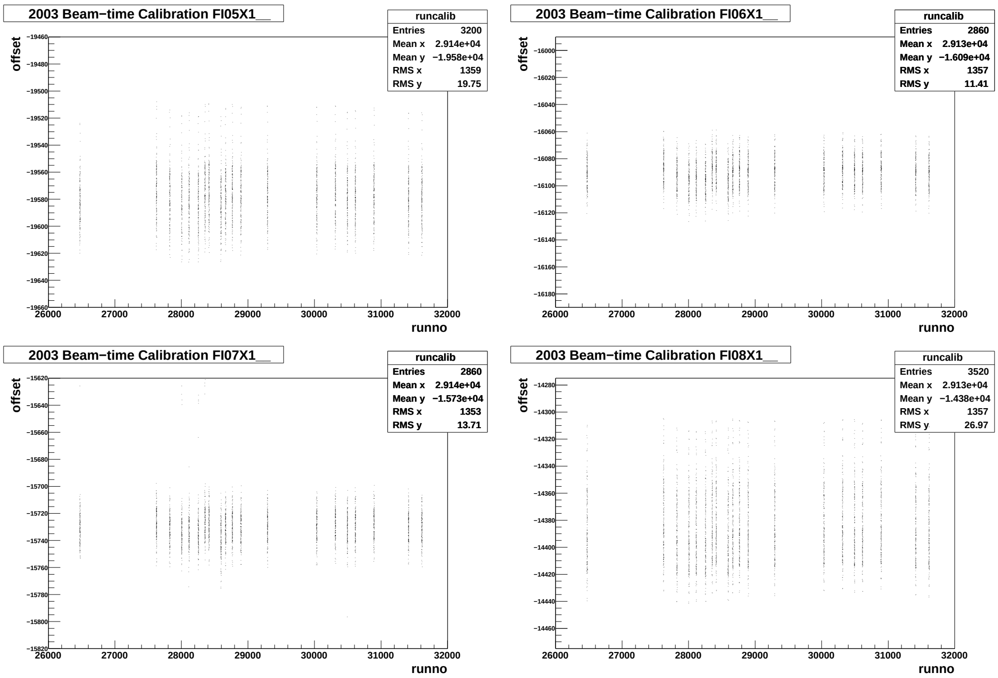

Figure 4.11: Stability of the calibration data during the beam-time 2003. All calibration constants for four detector planes (5X, 6X, 7X, 8X) for all runs for which a calibration was performed. The degree of scattering of the constants in any one plane is stable, as are the individual constants.

- **flag = 5** indicates a dead channel with fewer than 200 entries in the whole time-spectrum;

- **flag = 8** indicates other reasons to be careful using a particular channel that do necessarily require the channel to be disregarded, such as a double peak.

The calibration script indicates automatically which channels have been flagged; these are then examined individually with the naked eye to ascertain whether there is indeed a problem. Data from channels with $flag = 2$ and $flag = 5$ are automatically disregarded in the data-production process, whereas channels with $flag = 3$ and $flag = 8$ are generally still used. These last two flags function merely as warnings.

The flagging-statistics provide a simple picture of the reliability of the SciFi stations during beam-time. The total number of hours during which a single channel or block of channels is flagged with 2 or 5 is calculated and compared to the total number of "channel-hours" in the data-taking period. In the beam-time in 2003, the number of channels affected was in general lower than in 2002; in the second half of the 2003 beam-time the reliability was virtually 100

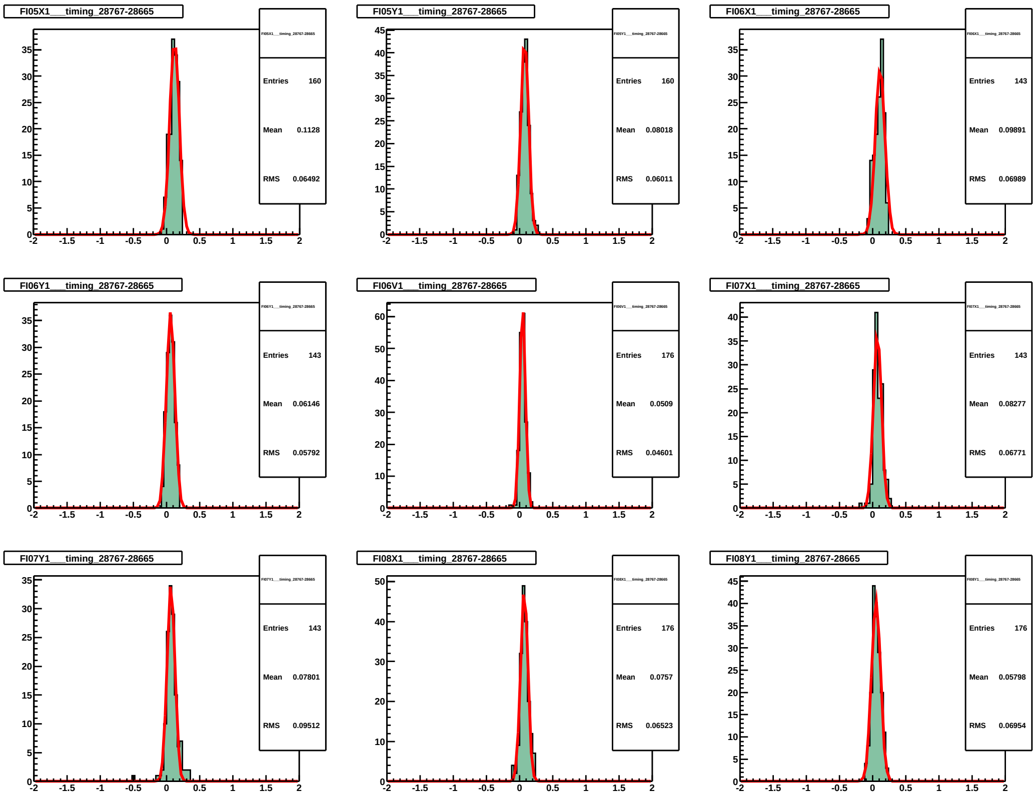

Figure 4.12: Variation in calibration constants between two runs (28665,28767) approximately two days apart. The average variation for a single channel over this period is between 50 and 100 ps – around 1 - 1.5 TDC channels in double-precision mode.

%. Only one channel at the extreme edge (FI07Y No. 0) was found to be definitively dead.

4.4.4 Calibration Stability

A picture of the stability of the time-calibrations – i.e., to what extent the calibration constants change over a longer period – could be made in the course of the 2003 beam-time. It was established that there were no significant long-term variations. The distribution of the differences in calibration constants between two calibration runs shows that the drift for single channels is below 100 ps. A relative sparse calibration density is therefore sufficient to ensure the delivery of reliable timing information from the SciFis. Figures 4.11 and 4.12 demonstrate this point.

4.5 Efficiency Calculations

The principle of all algorithms to determine the efficiency of a detector is the comparison of the number of hits in the detector plane under investigation with

Beam-time	total channel-hours ($\times 10^6$)	*of which malfunctioning*	reliability %
2002[6]	1.78	13507	99.2
2003	3.10	9148	99.7
2003 (ab 08.08)	1.33	936	≈ 100

Table 4.3: The reliability of the Bonn/Erlangen SciFis during the beam-times in 2002 and 2003 (sum of the down-time of all channels.

a reference number of hits in other planes. Hits which are highly correlated in time with the reference hits are sought. In the case of the SciFis, with their high hit frequency, which can lead to several combinatorial possibilities even in a narrow time-window, it is also desirable that there be a geometrical correlation between the reference hits and the hits in the plane being examined. Because of the positioning of the SciFis in the beam-region, the efficiency calculation can only be conducted among the SciFi planes themselves.

4.5.1 Tracking Efficiency

One possibility of calculating the efficiency of individual detector planes for those runs produced for the physics analysis is to examine hits along the reconstructed particle tracks. If a hit is found in each of the detector planes acting as references, a hit should also be present in the plane under investigation. The efficiency ϵ of a plane h_0 is given by

$$\epsilon = \frac{N(h_0 \&\& h_i)}{N(h_i)} \tag{4.3}$$

where $N(h_i)$ is the number of events where a hit has been recorded in all reference planes, and $N(h_0 \&\& h_i)$ is the number of events where all reference planes and additionally the plane under investigation have recorded a hit. Typical global efficiencies for the individual planes and the planes used as references are listed in Table 4.4. Since the calculation is based on physical tracks, in the cases of stations FI01 and FI02 only the other planes of the two stations can be used as references; these stations are in front of the target, and tracks belonging to beam particles end at the target. The slightly reduced efficiency of the Japanese SciFi stations FI01-04 in the target-region is largely a result of the small overlap between neighbouring channels in these planes (c.f Table 4.5), and also of the peak-sensing discrimination used. Figures 4.13 and 4.15 show the efficiency of SciFi plane 6X in the course of data-taking in transverse target mode in 2002 (three periods - *P2B*, *P2C* and *P2H* - each of approximately one week). The efficiency of all stations remains stable throughout all the periods, in this case at around 99%.

[6] Approximately the first third of the 2002 beam-time is not included in these statistics, as the appropriate data were not collected.

Plane	references	efficiency %	no. events
FI01X	1Y,2X,2Y	95.7	$4.6 \cdot 10^7$
FI01Y	1X,2X,2Y	92.2	$4.8 \cdot 10^7$
FI02X	2Y,1X,1Y	95.0	$4.7 \cdot 10^7$
FI02Y	2X,1X,1Y	95.1	$4.7 \cdot 10^7$
FI03X	3Y,3U,4X,4Y,4U	91.8	$5.0 \cdot 10^7$
FI03Y	3U,3X,4X,4Y,4U	92.2	$5.0 \cdot 10^7$
FI03U	3X,3Y,4X,4Y,4U	91.9	$5.0 \cdot 10^7$
FI04X	4Y,4U,3X,3Y,3U,5X,5Y	94.0	$3.8 \cdot 10^7$
FI04Y	4U,4X,3X,3Y,3U,5X,5Y	93.9	$3.8 \cdot 10^7$
FI04U	4X,4Y,3X,3Y,3U,5X,5Y	91.4	$3.9 \cdot 10^7$
FI05X	5Y,4X,4Y,4U,6X,6Y,6V	97.8	$2.9 \cdot 10^7$
FI05Y	5X,4X,4Y,4U,6X,6Y,6V	98.4	$2.9 \cdot 10^7$
FI06X	6Y,6V,5X,5Y,7X,7Y	99.0	$1.2 \cdot 10^7$
FI06Y	6V,6X,5X,5Y,7X,7Y	99.0	$1.2 \cdot 10^7$
FI06V	6X,6Y,5X,5Y,7X,7Y	97.2	$1.2 \cdot 10^7$
FI07X	7Y,6X,6Y,6V,8X,8Y	97.8	$0.5 \cdot 10^7$
FI07Y	7X,6X,6Y,6V,8X,8Y	96.0	$0.5 \cdot 10^7$
FI08X	8Y,7X,7Y	97.4	$0.5 \cdot 10^7$
FI08Y	8X,7X,7Y	96.9	$0.5 \cdot 10^7$

Table 4.4: The tracking efficiency of the SciFi stations. The sample is based on all physics data runs in the period 2002-P2C.

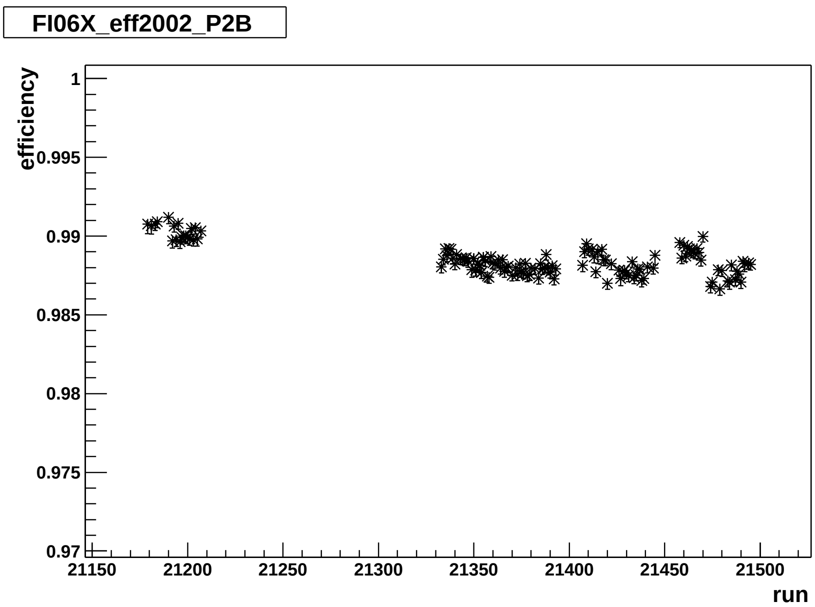

Figure 4.13: Tracking efficiency of SciFi station 6X in the period 2002-P2B. The hiatus in physics data-taking between runs 21200 and 21300 was due to a vacuum-leak in the target.

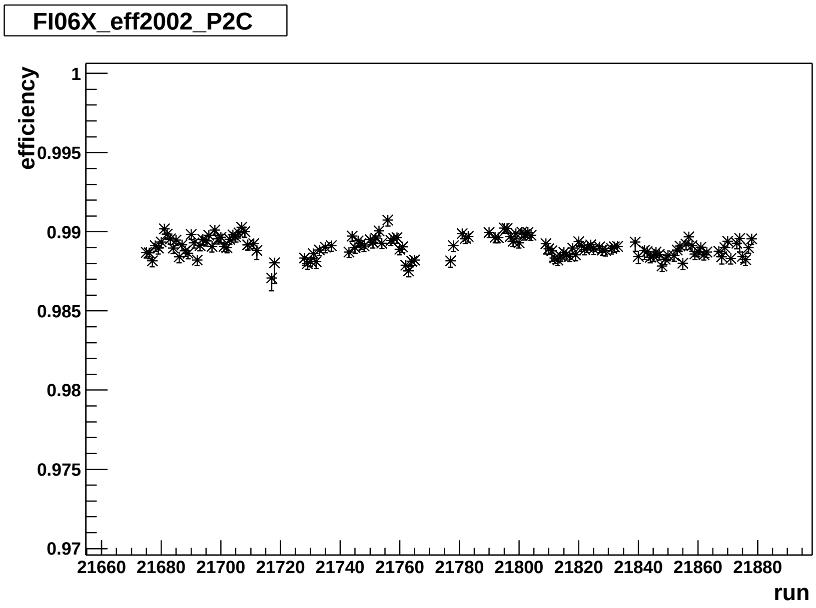

Figure 4.14: Tracking efficiency of SciFi station 6X in the period 2002-P2C.

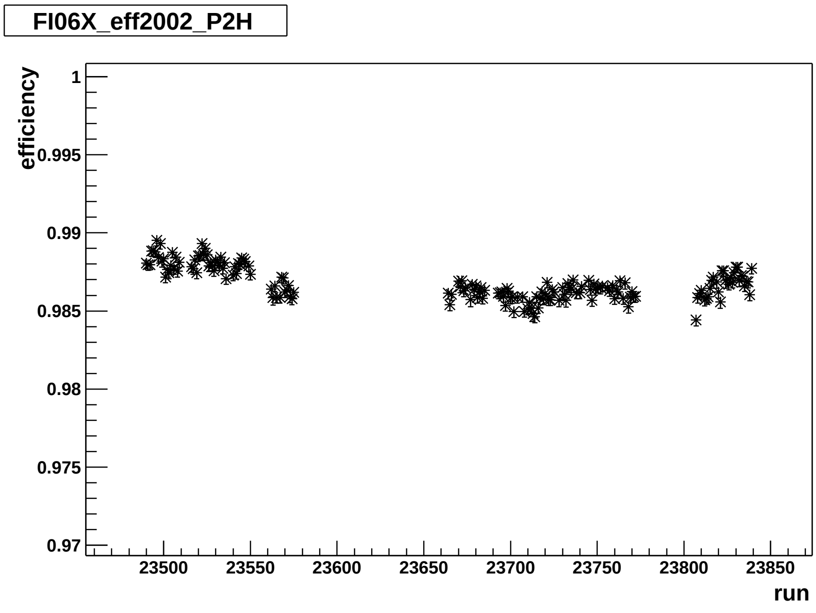

Figure 4.15: Tracking efficiency of SciFi station 6X in the period 2002-P2H. The hiatus in data-taking between runs 23570 and 23660 corresponds to the planned field-reversal of the target in this period.

	SciFiJ (FI03)	SciFiG (FI06)
total fibre radius [mm]	0.25	0.50
active fibre radius [mm]	0.235	0.44
pitch [mm]	0.43	0.7
overlap (adjacent channels) [mm]	0.04	0.18
overlap (% active radius)	17%	41%
multiplicity (before clustering)	8.7	15.6
multiplicity (after clustering)	8.5	9.0

Table 4.5: Geometric data for the Japanese and German-built SciFis, with average multiplicity per event. The small overlap between adjacent channels coupled with the peak-sensing discrimination used in the Japanese hodoscopes reduces the number of hits recorded in adjacent channels; the German SciFis record all hits, with the number being reduced by a clustering process when the data is produced.

4.5.2 Calculation of the Three-Plane Efficiency

The SciFi stations FI03, FI04 and FI06 offer a further possibility for determining their efficiency which also takes into account the geometrical relationship between reference and sought hits. In comparison to the method described in the previous section, it also possesses the significant advantage that the efficiency can be determined for each channel rather than just globally for the entire plane. In order to determine the efficiency for a hodoscope plane h_0, the other planes of the same station (h_1, h_2) are taken as references. For each event the steps described in the following sections are taken.

Clustering

First of all, the number of combinatorial possibilities in the two reference planes is reduced by combining hits in neighbouring channels which very probably were caused by the passage of the same particle. The hits combined in this *clustering* step must be strongly correlated in time; a 3σ cut on the time-difference distribution of the neighbouring hits is taken as the boundary. For station FI06 this corresponds to a cut of ± 40 TDC-channels, equivalent in double-precision mode (65 ps per TDC-channel) to some ± 2.6 ns. For the Japanese SciFi stations, where the peak-sensing discrimination mode and geometrically very small overlap between detector channels reduce the number of neighbouring hits to a minimum from the start, the clustering process has very little effect; for the Bonn/Erlangen SciFis on the other hand, the number of hits per event is reduced on average from 16 to 9, the level of the Japanese SciFis. The number of combinatorial possibilities with two reference planes is thereby reduced by a factor $16^2/9^2 \approx 3$ (see Table 4.5). The number of hits to be considered can be reduced still further by setting a trigger-correlated time-window. This means that all hits the calibrated times of which are outside a certain time from the zero-point of the channel in question are discarded.

Determining Expected Channels in h_0

Stations FI03, 04 and 06 comprise two orthogonal planes reading out in x and y and a third plane (U or V) at 45° to both of these. Taking any combination of hits in these two arbitrary reference planes, the channel where a hit is to be expected in the third plane can be calculated using the formula

$$V_{pred} = off - \frac{Y - X}{\sqrt{2}} \tag{4.4}$$

where off is an offset to be determined which takes into account that the three planes are not all exactly centered in relation to one another. Should the calculated channel lie outside the region corresponding to the projection of the active area of the three planes, the hit combination is discarded.

The minimum distance Δs between the channel expected from (4.4) and any channel to be found in the array of hits in h_0 for an event is calculated in a pre-loop for each h_1-h_2 hit combination. This value together with the time difference Δt between the h_1 and h_2 hits is taken as parameter for the calculation of a χ^2,

$$\chi^2 = \left(\frac{\Delta s}{\sigma_{\Delta s}}\right)^2 + \left(\frac{\Delta t}{\sigma_{\Delta t}}\right)^2 \tag{4.5}$$

which is taken as a measure of the probability of the combination. $\sigma_{\Delta s}$ and $\sigma_{\Delta t}$ are the widths of the two distributions. The χ^2 values for each h_1-h_2 are stored in a two-dimensional matrix. This matrix is combed first column-by-column and then row-by-row for the best χ^2 value. If the same combination is determined as the most likely column-by-column as line-by-line, i.e. if the independent conclusion is reached that a h_2 hit is the best partner for a h_1 hit and *vice versa*, this combination is taken as a pair and acts as a temporal and spatial reference point in the search for a correlated hit in the h_0 plane. If no agreement is found, the hits are discarded, since no unambiguous conclusion can be reached as to which h_1 and h_2 hits belong together.

Calculating the Efficiency

If a hit in the plane h_0 exists within a user-defined time-window around the average time of the h_1-h_2 hit and is also geometrically highly correlated to the point where a hit is expected, then this hit is deemed to have been detected efficiently by h_0. Such a hit not being found contributes to the inefficiency of the plane. The efficiency ϵ is given simply by

$$\epsilon = \frac{n_{found}}{n_{pred}} \tag{4.6}$$

where n_{found} is the number of hits found and n_{pred} the number of hits expected (i.e., the number of "valid" h_0-h_1 combinations) for the plane under investigation. The error $\delta\epsilon$ on this efficiency is asymmetric, since $\epsilon + \delta\epsilon$ cannot exceed 100%. It can be calculated from the binomial distribution and is given at the 1σ confidence level by [91]

23384 normal intensity			
FI...	X	Y	U/V
03	96.2	96.2	96.9
	± 0.04	±0.04	±0.04
04	96.4	96.4	97.2
	± 0.04	±0.04	±0.04
06	97.6	97.4	98.4
	± 0.04	±0.04	±0.04

22377 low intensity			
FI...	X	Y	U/V
03	98.0	98.4	98.5
	± 0.1	±0.1	±0.1
04	98.9	98.9	99.1
	± 0.1	±0.1	±0.1
06	98.5	98.8	99.4
	± 0.1	±0.1	±0.1

Table 4.6: The three-plane SciFi efficiencies for normal beam intensity (run 23384; left) and low intensity (run 22377; right). The values emerge from the analysis of all possible combinations of temporally correlated hits and represent therefore a worst-case scenario.

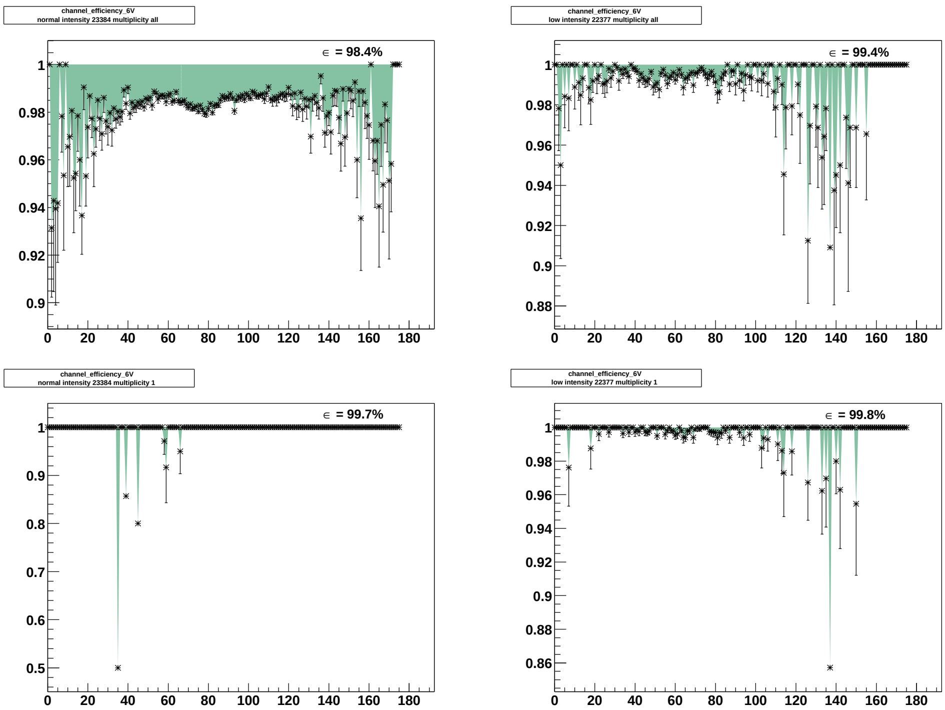

Figure 4.16: Efficiency of SciFi station 6V plotted across all channels: **(left)** normal beam intensity (run 23384) **(right)** low intensity (run 22377); **(above)** all multiplicities included **(below)** only events with multiplicity 1 in all planes. The apparently low efficiency at the sides of the plane is a result of the low statistics at the edge of the beam. The somewhat reduced efficiency in the central beam-region at full beam intensity (above left) is due to occupancy effects stemming from the very high rates involved.

$$\delta\epsilon = \frac{\frac{1}{2} \pm \sqrt{\epsilon(1-\epsilon)n_{pred} + \frac{1}{4}}}{n_{pred} + 1} \tag{4.7}$$

for the upper (+) and lower (-) error. The efficiencies calculated in this way for the planes of the SciFi stations FI03, FI04 and FI06 can be seen in Table 4.6, and the efficiency profile over all channels for normal beam intensity ($2.2 \cdot 10^8 \mu$ per SPS spill; top left) and low intensity ($3.5 \cdot 10^6 \mu$ pro SPS spill; top right) in Figure 4.16.

Since this method of calculating the efficiency uses the raw data directly, it can be used, for example, to investigate the effect of high hit multiplicity on the efficiency of a detector. The greater the number of registered hits per event in each plane is, the more combinatorial possibilities there are and the more difficult it is to ascertain which hits belong together. This effect can be clearly seen in Figure 4.16 on the left-hand side: whereas in the upper picture (events with all multiplicities) the efficiency is in general 98 - 99%, in the lower picture (only events with multiplicity 1 after clustering) it is nearly 100%. This number corresponds to the *intrinsic efficiency* of the detector, the likelihood that the hardware of the detector (scintillating fibres and photomultiplier) respond at the passage of a particle. This intrinsic efficiency may also be estimated by the analysis of data taken at lower beam intensity. Two such pictures, with all multiplicities (top) and only multiplicity-1 events (bottom) are to be seen on the right of Figure 4.16. Since the multiplicity in this case is by definition lower, there are proportionately more events with just multiplicity 1. The intrinsic efficiency of station 6V for example is estimated here to 99.8%.

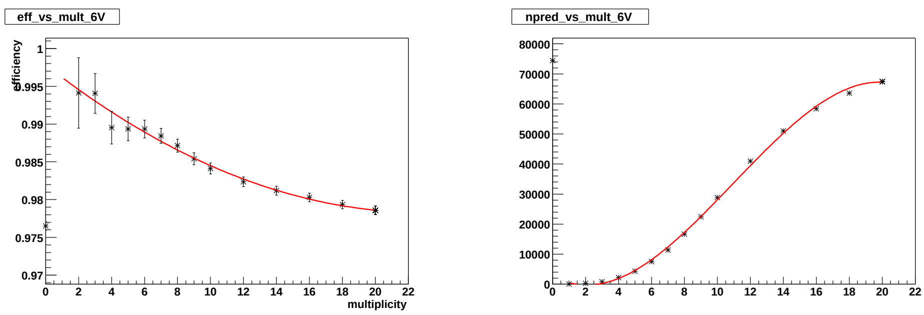

Figure 4.17: Efficiency **(left)** and number of expected hits **(right)** as a function of the multiplicity of an event (station 6V, 10000 events) . The multiplicity was artificially reduced when using the three-plane algorithm to determine the efficiency. At multiplicity = 0, the limit where all multiplicities are permissible is shown. This corresponds to the value given in Table 4.6 for normal beam intensity, 97.6%

A picture of the dependence of efficiency on multiplicity, together with the number of expected hits with growing multiplicity, is shown in Figure 4.17.

Chapter 5

Extraction of Transverse Spin Asymmetries at COMPASS

One of the main goals of the COMPASS experiment is to gain more exact knowledge of the transverse quark distribution functions $\Delta_T q(x)$. It was originally planned that about 20% of the total running-time should be spent on measurements with transverse target spin [17]; this allocation has been approximately held to. The Collins mechanism discussed in Section 2.6.4 is the favoured channel through which to gain access to $\Delta_T q(x)$. The following sections are devoted to the extraction of the Collins asymmetry from the data from the 2002 COMPASS beam-time.

5.1 Transverse Data 2002 and their Production

Measurements with transverse target polarisation (see Section 3.3.2) were taken during the 2002 COMPASS beam-time in three periods – P2B, P2C and P2H – each of approximately one week's length. In each period the two target cells possessed opposite polarisations. In principle the asymmetry could be calculated from the difference in the counting-rates in the two target cells, but this method is subject to systematic effects stemming from the differing acceptance of the two cells. In order to avoid such complications as far as possible, the polarisation of the cells is reversed between two data-taking periods, these being described as either *down-up* or *up-down* periods according to the spin configuration of the target cells (Figure 5.1). The counting-rate asymmetry is then calculated within the two target cells separately between two periods with opposite spin configurations. One polarisation reversal took place between the periods P2B and P2C, and a second in the middle of P2H. This period is therefore broken down further into sub-periods P2H.1 and P2H.2. Table 5.1 gives an overview of the periods and the amount of data taken in them.

The data-production process described in Section 3.8 was performed for the transverse periods in August and September 2003, once the production algorithms and the necessary aids such as calibration and alignment files had been finally settled. A pre-selection of the data suitable for production was made

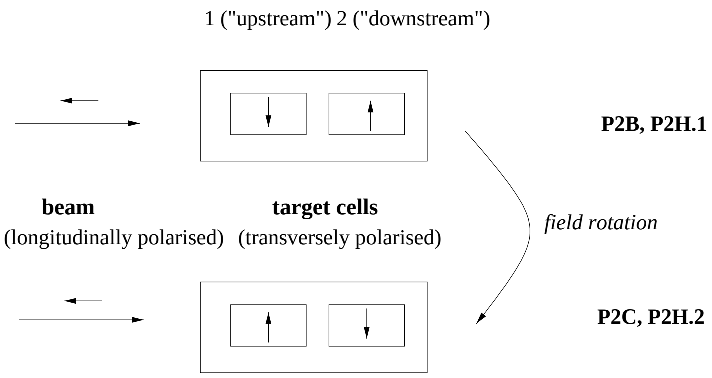

Figure 5.1: Schematic depiction of the target cells in transverse mode. Measurements are always performed with opposite polarisations in the two target cells. In order to avoid acceptance effects, the polarisation is reversed in both cells between periods.

Period	target polarisation	data produced	
		Runs	*GB*
P2B	$\Downarrow\Uparrow$	145	91.3
P2C	$\Uparrow\Downarrow$	145	97.2
P2H.1	$\Downarrow\Uparrow$	64	46.7
P2H.2	$\Uparrow\Downarrow$	112	84.0

Table 5.1: The transversity data-taking periods during the 2003 COMPASS beam-time. The spin of the target cells and the number of runs produced are shown. The target polarisation was reversed in the middle of period P2H, which is thus sub-divided into two shorter periods according to the spin configuration.

on the basis of criteria recorded in the online log-book such as beam stability, number of SPS spills, target polarisation and the magnetic fields of SM1 and SM2. Runs in which for whatever reason several detectors had malfunctioned were excluded. All data-*chunks* belonging to a run (generally some 100 of 1 GB each) were downloaded from tape and processed in parallel by CORAL. The output data were merged to form one file of on average some 0.6 - 0.7 GB (Figure 5.2).

Production-Efficiency Checks

The log-files produced during the processing of each runs were used to check how many chunks had been successfully completed. In a few isolated cases it occurred that some data contained in a chunk were corrupt, prohibiting further processing. The corrupt chunks were skipped and dis not affect the production of the runs further. Table 5.2 shows the number of such chunks in the transversity production. The failure rate was according to these figures on average around 0.1%.

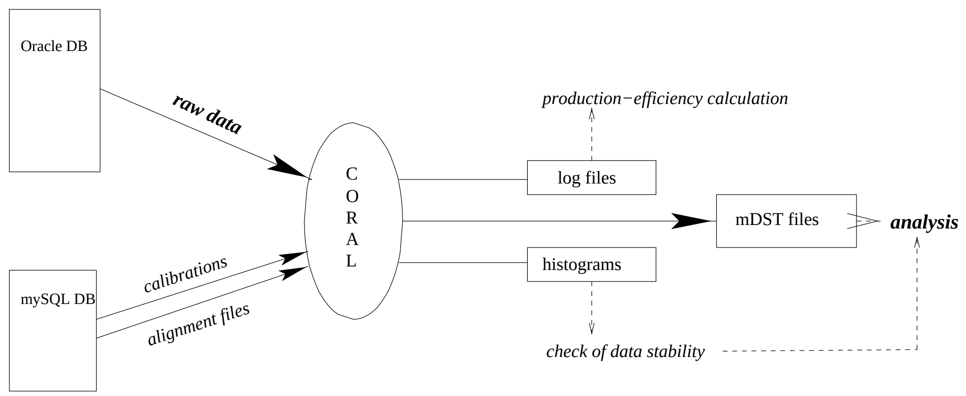

Figure 5.2: The production procedure with CORAL. Inputs are the raw-data files and the calibration and alignment files; outputs are log-files, ROOT histograms for stability checks on the data and the data themselves in *mini data storage* (mDST) format.

Period	no. of chunks	*of which corrupt*
P2B	ca. 13 800	11
P2C	ca. 13 700	0
P2H	ca. 16 300	41

Table 5.2: Unprocessed chunks in the transversity production.

Stability Checks

The integrity of the data over an entire period can be tested using ROOT histogram files created during production, or by further analysis of the mDST files. Various parameters were compared with an average value for a period or sub-period. These stability checks were divided into four categories:

- **Detector Stability:** Profiles of 260 detector planes were created during the production and checked for incongruities. Malfunctioning detector planes which had not been noted in the online logbook and which could compromise the data quality could be recognised at this stage.

- **Reconstruction Stability:** The stability of the following quantities was checked (Figure 5.3):

  – Number of tracks per reconstructed event in the whole spectrometer region and each sub-division of it (in front of the first spectrometer magnet SM1, behind the second magnet SM2, between the two);

  – Number of primary and secondary vertices[1] per event;

  – Number of clusters per event and detector plane.

[1] A *primary vertex* is one whose incoming particle has been identified as a beam particle. All other vertices are *secondary*.

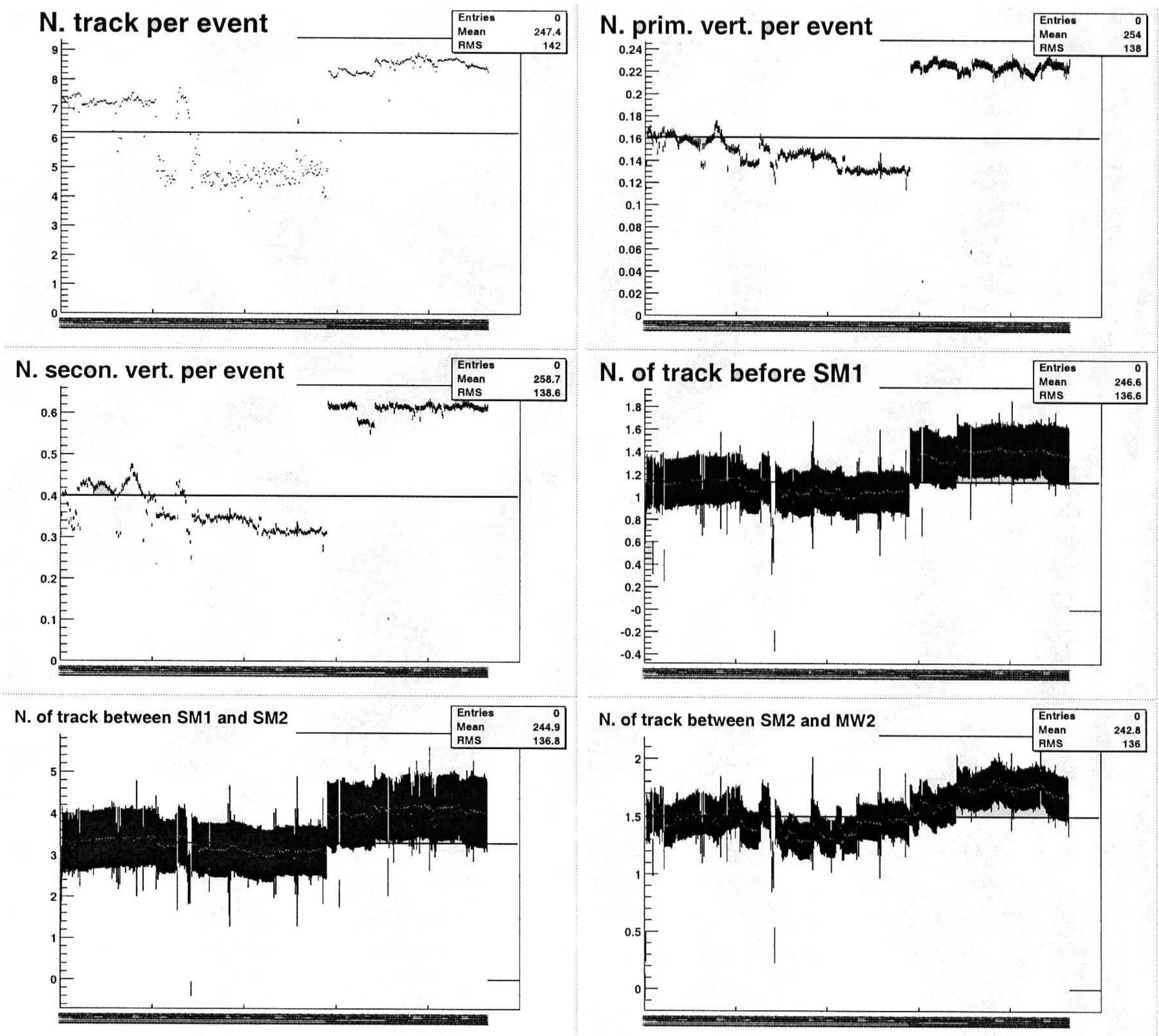

Figure 5.3: Overview of the reconstruction stability during the three periods P2B, P2C and P2H. Average number (per event) of reconstructed **(top left)** tracks in entire spectrometer **(top right)** primary vertices; **(middle left)** secondary vertices; **(middle right)** tracks in front of the spectrometer magnet SM1; **(bottom left)** tracks between SM1 and SM2; **(bottom right)** tracks behind the second spectrometer magnet SM2. Crucial when considering the compatibility of data periods is the number of primary and secondary vertices reconstructed. Whilst these quantities are comparable in P2B and P2C, in P2H they are significantly larger (right third of each plot). These two sets of data must therefore be analysed separately.

- **Kinematic Stability:** The stability of the following kinematic variables was checked:
  - the Bjorken scaling variable x;
  - the relative energy transfer y;
  - Q^2;
  - the transverse energy of the *leading hadron*[2] p_t;
  - the azimuthal angle of the leading hadron ϕ_h.

The following runs were shown as a result of these checks to be unstable and were excluded from the sample [92]:

- six runs (21762, 21763, 21764, 21765, 21777, 21778) in period P2C and one run in P2H (23767) because of instabilities in the detector profiles;
- three runs (P2B 21492, P2H 23503, P2H 23666) because of instabilities in the track reconstruction.

The single most important fact that emerged from the analysis of reconstruction and kinematic stability was the confirmation that data from the periods P2B and P2C on the one hand and from both sub-periods of P2H on the other could not be combined. The COMPASS spectrometer was still being commissioned in the beam-time in 2002: whilst periods P2B and P2C followed on from one another, one month passed before the data in P2H were taken. In this time new detectors and adjustments to the trigger influenced the data-taking considerably. This can be seen for example in the number of primary vertices reconstructed per event: in P2B and P2C this remains stable at around 0.14 - 0.16, but in P2H it increases to 0.23.

The Collins asymmetry must therefore be extracted separately for the period-pairs P2B/P2C and P2H.1/P2H.2. Only at the very end may the numerical values for the asymmetry be combined, weighted according to the statistics from each period.

K^0 Reconstruction

The global stability of the production can best be checked by extracting a known physical quantity from the data. A tried and tested method at COMPASS is the extraction of the K^0 mass [93]. The analysis was performed with the COMPASS analysis program PHAST (see Section 3.8) using the available mDST data. Vertices possessing two outgoing tracks (so-called V0-vertices) were sought more than 20 cm downstream from the second target cell. Such vertices are very likely caused by short-lived neutral kaons decaying to two pions [94]

$$K_s^0 \to \pi^+\pi^- \qquad (68.60 \pm 0.27\%) \tag{5.1}$$

[2]leading hadron = the hadron produced in the scattering process with the largest proportion of the available energy

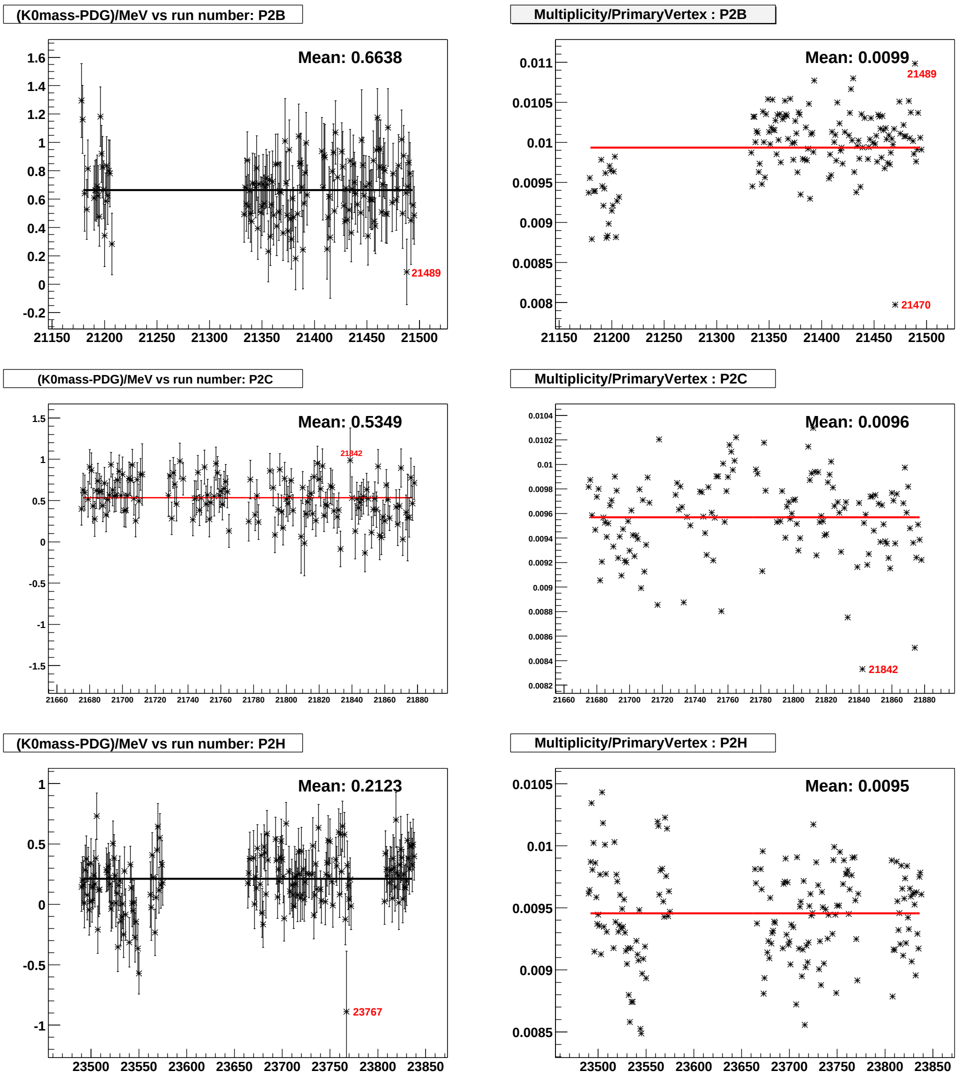

Figure 5.4: K^0 analysis of the transversity data for P2B (top), P2C (middle), P2H (bottom): **left** the mass difference $M(\pi^+\pi^-) - M(K^0, PDG)$; **right** K^0 events per primary vertex.

The only other significant decay mode, to two neutral pions, produces no measurable tracks in the COMPASS spectrometer. The mass in the $\pi^+\pi^-$-frame is compared with the K^0-mass from the *Particle Data Group* (PDG) of 497.672 MeV. If the reconstructed mass is within 100 MeV of this value, a K_s^0 event is registered.The following quantities are plotted for a period as measures of the stability of the data in a run:

- the mass difference $M(\pi^+\pi^-) - M(K^0, PDG)$;
- the width of the mass-difference distribution;
- the number of K^0 events per primary vertex;
- the number of K^0 events normalised to the beam intensity.

The first and third of these distributions are shown in Figure 5.4. The data show a remarkable stability, with the reconstructed mass varying in a limited range between 0 and 1 MeV above the PDG K^0 mass. In all periods a K_s^0 event is registered in approximately one in 100 reconstructed primary vertices. Only four runs - P2B 21470 and 21489, P2C 21842 and P2H 23767 - were excluded from the final data-sample as a result of larger deviations ($> \pm 3\sigma$) from one or other of the averages for the period.

5.2 Event Selection

For the calculation of the Collins asymmetry, deep-inelastic scattering events in which at least one hadron is produced are required. Such events represent only a small proportion of the data produced. Kinematic and other cuts detailed in the following sections are applied in order to reduce the sample to the relevant events. A schematic overview of the event-selection algorithm applied is given in A.

5.2.1 Q^2 Reduction

Several branches of the physics analysis at COMPASS, such as that to determine the gluon polarisation ΔG (Section 2.5), deal with events in the whole kinematic range of Q^2 right down to values $Q^2 \approx 0$ (exchange of a quasi-real photon). For the transversity analysis, only events in the deep-inelastic limit are of interest. $Q^2 > 1$ is generally taken as the defining condition. Since the events measured by the COMPASS spectrometer lie principally in the range of low Q^2, this cut represents a considerable reduction in the data of a factor 7 - 8 (Figure 5.5)[3]. The Q^2 reduction is performed therefore separately run-for-run and the reduced data-files saved to tape, in order to reduce the computing power required for the further steps of the analysis.

[3]The allocation of a Q^2-value to an event demands naturally that a beam and scattered muon have been detected; events where both are not found are also discarded at this point.

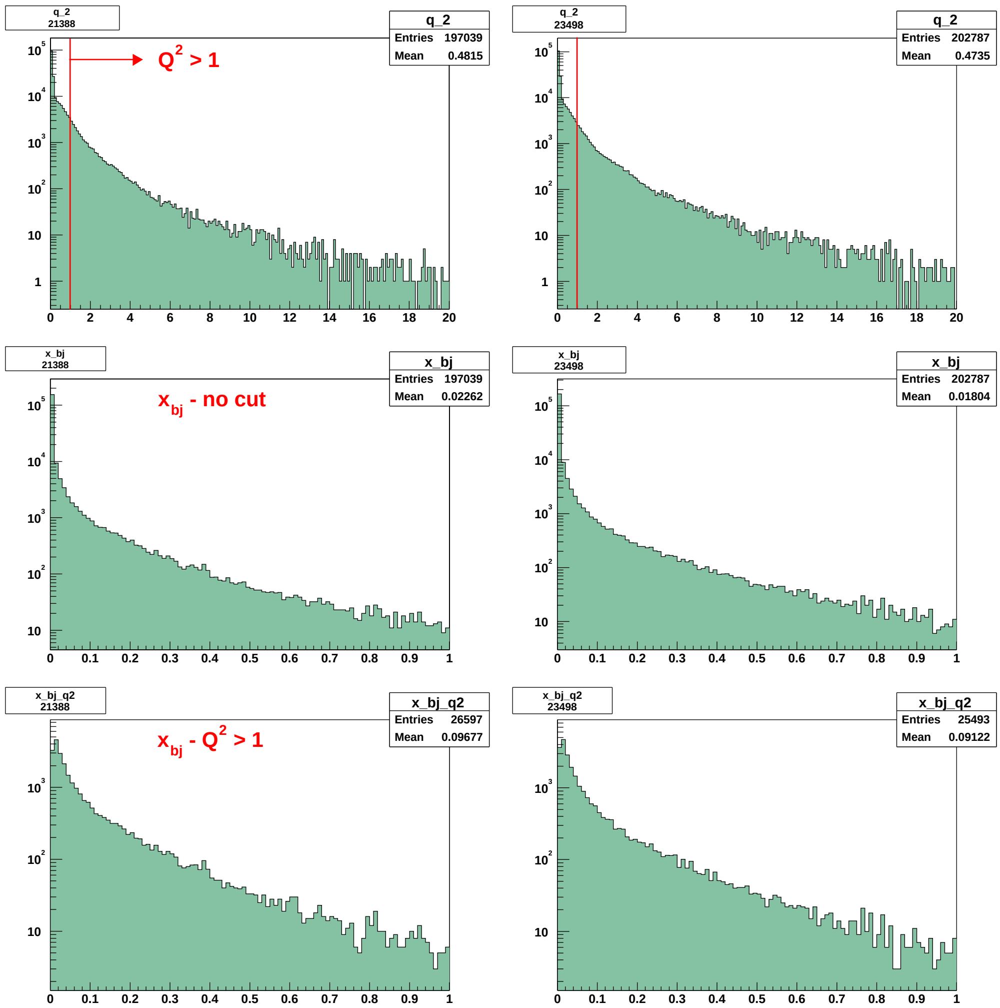

Figure 5.5: Reduction of the data-sample to scattering events with $Q^2 > 1$ for a representative run from the transversity periods P2B (21388; left) and P2H (23498, right): **(top row)** Q^2 distribution before the reduction; **(middle row)** Bjørken-x distribution before the reduction; **(bottom row)** Bjørken-x distribution after the reduction. The requirement $Q^2 > 1$ reduces the quantity of data by a factor 7-8.

5.2.2 Cuts on the Primary Vertex and Muons

Selection of Beam and Scattered Muons

Those beam and scattered muons identified as such by CORAL during the production process are in the first instance accepted. Only the "best" primary vertices identified on the basis of their reduced χ^2 and the number of outgoing particles are used in the reconstruction.

When the mDST data are produced, a total χ^2 fit is calculated for each track expressing the summed probability that each hit assigned to the track does in fact belong to it. A reduced χ^2 can be constructed from this value, given by

$$\chi^2_{red} = \frac{\chi^2_{total}}{N_{hits} - 5}, \tag{5.2}$$

where N_{hits} is the number of hits along the track. The reduction of five in the number of degrees of freedom emerges from the five parameters which are extracted from the track: two co-ordinates (x, y; z is pre-determined by the first hit on the track), two direction cosines ($\frac{dx}{dz}$, $\frac{dy}{dz}$) and the momentum of the track. A reduced χ^2 for beam or scattered muon greater than 10 leads to the event being discarded (Figure 5.6).

Since the COMPASS trigger hodoscopes do not cover the full kinematic range in the large-angle spectrometer, calorimeter information must be used to identify the scattered muon in this region. This can lead to muons that are scattered at large angles not being recognised as such. These muons must be specially extracted from the data by accepting as a scattered muon additionally any particle that causes more than four hits in the first detector of the Muon Wall at the back of the large-angle spectrometer and more than six in the second detector. This detector system is positioned behind a 60 cm thick iron block and should therefore only detect highly penetrative muons. For around every 100 events with a normally-flagged scattered muon, one event is found with a such a "regained" muon. These muons are however of great importance for the extraction of the Collins asymmetry, since they occur by definition in events in the high x-Bjørken region, where the asymmetry should be at its largest.

Since one cannot *a priori* explain what kind of reaction would produce a normal scattered muon and simultaneously a "regained" muon, events with both are discarded. Similarly, those few events where more than one large-angle muon can be regained are also not considered.

Cuts on the Variables y and W

A further cut is applied on events with very large and very small values of the kinematic variable y (relative energy-loss of the muon in the scattering process). Events with $y < 0.1$ belong to the elastic region and are excluded. Since the COMPASS trigger can only reliably identify events up to approximately $y = 0.9$ (c.f. Figure 3.13), events with larger y are discarded. These cuts lead

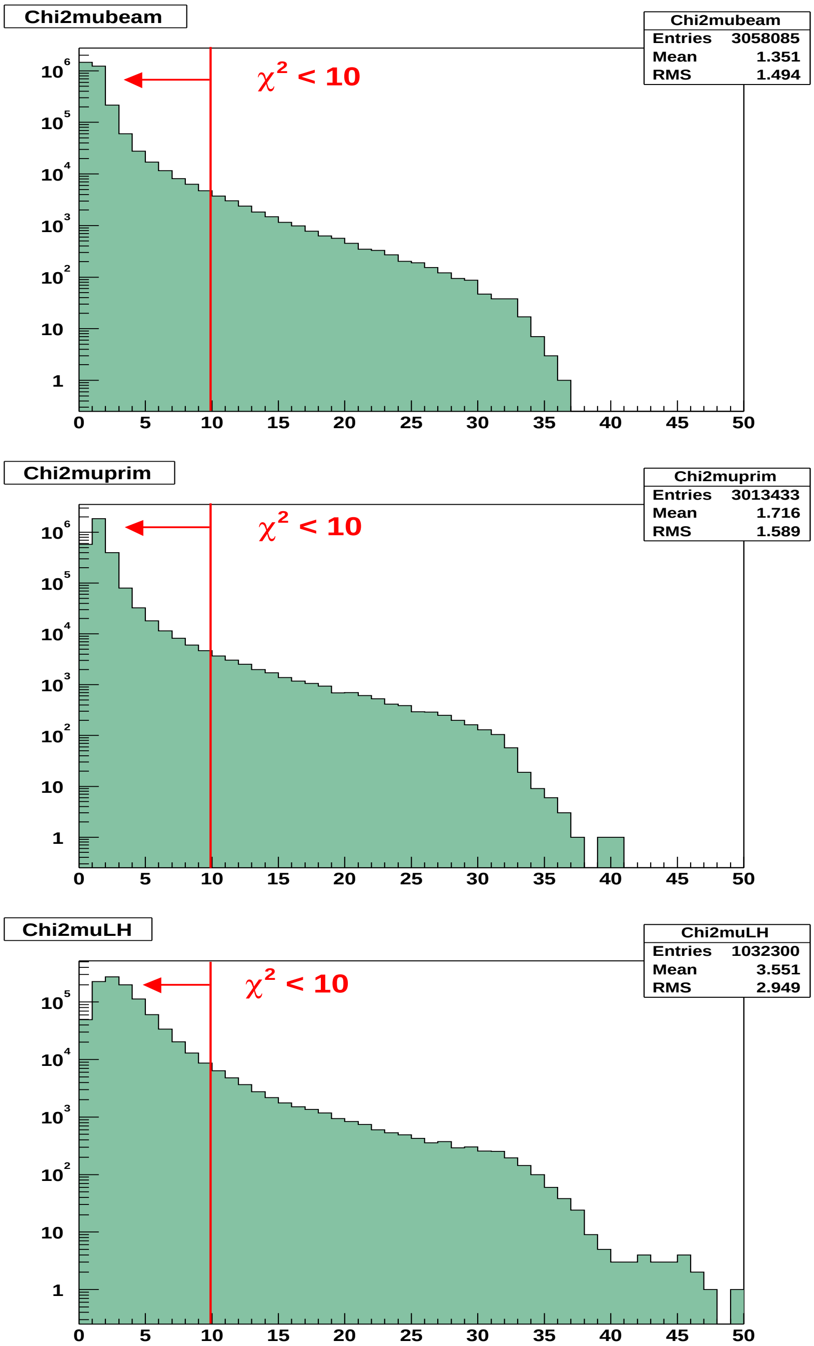

Figure 5.6: Distribution of the reduced χ^2 of the track of the **(top)** beam muon, **(middle)** scattered muon **(bottom)** most energetic hadron in an event. The average χ^2 for beam and scattered muons is lower than that for particles identified as hadrons. This is due in part to the many detectors specifically intended for muon identification in the beam-region (SciFis etc.), in part to the great number of combinatorial possibilities in the region behind the target. $\chi^2 < 10$ is required for all particles used in the analysis.

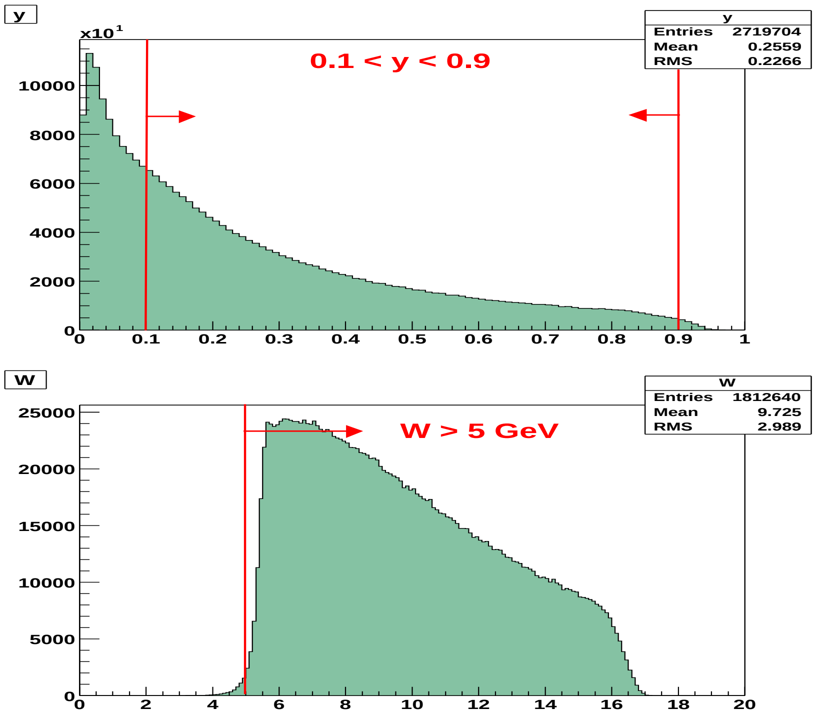

Figure 5.7: y- and W-cuts. Whilst a significant number of events is discarded by the y-cut, the W-cut, which is applied immediately afterwards and ensures a purely inelastic sample above the region of the nucleon resonances, discards only a very few events.

to a further reduction in the number of events of around 30 % compared to the sample-size after the Q^2-cut.

The cut on y causes elastic scattering events to be almost entirely excluded. In order to increase this probability still further, an explicit cut on the centre-of-mass energy of the hadronic system created in the scattering process is also applied. The requirement $W > 5$ GeV removes from the sample events in the region of the nucleon resonances. The Q^2- and y-cuts already applied mean that only some 0.3% of the surviving events are affected by this cut (Figure 5.7).

Target Cuts

It is essential in the event selection that a primary vertex is found inside one of the two target cells. These lie in the COMPASS coordinate system in z between -100 cm and -40 cm (the first or *upstream* cell) and -30 cm and +30 cm (the second or *downstream* cell). All vertices outside these regions are discarded (Figure 5.8).

The COMPASS target cells are cylindrical with a radius of 1.5 cm. Whereas in the purely longitudinal magnetic field they are almost exactly centred on the

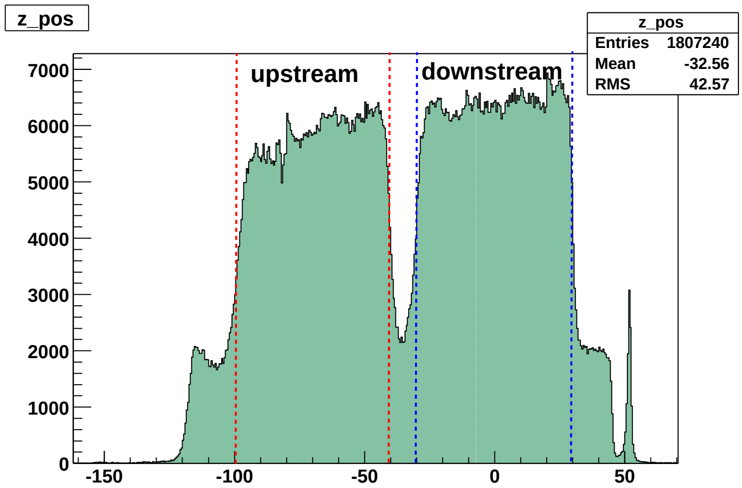

Figure 5.8: Requirement of a vertex in the target (i): cut along the beam-axis (z).

null (x,y) axis of the co-ordinate system, the additional dipole field in transverse mode shifts the target cells almost uniformly by 0.25 cm to the Jura side and by 0.05 cm downwards. In order to be certain that no vertex outside the target is accepted, all vertices with a radial distance $r > 1.3$ cm from the adjusted central axis at x = -0.25 cm, y = -0.05 cm are discarded (Figure 5.9).

5.2.3 Determining the Leading Hadron

The *flavour* of the outgoing quark in the fragmentation process – which is by definition also the quark struck by the photon in the scattering process – largely determines what type of hadron is produced with the largest momentum or energy [95, 37]. The unfavoured fragmentation functions are found to be heavily suppressed and can be neglected (c.f. (2.122) - (2.124)). The production of a π^+ (quark content $u\bar{d}$) or a π^- (quark content $\bar{u}d$) contains a differing contribution from the transverse u and d quark distributions, allowing conclusions to be drawn as to the form of each. From this point in the analysis on, the sample is therefore divided into two: events containing a positively-charged leading hadron, and those in which the leading hadron has negative charge.

A high degree of security is required that the leading hadron as identified in the event selection is indeed a hadron. Possible impurities caused by falsely identified muons must be eliminated. The existence of such a mixing of the identified hadron and muon samples in the data production (see Section 3.8) is made clear by the following discrepancies:

- Some particles identified as scattered muons cause no hits in either the second Muon Wall at the back of the small-angle spectrometer or in the MWPC detectors immediately behind, a case rendered impossible by the

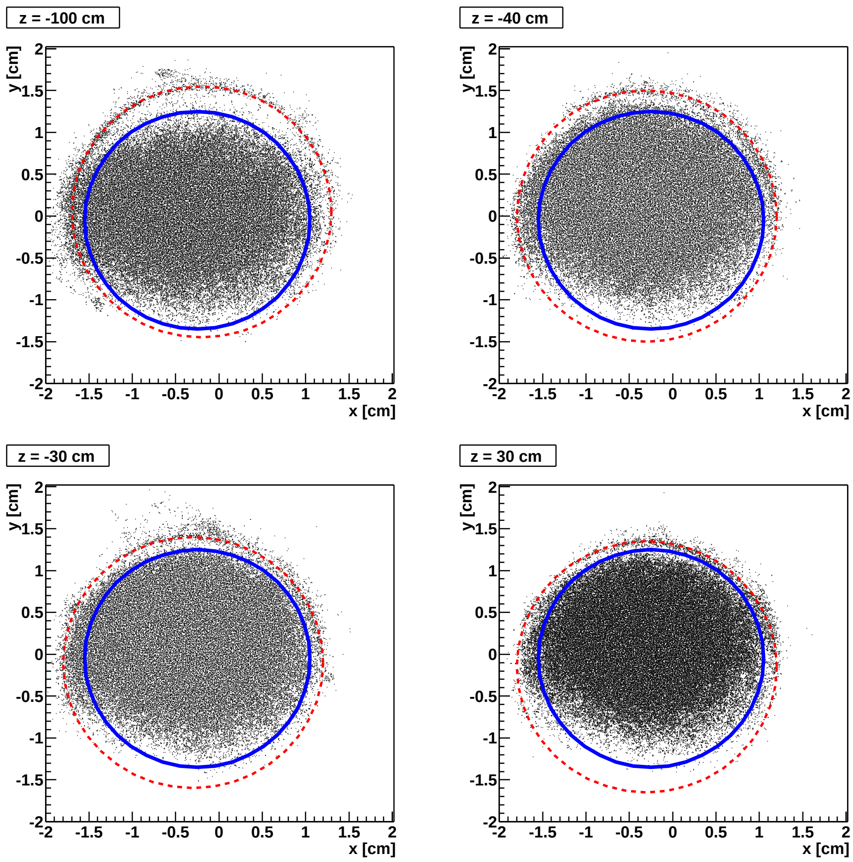

Figure 5.9: Requirement of a vertex in the target (ii): radial cut. The target cells are shifted relatively uniformly away from the nominal null-point by the transverse dipole field. The red (dotted) circles indicate the target position (radius 1.5 cm) as determined at the ends of each of the two target cells. The blue (continuous) line is drawn at 1.3 cm radius from the new null-axis, assumed to be at (x,y) = (-0.25 cm, -0.05 cm) along the whole length of the cells.

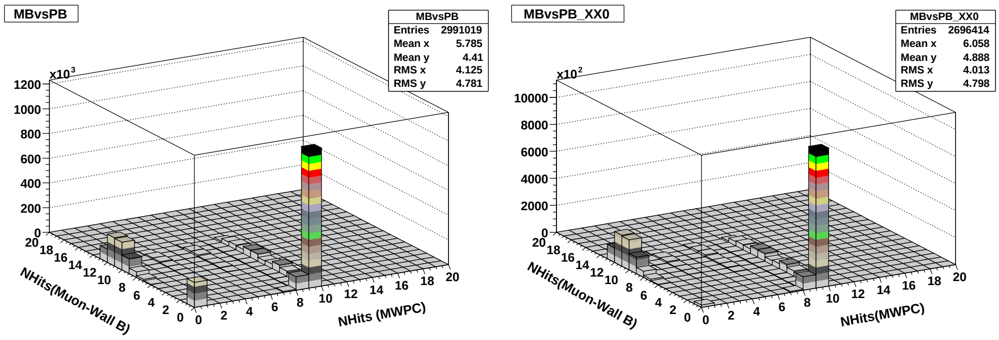

Figure 5.10: Hadronic impurity in the muon sample: the number of particles identified as scattered muons causing a certain number of hits in the second Muon Wall (left axis) and in the MWPCs immediately behind this detector system (right axis) is shown. According to the geometry of the two detector systems a muon must cause hits at least one of the two: the peak at (0,0) cannot be easily explained if the particles are muons. It is highly likely that they are falsely identified hadrons; demanding a nuclear interaction length $nXX_0 > 30$ removes these particles from the sample.

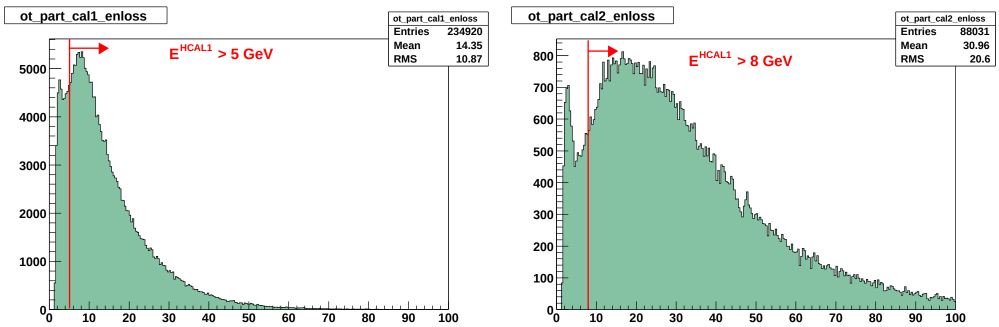

Figure 5.11: Energy deposition (GeV) in the hadron calorimeters HCAL1 and HCAL2 (frequency distribution for all particles identified as leading hadrons). Demanding a minimum energy deposition of $E_{HCAL1} > 5$ MeV or $E_{HCAL2} > 8$ purges the sample of falsely identified muons at low energies.

geometry of the two detectors. These particles are most likely not highly penetrative muons, but falsely identified hadrons. (Figure 5.10).

- The distributions of energy deposited in the hadron calorimeters HCAL1 and HCAL2 by those particles identified as leading hadrons contains an excess of particles depositing only a very small amount of energy. These are very probably muons (Figure 5.11).

The following further cuts on the data allow these inconsistencies to be eliminated, albeit with a significant loss of events:

- A certain *nuclear interaction length* nXX_0 is demanded for the muon and hadron samples. This quantity indicates how much energy a particle must have lost in the spectrometer under the assumption that it was a hadron: a hadron with $nXX_0 = x$ would have only a fraction $1/2^x$ of its original energy at the end of the reconstructed track. A particle which has over its entire track length lost a great deal of energy and possesses therefore a high value of nXX_0 is very likely a muon. For the purposes of this analysis, a scattered muon is only accepted as such if it satisfies the condition $nXX_0 > 30$. Hadrons must possess $nXX_0 < 10$. These conditions eliminate for example the impurity in the muon sample identified in Figure 5.10.

- A minimum energy deposition in the cluster associated with the hadron in HCAL1 or HCAL2 is required, specifically $E_{HCAL1} > 5$ MeV or $E_{HCAL2} > 8$ MeV. When no calorimeter cluster is found associated with the hadron with the largest momentum, this hadron is still accepted and the event not discarded.

5.2.4 Kinematic Cuts on Leading Hadrons: z, p_t

The kinematic variable z expresses the proportion of the photon energy transferred to the struck quark and consequently to the hadron produced in the fragmentation. The higher the energy of the leading hadron, the greater is the probability that it is the hadron initially produced at the start of the fragmentation chain. At lower values of z, impurities occur through, for example, secondary interactions of the original hadron with the target material. This can lead to the identified leading hadron having the opposite charge as the actual leading hadron, since the determination of the particles' charge and energy only occurs outside the target through measurement of their deflection in the magnetic field and the energy they deposit in the calorimeters. Monte-Carlo studies show that the probability of identifying a "false" leading hadron is in fact dominant at low values of z. From $z \sim 0.4$ upwards, the proportion of falsely reconstructed hadrons is no longer significant (Figure 5.12) [17, 97]. Since the COMPASS kinematics are skewed to lower values of z, a cut at $z = 0.25$ is applied in order to keep the loss of events within an acceptable bound (Figure 5.13). 40% of the events remaining after all previous cuts are however still lost.

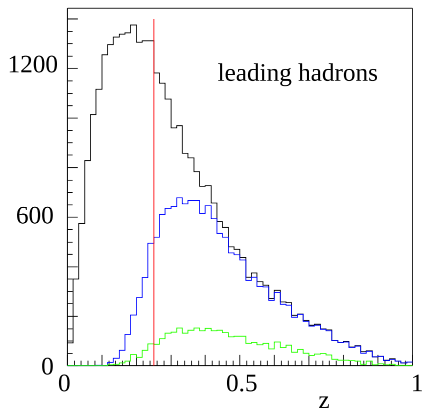

Figure 5.12: The probability of falsely identifying the most energetic hadron in an event decreases with increasing z, as does the number of events. A cut at $z = 0.25$ as shown represents a compromise which takes into account these two facts. Black (upper line) - all reconstructed hadrons; blue (middle line) - correctly identified hadrons; green (lower line) - neutral leading hadrons [from Monte-Carlo studies in [96]].

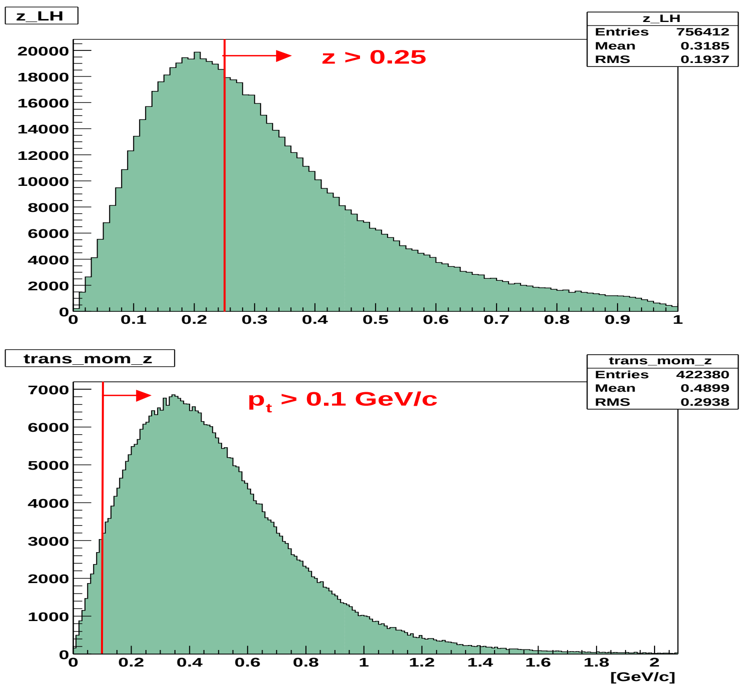

Figure 5.13: z- and p_t-cuts. The z-cut ensures a higher certainty that the identified leading hadron was also the most energetic product of the primary process. The p_t-cut allows the azimuthal angle of the hadron momentum to be determined reliably.

An additional requirement is that the leading hadron possess a transverse momentum component $p_t > 0.1$ GeV/c. This is solely in order to ensure a reliable determination of the hadron momentum vector used in the calculation of the Collins angle.

5.2.5 Impurities from Unidentified Leading Hadrons

As the COMPASS spectrometer is not in a position to identify neutral tracks, it is also possible that the particle with the greatest energy of all products of the scattering process was a neutral hadron. Such events must be excluded from the sample, since the "sub-leading" hadron taken is expected to exhibit a fundamentally different Collins asymmetry. In order to identify these events, the sum of all z-values of hadrons in the primary vertex (i.e. all particles not identified as muons or "recovered" in the large-angle spectrometer) is calculated. Subtracting this quantity from unity gives the "missing" z-component. If this is greater than the z-value of the particle identified as the leading hadron, then it is possible that a neutral particle with a greater momentum was produced in the interaction (it could equally be several particles each with a smaller proportion of the energy than the identified leading hadron). To clarify this point, a search is made for any clusters in the hadron calorimeters HCAL1 and HCAL2 that possess a greater energy that the energy of the identified leading hadron and which have no track associated with them. This requires

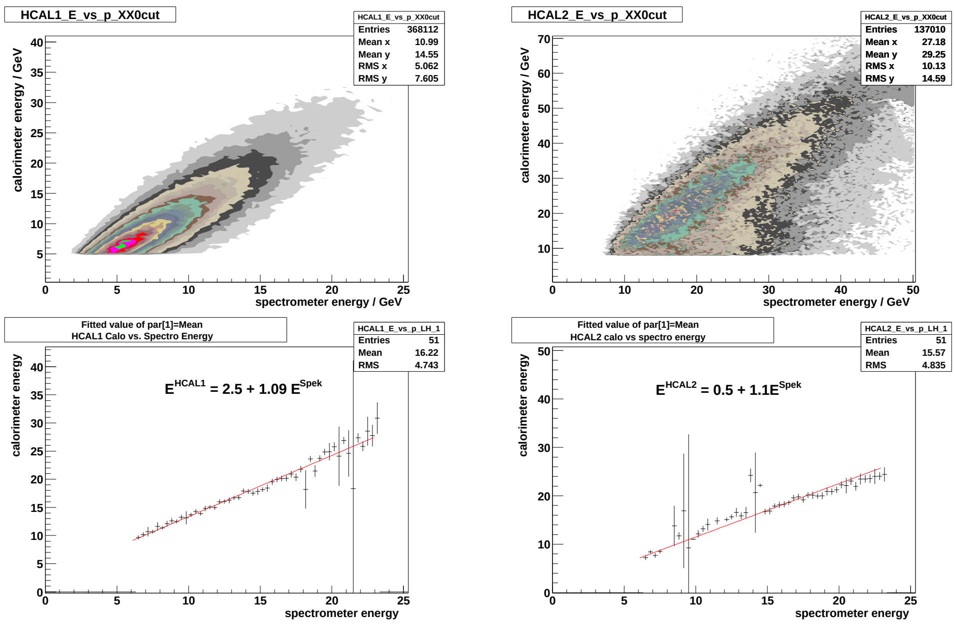

Figure 5.14: (above) Energy deposited in the calorimeter (y-axis) against the particle energy calculated through track reconstruction in the magnetic field;**(below)** Average energy deposition in the calorimeter as a function of the energy from track reconstruction: for HCAL1 **(left)** and HCAL2 **(right)**

knowledge of the correlation between the calculated momentum of a particle and the energy which it deposits in the calorimeter. Since the determination of the energy is more accurate in the spectrometer than in the calorimeter, the energy of the cluster associated with the leading hadron is not taken directly. Instead the spectrometer energy is converted to a calorimeter energy using a calibration relation. Plotting the average deposited energy in the calorimeter $E^{HCAL1,2}$ for each bin of spectrometer energy $|p_h|$, a straight-line fit may be drawn from which the necessary correlation may be read off (Figure 5.14). The formulae for HCAL1 and HCAL2 are found to be

$$E^{HCAL1} = 2.5 + 1.09 \cdot |p_h| \tag{5.3}$$
$$E^{HCAL2} = 0.5 + 1.10 \cdot |p_h| \tag{5.4}$$

where the units in the energy range in question are GeV. Parallel investigations of the energy resolution $\sigma_E^{HCAL1,2}$ of the hadron calorimeters produces the values

$$\sigma_E^{HCAL1} = 0.8\sqrt{E^{HCAL1}} \tag{5.5}$$
$$\sigma_E^{HCAL2} = 0.6\sqrt{E^{HCAL2}} \tag{5.6}$$

On the basis of these values, a further cut was introduced in order to eliminate any impurity through unidentified leading hadrons. Events where there is a cluster in one of the calorimeters the energy of which is in the range

$$E_{clus} > E^{HCAL1,2} + 2\sigma_E^{HCAL1,2} \tag{5.7}$$

and with which no track is associated are discarded.

5.3 Final Data-Sample

Following the cuts listed in the previous sections, the event samples listed in Table 5.3 survived in the four periods with transverse target spin. The distributions of the important kinematic variables may be seen in Figure 5.15. The variant acceptance of the target cells is clearly to be seen in the difference in sample size between the two. It is also important to note that whilst P2B and P2C contain approximately equal numbers of events, P2H.1 and P2H.2 have highly differing sample sizes, meaning that the asymmetry from these periods will have a higher statistical uncertainty.

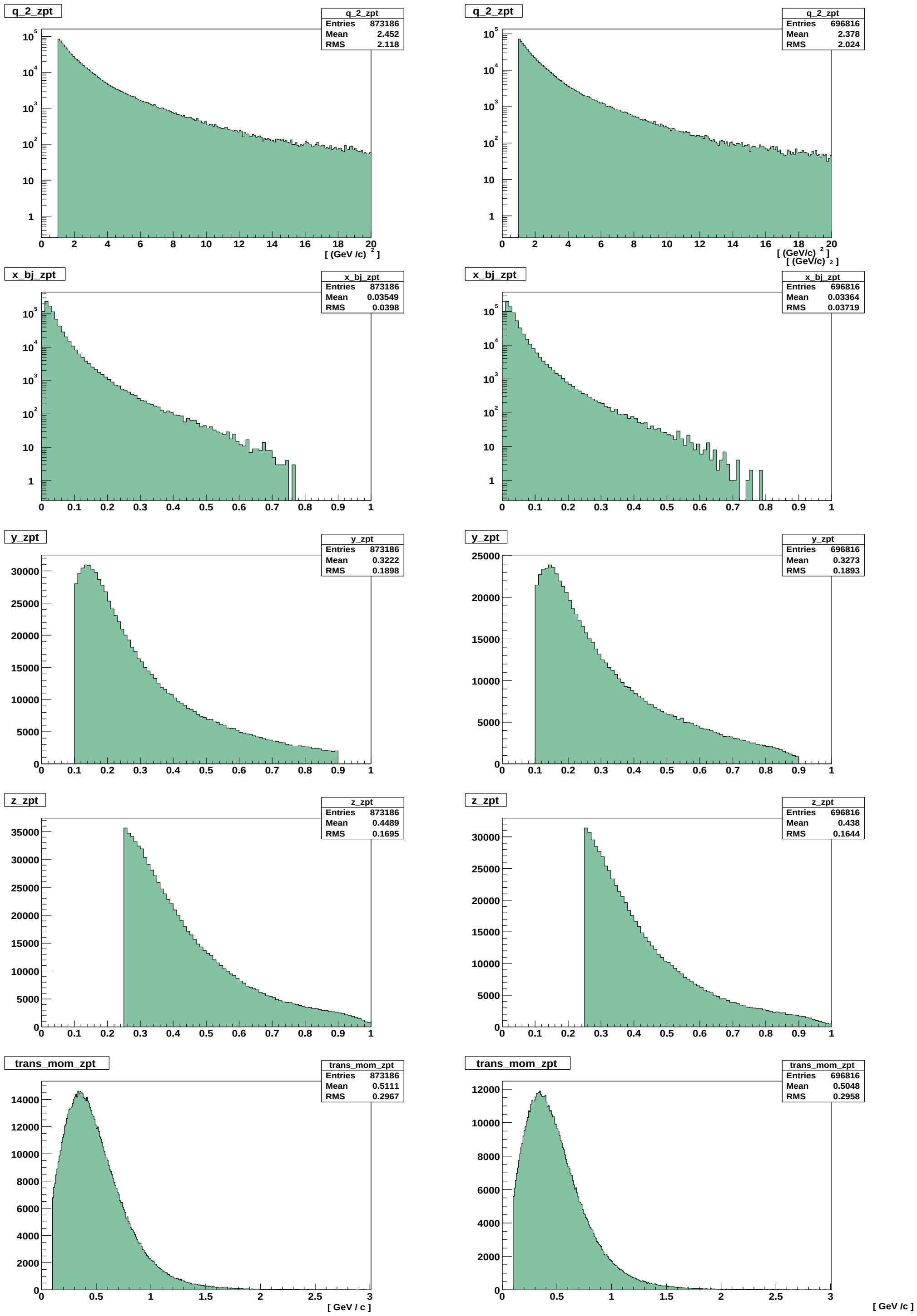

Figure 5.15: The distributions of the important kinematic variables in the final sample: **(left)** positive leading hadrons; **(right)** negative leading hadrons. From top to bottom: Q^2 (logarithmic scale); x (logarithmic scale); y; z; p_t.

10^3 **events**	P2B pos	P2B neg	P2C pos	P2C neg	P2H.1 pos	P2H.1 neg	P2H.2 pos	P2H.2 neg
$Q^2 > 1$ GeV/c^2	3218		3344		1564		2720	
$+\ 0.1 < y < 0.9$	1995		2146		1056		1813	
$+\ W > 5$ GeV	1990		2140		1053		1807	
target in z	1586		1715		845		1447	
+ in r	1343		1447		718		1226	
vertex with hadron	1086		1174		586		1000	
charge = 1 or -1	585	501	633	541	315	270	538	462
$nXX_0 < 10$	555	482	600	521	299	260	509	443
calo. cut	502	433	542	468	272	235	463	401
$\nexists E^{HCAL}_{q=0} > p_h$	443	378	479	409	239	204	407	349
$+\ z > 0.25$	257	205	279	222	138	111	234	188
$+\ p_t > 0.1$ GeV/c	247	197	268	213	132	106	225	181
upstream cell	103	84	112	91	56	46	95	78
downstream cell	144	113	156	122	77	61	130	103

Table 5.3: Data-sample after each cut detailed in Section 5.2, in thousands of events.

5.4 Calculation of the Raw Asymmetries

The complete expression for the transverse interaction cross-section may be written (c.f. (2.120))

$$\begin{aligned} A_T^h &:= \frac{d\sigma^{\Uparrow} - d\sigma^{\Downarrow}}{d\sigma^{\Uparrow} + d\sigma^{\Downarrow}} \\ &= D_{NN}\frac{\sum_i e_i^2 \Delta_T q_i(x) \Delta_T^0 D_i(z, \vec{P}^2_{h\perp})}{\sum_i e_i^2 q_i(x) D_i(z, \vec{P}^2_{h\perp})} |\vec{S}_\perp| \sin\phi_C \end{aligned} \tag{5.8}$$

where D_{NN} is the depolarisation factor, $\vec{S}_\perp$ the transverse polarisation of the target, and ϕ_C the Collins angle. The COMPASS collaboration defines the Collins angle according to the convention of the SMC experiment with a phase difference of π compared to the definition in (2.115). The relation used is $\phi_C = \phi_S + \phi_h - \pi$, where ϕ_S and ϕ_h are the azimuthal angles respectively of the nucleon spin-vector in the initial state ($\vec{S}$) and of the hadron momentum ($\vec{p}_h$). Since most measurements are taken on top of an unpolarised background, a counting-rate asymmetry $A_N(\phi_C)$ which should take the form

$$A_N(\phi_C) = A_0 \pm A_1 \sin\phi_C \tag{5.9}$$

is expected. A_0 is the unpolarised counting-rate asymmetry, which should remain constant if the acceptance remains the same. The "raw" asymmetry A_1 is composed of all pre-factors in (5.8) together. Plotting the measured counting-rate asymmetry against the Collins angle one expects a sine curve, the amplitude of which corresponds to the unscaled Collins asymmetry.

5.4.1 Calculation of the Collins Angle ϕ_c

The Collins angle ϕ_C is usually defined for a deep-inelastic scattering event in the Breit frame of reference and is calculated from the appropriate vectors (momentum of the leading hadron and spin of the nucleon) in this system. This is a somewhat complicated procedure, since the vectors must be transformed several times, first from the laboratory frame (in which the kinematic data of the particle tracks is calculated in the production process) into a system where the direction of flight of the beam muon defines the forward axis, and then through the $\gamma^\star N$-system via a Lorentz boost into the Breit system. This analysis follows the alternative and equivalent method suggested in [98] which uses only vector products in the laboratory system to define the angles required for the calculation of the Collins angle. Two unit-vectors are defined event-by-event: $\hat{k}$ from the cross-product of the momentum vectors of beam and scattered muon; and $\hat{m}$ from the difference of these two vectors. A third unit-vector $\hat{l}$ orthogonal to these two completes the definition of the frame of reference. The angles ϕ_h, ϕ_S may then be defined thus in this system:

$$\cos\phi_h = \frac{\hat{m} \times \vec{p}_h}{|\hat{m} \times \vec{p}_h|} \cdot \hat{k} \tag{5.10}$$

$$\cos\phi_s = \frac{\hat{m} \times \vec{S}}{|\hat{m} \times \vec{S}|} \cdot \hat{k} \tag{5.11}$$

The Collins angle may by definition be calculated from these two angles.

5.4.2 Experimental Extraction of the Raw Asymmetries

Although it should in principle be possible to take data in one period with transverse and opposite spin in the two target cells and calculate the asymmetry from the difference in the counting rates between the two cells, it is advisable because of the different acceptance of the cells to measure in two periods with the target spin being flipped between the two. The counting-rate asymmetry between two periods with opposite polarisation is therefore measured for both target cells separately. In the analysis of the 2002 data, the asymmetry between P2B and P2C and between P2H.1 and P2H.2 was calculated for eight bins of equal size in the range $0 < \phi_C < 2\pi$:

$$A_N(\phi_C) = \frac{N^{P2B,P2H.1}(\phi_C) - R \cdot N^{P2C,P2H.2}(\phi_C)}{N^{P2B,P2H.1}(\phi_C) + R \cdot N^{P2C,P2H.2}(\phi_C)} \tag{5.12}$$

R is a simple normalising factor taking into account the different total sample sizes in the periods under comparison,

$$R = \frac{N_{tot}^{P2B,P2H.1}}{N_{tot}^{P2C,P2H.2}}. \tag{5.13}$$

The counting-rates over the spectrum of ϕ_C for two different ranges of the kinematic variable x for periods P2B and P2C may be seen in Figure 5.16. A clear

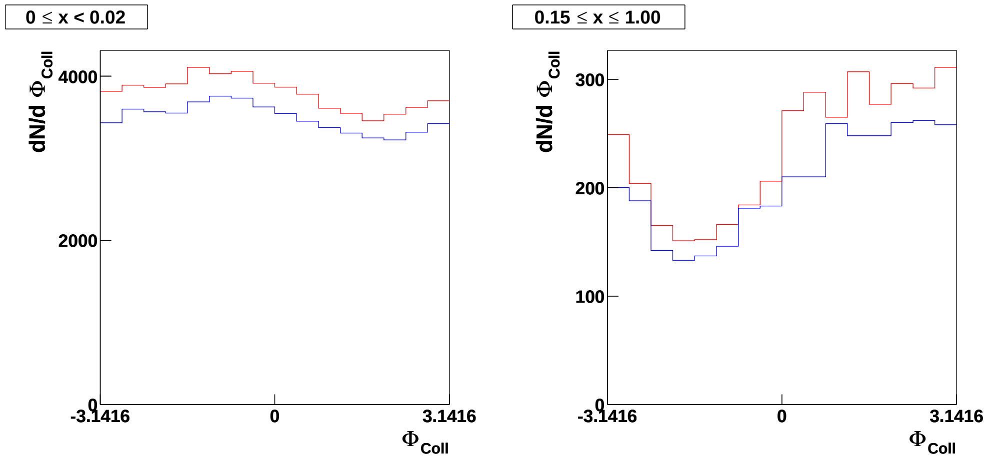

Figure 5.16: Counting rates in the periods P2B (lower (blue) line) and P2C (upper (blue) line) plotted against the Collins angle for two different regions of the kinematic variable x. The variable counting-rates in each period are taken into account by the normalisation factor R (5.13). A systematic effect, larger at higher values of x, caused by the different acceptance of the two target cells can also be seen: the spectrometer is clearly more sensitive to events involving hadrons emitted at larger angles on one side than on the other. The measurement method using the two target cells of opposite polarisation in order to compare counting-rates in one cell under different spin configurations is designed to avoid this problem.

acceptance effect may be seen in this picture, an effect which the measurement method with two oppositely and reversibly polarised target cells should eliminate.

The counting-rates are measured as a function of ϕ_C, since $\sin \phi_C$ is an argument of the cross-section. The physically observable asymmetry is however expected in the production angle ϕ_h of the leading hadron. In calculating the asymmetry, it is assumed that the target spin is always pointing in the same direction (upwards). A hadron produced at a particular azimuthal angle therefore always registers the same value of the Collins angle (Figure 5.17, Table 5.4). At the point of its calculation, the sign of the asymmetry for one cell (by convention upstream) is then reversed, in order to obtain an asymmetry uniformly in the form in (5.8), i.e. spin-up − spin-down:

	Polarisation				Assumption	
	Actual		Assumed		True/False	
P2B/P2H.1	$\Downarrow$	$\Uparrow$	$\Uparrow$	$\Uparrow$	F	T
P2C/P2H.2	$\Uparrow$	$\Downarrow$	$\Uparrow$	$\Uparrow$	T	F

Table 5.4: Actual and assumed polarisations.

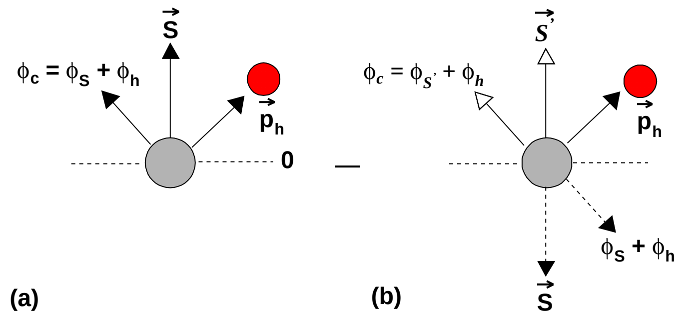

Figure 5.17: In order to compare counting-rates at the same azimuthal angle in a parameterisation with ϕ_C, the polarisation is always assumed to be pointing upwards, even when it is in fact pointing downwards (**b**) .

$$
\begin{aligned}
A_N &:= \frac{d\sigma^{\Uparrow} - d\sigma^{\Downarrow}}{d\sigma^{\Uparrow} + d\sigma^{\Downarrow}} && (5.14)\\
&= -\frac{(N^{P2B,P2H.1} - R \cdot N^{P2C,P2H.2})}{N^{P2B,P2H.1} + R \cdot N^{P2C,P2H.2}}, \mathit{upstream} && (5.15)\\
&= \frac{N^{P2B,P2H.1} - R \cdot N^{P2C,P2H.2}}{N^{P2B,P2H.1} + R \cdot N^{P2C,P2H.2}}, \mathit{downstream} && (5.16)
\end{aligned}
$$

The error on this asymmetry can be calculated to be

$$
\sigma_{A_N} = \sqrt{\frac{4N^{P2B,P2H.1} \cdot N^{P2C,P2H.2}}{(N^{P2B,P2H.1} + N^{P2C,P2H.2})^3}} \tag{5.17}
$$

These counting-rate asymmetries are plotted separately for the upstream and downstream target cells and for positive and negative leading hadrons against ϕ_c. The data are split into different kinematic regions in x and in z since the asymmetry should according to (5.8) be a product of x-dependent distribution functions and z-dependent fragmentation functions. The x- and z-bins used are

$$
\begin{aligned}
0 < \; & x < 0.02\\
0.02 <= \; & x < 0.05\\
0.05 <= \; & x < 0.10\\
0.10 <= \; & x < 0.15\\
0.15 <= \; & x < 1
\end{aligned}
\qquad\qquad
\begin{aligned}
0.25 <= \; & z < 0.4\\
0.4 <= \; & z < 0.6\\
0.6 <= \; & z < 0.8\\
0.8 <= \; & z < 1.0
\end{aligned}
$$

It should be noted that the kinematic range covered by COMPASS in x runs only from around $x = 0.03$ to $x = 0.8$, with the number of events decreasing steeply towards higher x. The division of the events according to their x- and z-values can be found in Appendix B. About 80% of all events fall within the first two x-bins. A finer binning has subsequently been introduced which better takes into account the higher statistics at small values of x.

With reference to (5.9), the data for each cell are fitted with a function of the form $A_0 + A_1 \sin \phi_c$. The fit coefficient A_1 corresponds to the value of the raw Collins asymmetry for the kinematic region and target cell in question, and is plotted against x or z accordingly. A weighted mean of the raw asymmetry for each data point in both target cells can then be taken.

5.5 From the Raw Asymmetry to the Collins Effect

The objective is to gain from the raw asymmetries an insight into the unknown product from (5.8),

$$A_C = \frac{\sum_i e_i^2 \Delta_T q_i(x) \Delta_T^0 D_i(z, \vec{P}_{h\perp}^2)}{\sum_i e_i^2 q_i(x) D_i(z, \vec{P}_{h\perp}^2)}, \tag{5.18}$$

which is the expression for the Collins asymmetry. The transversity distributions $\Delta_T q_i(x)$ may be extracted from this expression up to an unknown z-dependent normalisation. The Collins asymmetry is related to the raw asymmetry A_1 through

$$A_C = \frac{A_1}{D_{NN} \cdot |\vec{S}_\perp|} \tag{5.19}$$

where $|\vec{S}_\perp|$ is the average polarisation of the target material given by the measured polarisation P multiplied by a further *dilution factor*, f. This factor takes into account how much of the target material is polarisable, and must be calculated for the exact target set-up. The proportion of this polarisation transferred by the virtual photon is given by the depolarisation factor D_{NN}, which is defined from the kinematics of each individual event.

5.5.1 Target Polarisation and Dilution Factor

A direct measurement of the COMPASS target polarisation is not possible in transverse mode. The polarisation values are obtained through interpolation of the target polarisation curve over the whole beam-time and are set out in Table 5.5.

The naïve assumption of a dilution factor of 0.5 with a deuterium target, since one-half of all the nucleons is polarisable, is found to be too high because of the presence of other non-polarisable materials in the target cells. As the current COMPASS target was inherited from the SMC experiment, calculations from SMC regarding the dilution factor could be modified for the COMPASS kinematics [99]. The factor is found to vary slightly with x, with a value in the

Period	Runs	Polarisation	
		upstream	downstream
P2B	21178-21207	-49.79	54.58
P2B	21333-21393	-47.79	47.40
P2B	21407-21495	-47.09	46.33
P2C	21670-21765	52.50	-44.09
P2C	21777-21878	50.36	-43.06
P2H.1	23490-23575	-49.83	52.11
P2H.2	23664-23839	47.45	-41.41

Table 5.5: Calculated values for the COMPASS target polarisation in the transverse data-taking periods.

x	< 0.02	$0.02 - 0.05$	$0.05 - 0.10$	$0.10 - 0.15$	> 0.15
$D_{nn}(up)$	0.373	0.371	0.378	0.383	0.39
$D_{nn}(down)$	0.383	0.381	0.389	0.394	0.4

Table 5.6: Value from [99] for the *dilution factor* in different regions of x for the upstream and downstream target cells.

relevant range of just under 0.4. Although these data values were calculated for the longitudinal mode, there is no significant difference for transverse running [100]. The values for the different x-bins can be seen in Table 5.6. For the z-binning a constant value of $f = 0.38$ was assumed.

5.5.2 Depolarisation Factor

The depolarisation factor is given for the transverse case by (c.f. (2.113))

$$D_{NN} = \frac{2(1-y)}{1+(1-y)^2}. \tag{5.20}$$

This factor is calculated from the kinematics of each scattering event in the data-sample. It is multiplied by the appropriate value for the polarisation from Table 5.5 according to the the run it occurs in and the target cell where the vertex was found, and then used to weight the event. This weighting can, because of the method used to calculate the asymmetry, only be used as an value averaged over the two data periods under comparison in each bin in ϕ_c and x or z. The depolarisation factor is in general greater than 0.95; only for the region with $x < 0.02$ is it significantly smaller, $D_{NN} \sim 0.8$. Together with the target polarisation of around 0.5 and the dilution factor of around 0.38, the scaling factor from raw to Collins asymmetry comes to $1/(0.95 \cdot 0.5 \cdot 0.38) \approx 5.5$ (≈ 7 for the first x-bin) (Figure 5.18). The values of the scaling factor $1/(f \cdot D_{NN} \cdot P)$ for each bin in the final sample (split for P2B/C, P2H.1/P2H.2; positive/negative leading hadrons) may be found in Appendix B.

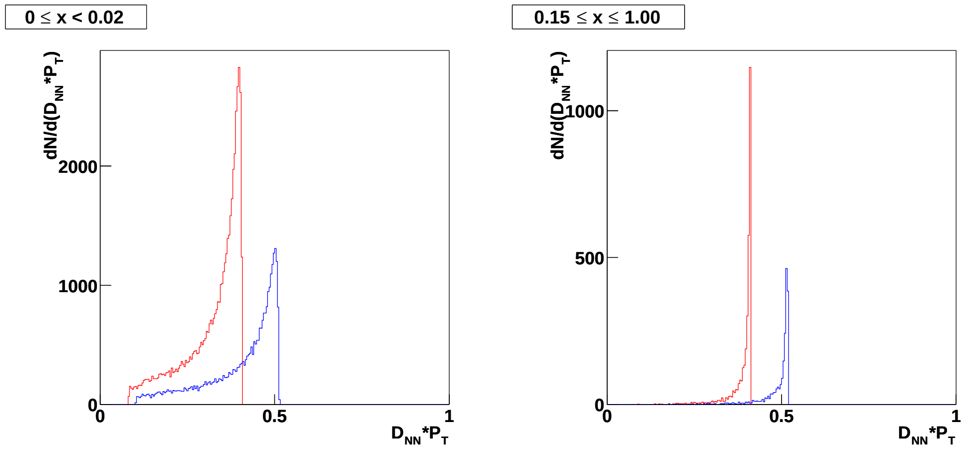

Figure 5.18: The factor $D_{NN} \cdot P$ for all events in the periods P2H.1 (blue peak to the left in both plots) and P2H.2 (red peak to the right) for two different ranges of x, downstream target cell. The maximum value of this factor corresponds to the polarisation in the cell, 52.11% and (-)41.41% respectively in P2H.1 (Table 5.5). At higher values of x almost the entire polarisation is transferred by the virtual photon in the great majority of cases (right-hand plot); at lower values of x (left-hand plot), this is not always the case – the distribution stretches to much lower values.

5.6 Results for the Collins Asymmetry

5.6.1 Asymmetries from the Individual Periods and Target Cells

The values for the Collins asymmetry for the individual target cells in the different periods established following the procedure described in the preceding sections are presented in Figures (5.19 - 5.22). In Appendix C, the numerical values presented in the plots are listed separately for the target cells and as a mean value over both cells, weighted according to the relative number of events in each. The statistical error for each value is also shown.

5.6.2 Asymmetries from all 2002 COMPASS Data

As far as the physics involved is concerned, the Collins asymmetry should only be calculated separately for positive and negative leading hadrons. The asymmetries averaged over both target cells for the paired periods P2B/C and P2H.1/H.2 should therefore be combined with an appropriate weighting

$$A_C^{comb}(x;z) = \frac{N^{P2BC}(x;z) \cdot A_C^{P2BC}(x;z) + N^{P2H}(x;z) \cdot A_C^{P2H}(x;z)}{N^{P2BC}(x;z) + N^{P2H}(x;z)} \tag{5.21}$$

Since the number of events from each second period (P2C, P2H.2) has already been normalised to that from the first period (P2B, P2H.1) according to (5.12), only the number of events from the first period must be taken into account for

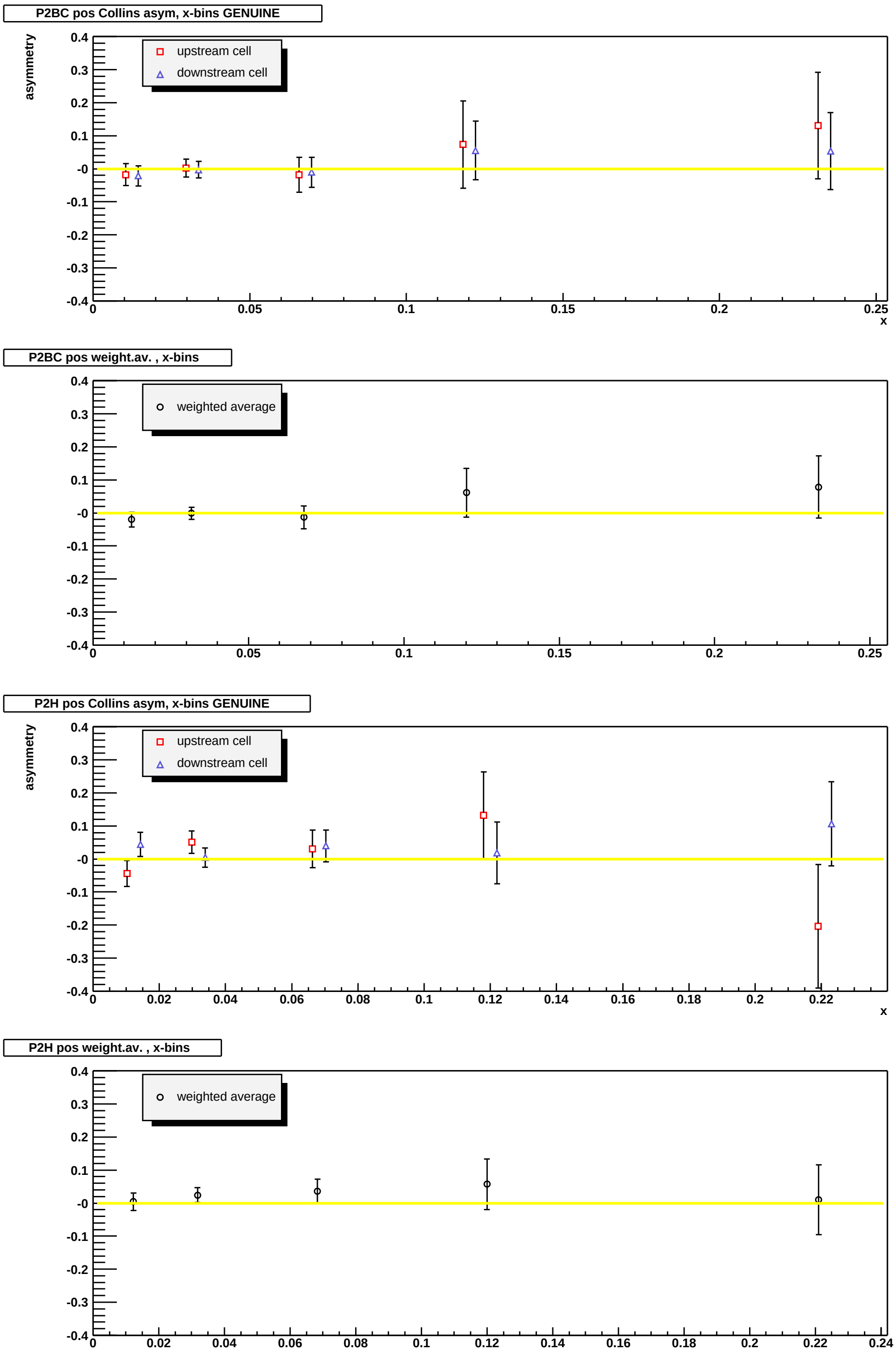

Figure 5.19: Collins Asymmetry from the COMPASS data 2002; positive leading hadrons, x-dependence:
(a) P2BC upstream, downstream target cell;
(b) P2BC weighted mean for both target cells;
(c) P2H upstream, downstream target cell;
(d) P2H weighted mean for both target cells.

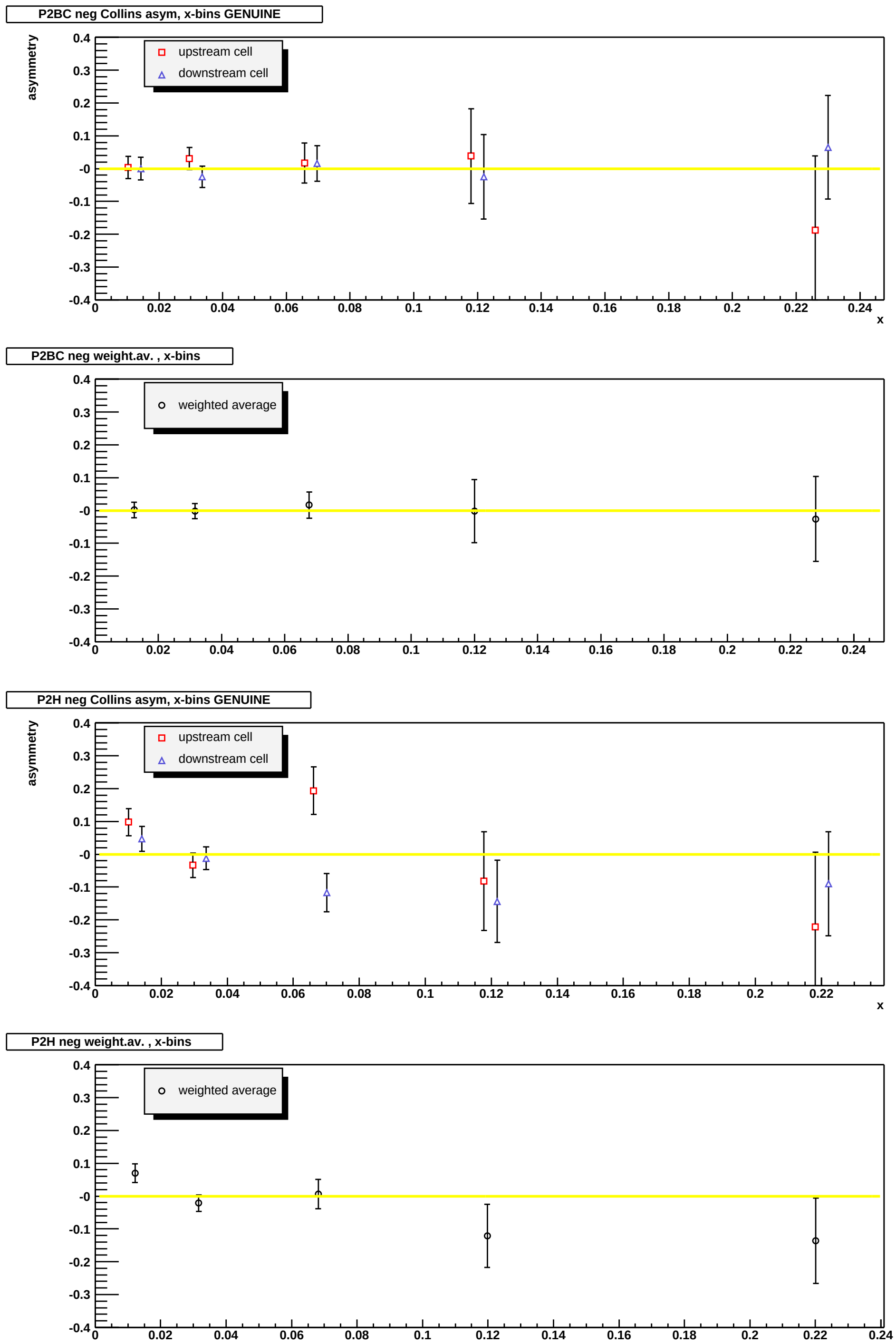

Figure 5.20: Collins Asymmetry from the COMPASS data 2002; negative leading hadrons, x-dependence:
(a) P2BC upstream, downstream target cell;
(b) P2BC weighted mean for both target cells;
(c) P2H upstream, downstream target cell;
(d) P2H weighted mean for both target cells.

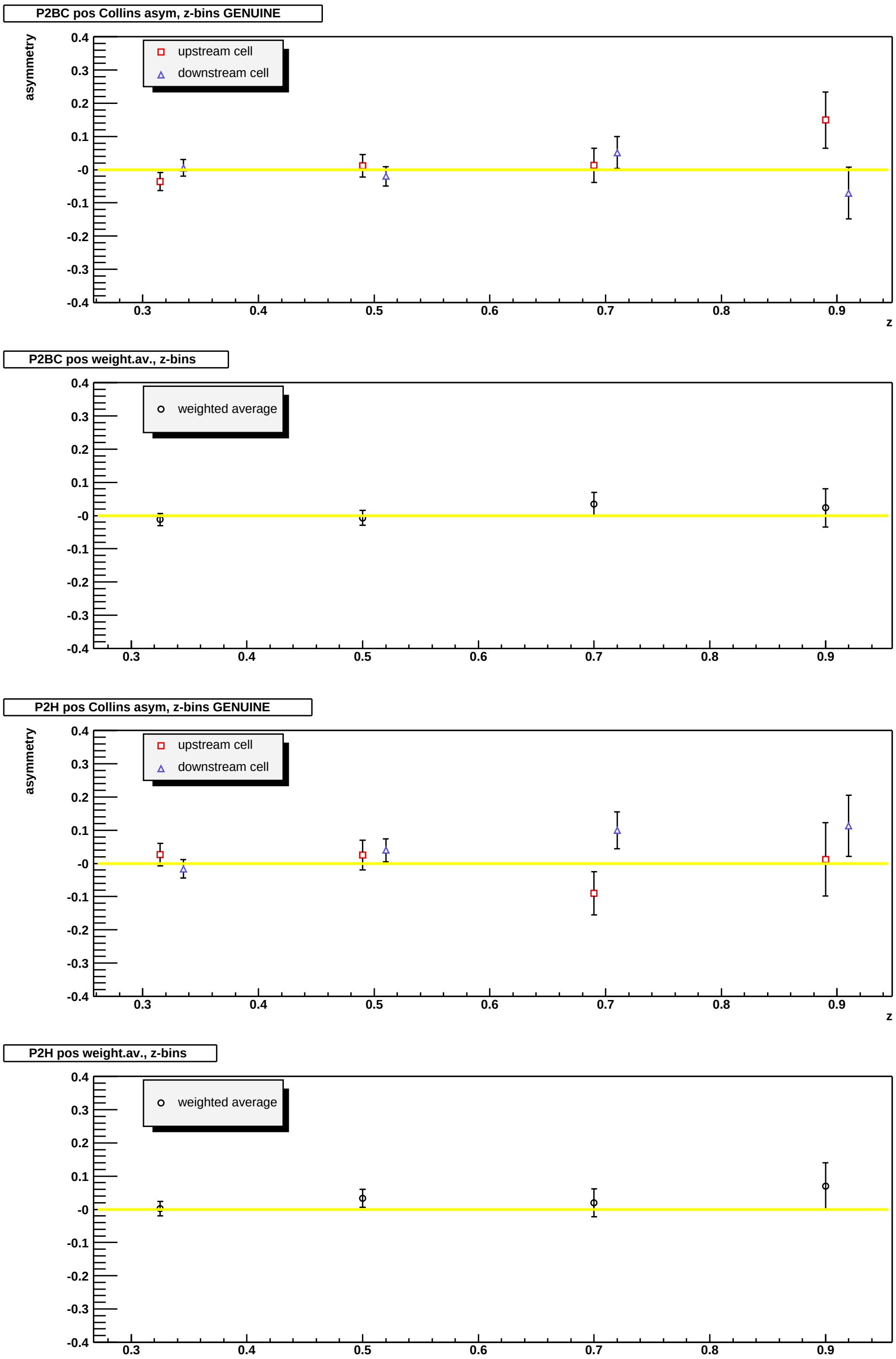

Figure 5.21: Collins Asymmetry from the COMPASS data 2002; positive leading hadrons, z-dependence:
(a) P2BC upstream, downstream target cell;
(b) P2BC weighted mean for both target cells;
(c) P2H upstream, downstream target cell;
(d) P2H weighted mean for both target cells.

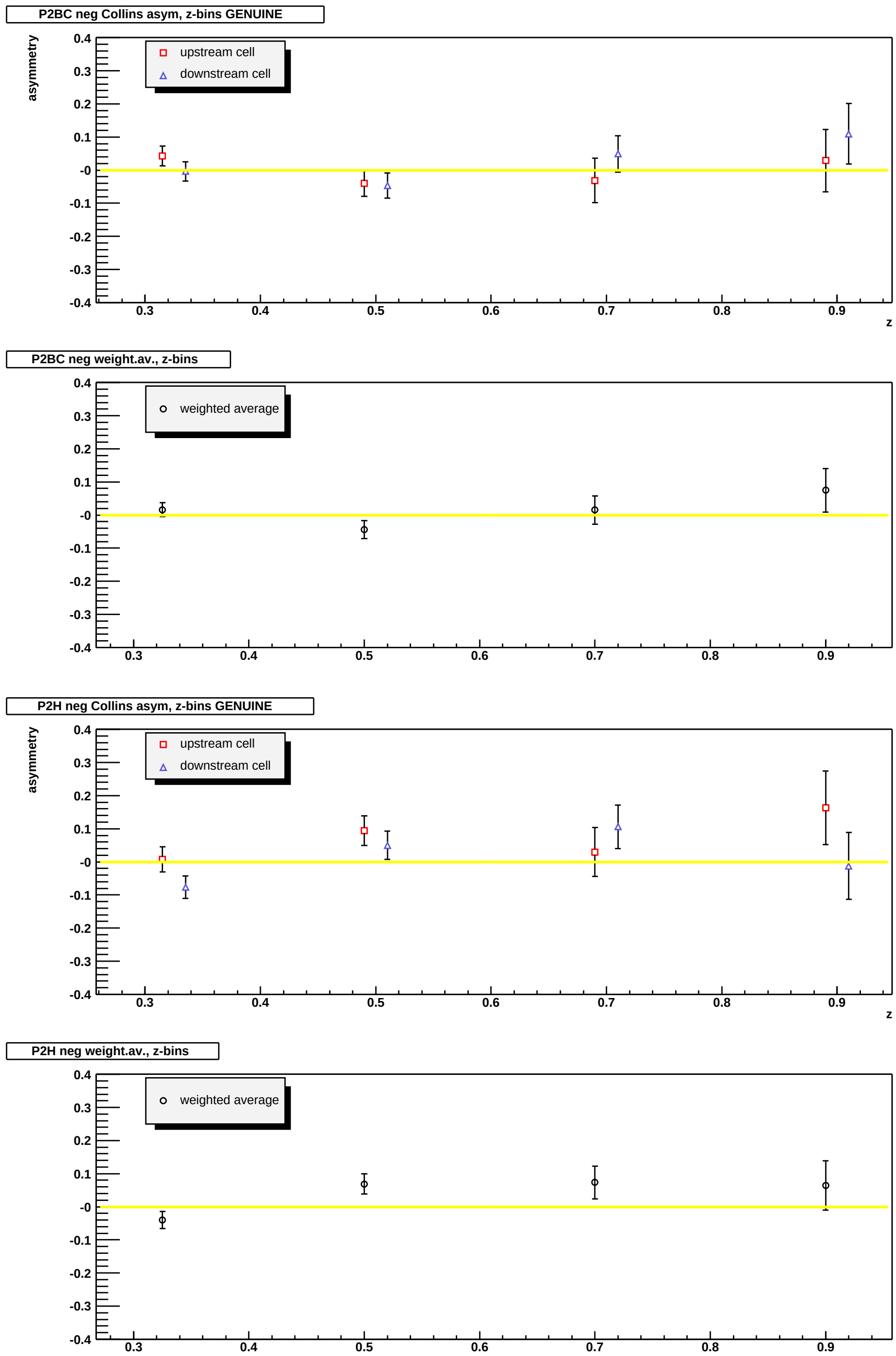

Figure 5.22: Collins Asymmetry from the COMPASS data 2002; negative leading hadrons, z-dependence:
(a) P2BC upstream, downstream target cell;
(b) P2BC weighted mean for both target cells;
(c) P2H upstream, downstream target cell;
(d) P2H weighted mean for both target cells.

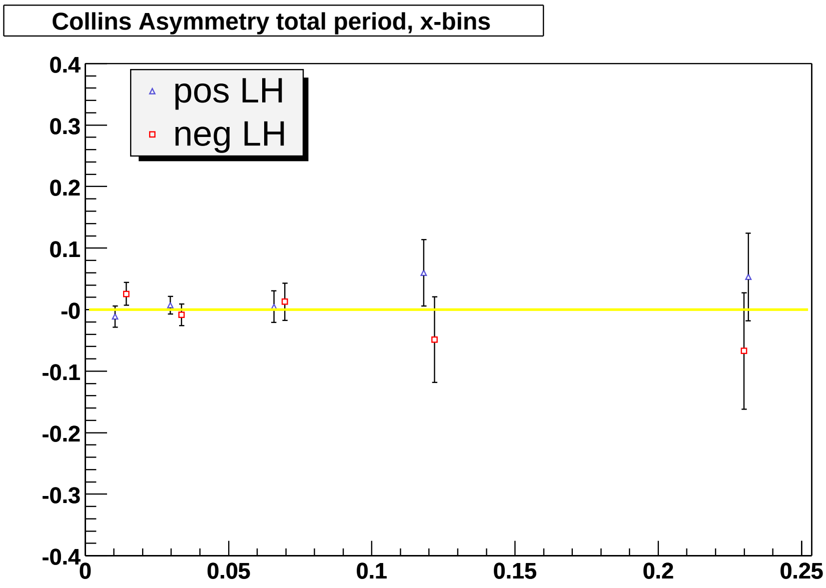

Figure 5.23: Collins asymmetry; all transverse data 2002, x-dependence.

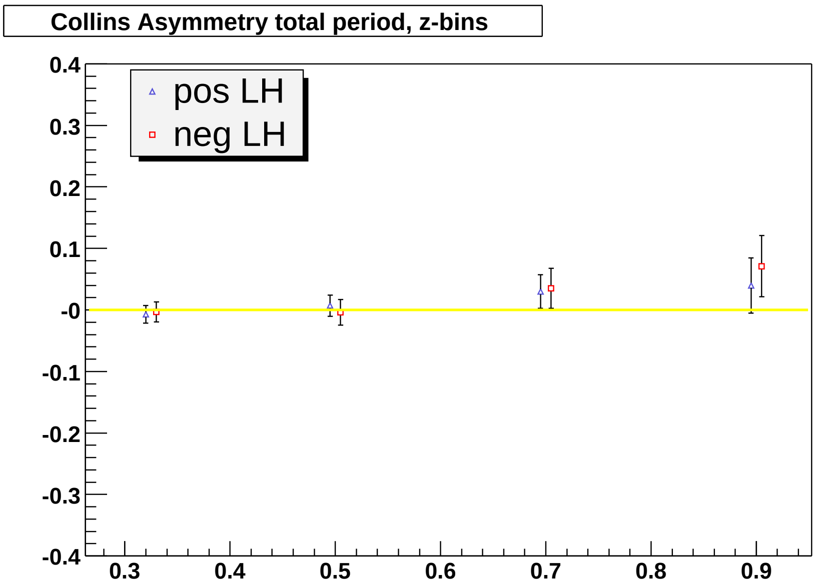

Figure 5.24: Collins asymmetry; all transverse data 2002, z-dependence.

the further normalisation (5.21). The weighting factor is given simply by the sum of events in both target cells (N_{up} and N_{down}) in each of the first periods[4]

$$N^{P2BC} = N_{up}^{P2B} + N_{down}^{P2B} \tag{5.22}$$

$$N^{P2H} = N_{up}^{P2H.1} + N_{down}^{P2H.1} \tag{5.23}$$

The statistical error σ^{comb} on the combined asymmetry can be calculated accordingly from the statistical error on the period asymmetries $\sigma^{P2BC}, \sigma^{P2H}$ through

$$\sigma^{comb} = \frac{\sqrt{(N^{P2BC} \cdot \sigma^{P2BC})^2 + (N^{P2H} \cdot \sigma^{P2H})^2}}{N^{P2BC} + N^{P2H}}. \tag{5.24}$$

The Collins asymmetries for all transverse data from the COMPASS beam-time in 2002 are to be found in Tables 5.7 and 5.8. The corresponding graphs can be seen in Figures 5.23 (x-bins) and 5.24 (z-bins).

x	pos			neg		
0-0.02	-0.011	±	0.017	0.025	±	0.019
0.02-0.05	0.007	±	0.014	-0.008	±	0.018
0.05-0.10	0.005	±	0.026	0.013	±	0.031
0.10-0.15	0.060	±	0.054	-0.049	±	0.070
0.15-1.0	0.053	±	0.071	-0.067	±	0.094

Table 5.7: Collins asymmetry; all transverse data 2002, positive/negative leading hadrons, x-dependence.

z	pos			neg		
0.25-0.4	-0.007	±	0.014	-0.003	±	0.016
0.4-0.6	0.007	±	0.017	-0.004	±	0.021
0.6-0.8	0.030	±	0.027	0.035	±	0.033
0.8-1.0	0.040	±	0.045	0.071	±	0.050

Table 5.8: Collins asymmetry; all transverse data 2002, positive/negative leading hadrons, z-dependence.

5.7 Estimation of the Systematic Errors

5.7.1 Stability of the Normalisation

In (5.13) it is assumed that the normalisation factor is given solely by the ratio of the number of events between the two data periods under comparison. A

[4] The arguments x or z of σ and N is dropped for clarity; the weighting is however performed separately for each x-and z-bin.

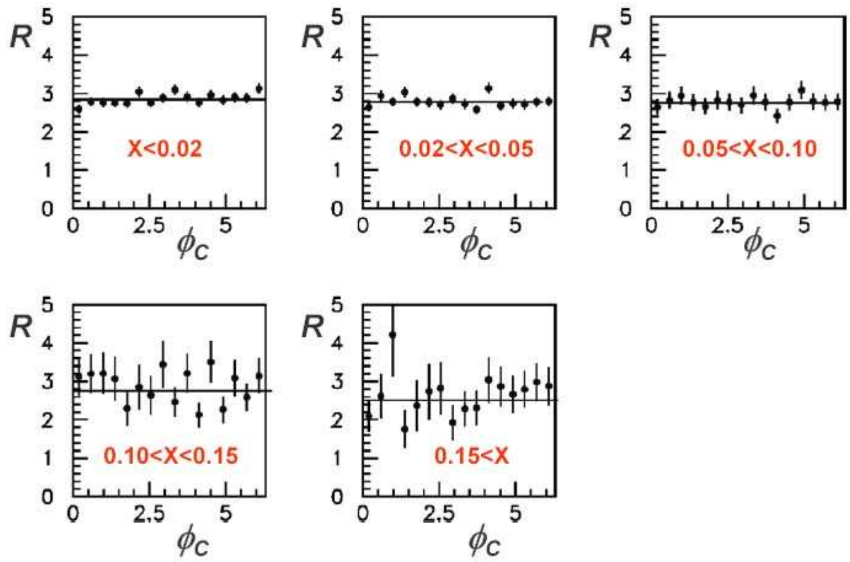

Figure 5.25: The combined counting-rate ratio shows no dependence on ϕ_C; acceptance effects are to a large extent avoided by the measurement method with two target cells.

possible dependence of this factor on ϕ_C caused by acceptance effects (the fact that the spectrometer is not uniformly sensitive to events occurring at different angles) was not considered. The extent to which this assumption is justified can be estimated starting from the ratio of acceptances α of the two target cells, which is assumed to be constant over two periods. Thus

$$\frac{\alpha_d^{P2B}(\phi_c)}{\alpha_u^{P2B}(\phi_c)} = \frac{\alpha_d^{P2C}(\phi_c)}{\alpha_u^{P2C}(\phi_c)} \tag{5.25}$$

where u (d) indicates the upstream (downstream) target cell. The number of events N in a target cell in one period is proportional to the acceptance in that target cell, so that the combined counting-rate ratio R from the numbers of events in both target cells for a pair of periods can be written

$$R(\phi_C) = \frac{N_u^{P2C} \cdot N_d^{P2C}}{N_u^{P2B} \cdot N_d^{P2B}} \propto \left[\frac{\alpha_u^{P2C}(\phi_c)}{\alpha_u^{P2B}(\phi_c)}\right]^2 . \tag{5.26}$$

The nearer R is to a constant over the whole spectrum of ϕ_c, the smaller the systematic acceptance effects are, and the more justifiable the original assumption was. Figure 5.25 shows that the initial assumption was indeed justified within the bounds of error.

5.7.2 "Washed-out" Asymmetries

A further estimation of the systematic errors introduced by acceptance effects or longer-term variations in the beam or target may be achieved by considering a data-sample in which no or a negligible asymmetry is to be expected. A simple way of gaining such a comparison sample from the existing data is to take not just leading hadrons, but all outgoing particles of the primary vertex for the calculation of the asymmetry. The cut on the variable z is loosened from $z > 0.25$ to $z > 0$ and the standard kinematic variables and the Collins angle are calculated for all non-muonic particles emanating from the primary vertex. The asymmetries are as before calculated from the counting-rate differences between two periods for different bins in ϕ_C and x or z. They should be, if not zero, then starkly reduced, since *a priori* no asymmetry is expected from particles of low energy. Theoretical considerations exist that the hadron from the primary vertex with the second-largest energy contribution (the *sub-leading hadron*), could even cancel out all or part of the asymmetry of the leading hadron [39]. The data-points calculated using all hadrons are indeed all very close to zero, suggesting that the systematic error in the values for the Collins asymmetry is small. More extensive investigations of the systematics and the still somewhat unclear theoretical situation regarding the sub-leading hadron are still being performed. Tables 5.9 and 5.10 contain the values for the asymmetries averaged for all periods and both target cells.

x	pos			neg		
0-0.02	-0.008	$\pm$	0.004	0.009	$\pm$	0.004
0.02-0.05	-0.002	$\pm$	0.004	0.004	$\pm$	0.005
0.05-0.10	0.001	$\pm$	0.008	0.000(5)	$\pm$	0.009
0.10-0.15	0.010	$\pm$	0.018	-0.028	$\pm$	0.018
0.15-1.0	0.007	$\pm$	0.023	-0.004	$\pm$	0.025

Table 5.9: False asymmetries from the 2002 COMPASS data; all transverse data, positive/negative leading hadrons, x-bins.

z	pos			neg		
0.25-0.4	-0.006	$\pm$	0.003	0.007	$\pm$	0.003
0.4-0.6	0.003	$\pm$	0.008	-0.005	$\pm$	0.010
0.6-0.8	0.014	$\pm$	0.013	0.014	$\pm$	0.015
0.8-1.0	0.021	$\pm$	0.021	0.034	$\pm$	0.024

Table 5.10: False asymmetries from the 2002 COMPASS data; all transverse data, positive/negative leading hadrons, z-bins.

5.8 Comparison Results

In parallel to the analysis contained in this thesis, independent analyses of the transverse data from the COMPASS beam-time in 2002 were performed in Bonn and Trieste. For the publication of the results for the Collins asymmetry at COMPASS, the standard cuts described in the preceding sections were agreed. The data-samples themselves were slightly different in the three analyses, mainly as a result of slightly different approximations used in the calculation

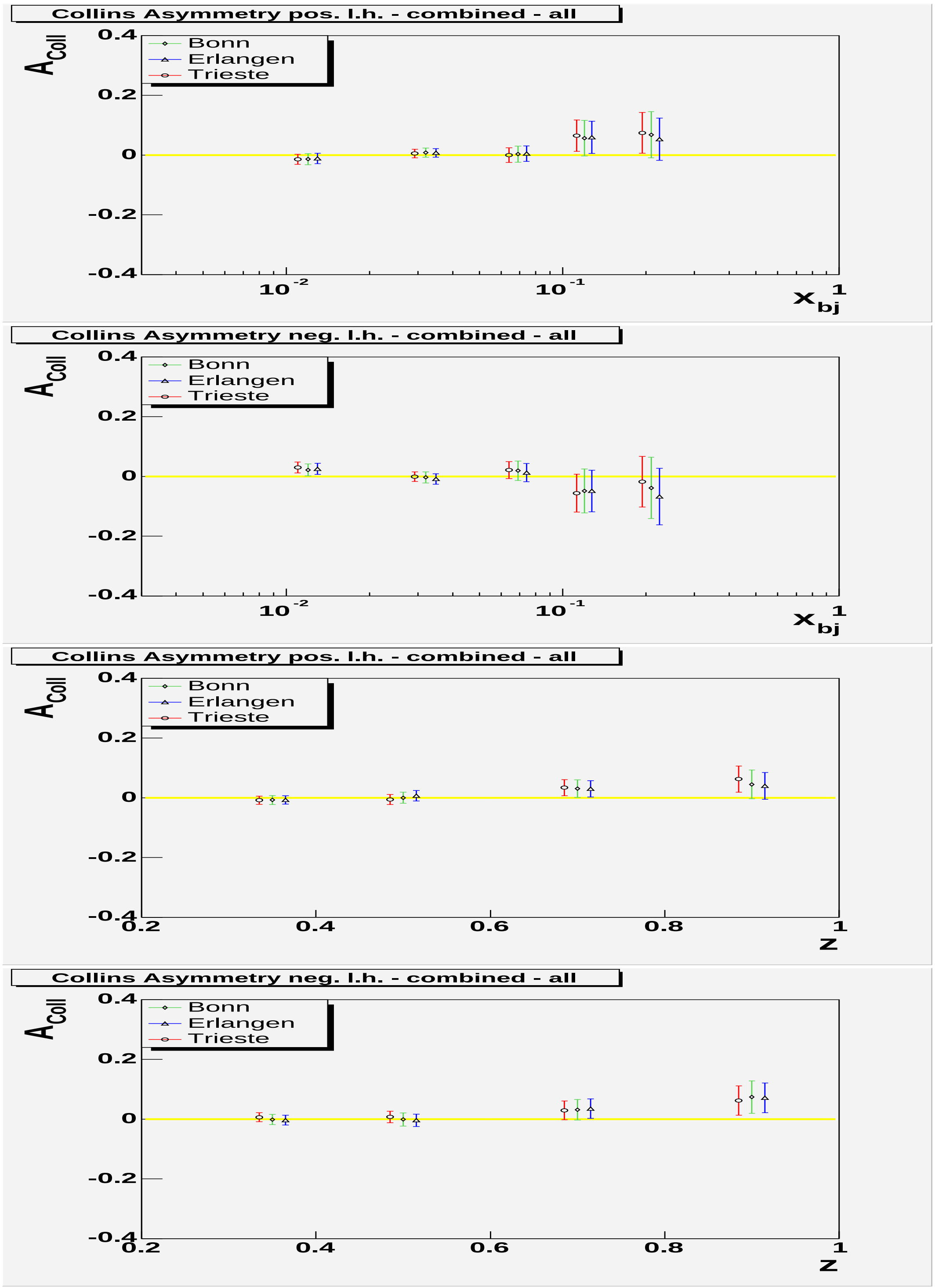

Figure 5.26: Comparison Results for the Collins asymmetry for the Collins Asymmetry from all COMPASS data 2002:
(a) positive leading hadrons, x-dependence;
(b) negative leading hadrons, x-dependence;
(c) positive leading hadrons, z-dependence;
(d) negative leading hadrons, z-dependence.
.

of the kinematic variables; those events not common to all three constituted however less than 1% of the total. The normalisations and fit procedures employed were also minimally different. The results from the three analyses can be found together in Figure 5.26. Clearly all three results are in very good agreement.

5.9 Statistical Error-Bounds on the 2003 Data

The first production of the data from the two transverse data-taking periods of the COMPASS beam-time 2003 was performed early in 2004. In the first period, 2003-P1G (target polarisation $\Downarrow\Uparrow$), 234 runs were taken (c.f. 145 runs (P2B) and 64 runs (P2H.1) in 2002); in the second period, 2003-P1H (target polarisation $\Uparrow\Downarrow$) 217 runs (c.f. 145 runs (P2C) and 112 runs (P2H.2)). Since the second period followed on immediately from the first, it is expected that they may be combined without any problems. The first glance at the 2003 data shows that among other things an optimised trigger (in particular new elements in the outer trigger covering the high-Q^2 region important for the transversity analysis (c.f. Figure 3.13)), should bring better statistics. Per run of 100 spills, approximately 77% more events with $Q^2 > 1$ can be expected. After all standard cuts, around 62% more events are expected. This increase it at its greatest in the region of high x_{Bj}.

Table 5.11 shows the statistical error on the Collins asymmetry from these data in the most favourable case (i.e., with no loss of data in stability checks).

	2002		2003		2002 + 2003	
	pos	neg	pos	neg	pos	neg
x_{Bj}						
0.003 - 0.02	0.017	0.019	0.016	0.016	0.012	0.012
0.02 - 0.05	0.014	0.018	0.012	0.014	0.009	0.011
0.05 - 0.10	0.026	0.031	0.021	0.024	0.016	0.019
0.10 - 0.15	0.054	0.070	0.039	0.050	0.032	0.041
0.15 - 0.8	0.071	0.094	0.050	0.058	0.040	0.049
z						
0.25-0.4	0.014	0.016	0.012	0.013	0.009	0.010
0.4-0.6	0.017	0.021	0.014	0.018	0.011	0.014
0.6-0.8	0.027	0.033	0.022	0.026	0.017	0.020
0.8-1.0	0.045	0.050	0.036	0.039	0.028	0.031

Table 5.11: Expected statistical error on the Collins asymmetry from the 2002 data, the 2003 data and both sets of data together, for positive and negative leading hadrons.

Chapter 6

Conclusion and Outlook

The first contribution to the COMPASS experiment reported on in this thesis consisted of the commissioning of scintillating-fibre hodoscopes and their integration into the experiment. In this context, program routines were written for their monitoring during beam-time and for their calibration and the calculation of their detection efficiency.

The SciFi hodoscopes are shown through the analysis in this thesis to be highly effective and reliable detectors. The summed time during which individual channels did not function properly came in the 2003 beam-time to much less that 1% of the physics data-taking time. The detector channels exhibited timing variations of not more than 100 ps, as shown by analysis of the calibration data; thus it is possible to deliver reliable timing information with a relatively sparse calibration density.

The intrinsic efficiency of the SciFi stations, defined as the probability of a single event being detected, is almost 100%. At full beam intensity, the effective efficiency varies from 97-99% according to the plane. Together with their excellent time-resolution of around 400 ps and their high-rate capability, this makes the SciFis ideally suited for their task of detecting scattered muons in the beam-region of the COMPASS experiment.

The second contribution reported in this thesis was the analysis of the data taken with transverse spin configuration during the COMPASS beam-time in 2002. This centred on the extraction of the so-called Collins asymmetry which should appear at higher values of the kinematic variables x and z in the distribution of the azimuthal angle of production of the most energetic hadron in a deep-inelastic scattering event. Through this effect, access should be possible to the previously unknown transversely polarised quark distribution functions $\Delta_T q_i(x)$.

The data taken in the total of three weeks' transverse data-taking proved with a few exceptions to be stable at the point of production. This was shown through analysis of the stability of kinematic variables and reconstruction variables, as well as through the K_s^0 mass-peak reconstruction. The data periods P2B/P2C on the one hand and P2H.1/P2H.2 on the other were found however to be incompatible and had to be analysed separately. The values for the asymmetries from the two pairs of periods were combined as a weighted mean at the end of the analysis process.

Through kinematic and other cuts, a deep-inelastic data-sample with a reliably identified leading hadron could be collected. Because of the COMPASS kinematics, the region of high x where the asymmetry should deliver a non-zero value is sparsely occupied. The asymmetries were calculated by comparing the counting-rates in two periods with opposite polarisation for both target cells, and then weighted and combined with each other, first according to target cell and then according to period. The asymmetries were extracted separately for positive and negative leading hadrons.

The data from the COMPASS beam-time 2002 yield no clear evidence for a non-zero Collins asymmetry in the kinematic range covered. All data-points are compatible with zero at the 1-2 σ level. A slight tendency to positive values for positive leading hadrons and to negative values with negative leading hadrons at higher values of x is possibly indicated,but the large error-bars make a concrete assertion impossible. These error-bars should be reduced significantly with data from the 2003 beam-time.

Further data will be taken at COMPASS in the prolonged beam-time in 2004. Following SPS-stop in 2005, the new COMPASS magnet with its much higher acceptance should allow much higher statistics at large x. These data should allow unambiguous conclusions to be drawn as to the nature of the Collins effect.

Appendix A

Event Selection for Extraction of the Collins Asymmetry

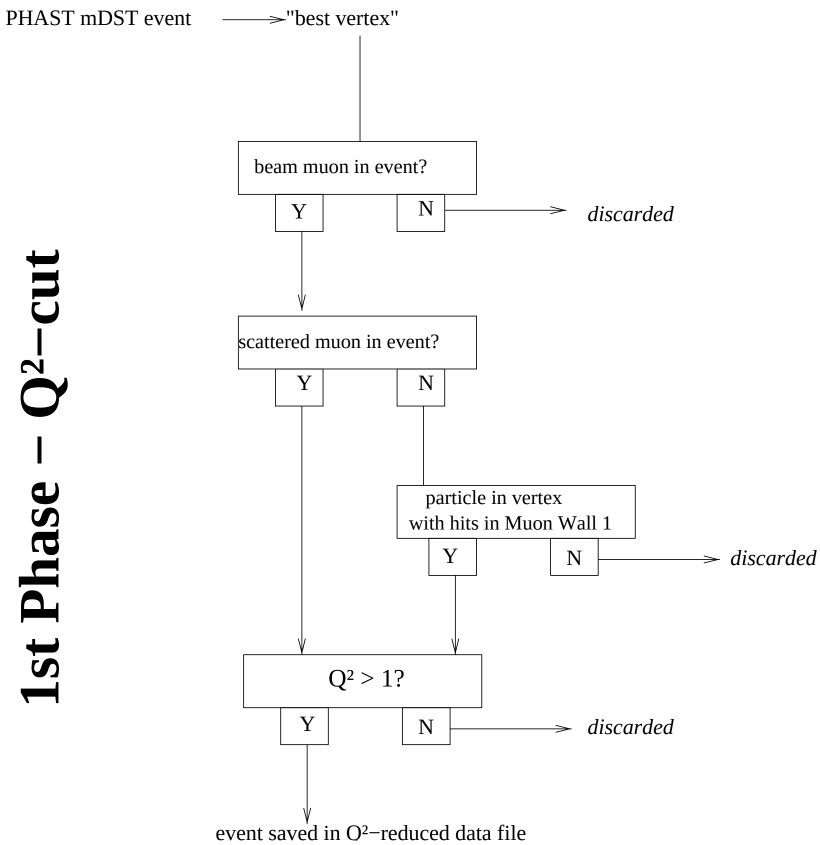

Figure A.1: Schematic depiction of the first phase of the Collins effect event-selection. Primary vertices with beam and scattered muons present are sought. If $Q^2 > 1$, the event is stored to a reduced data-file.

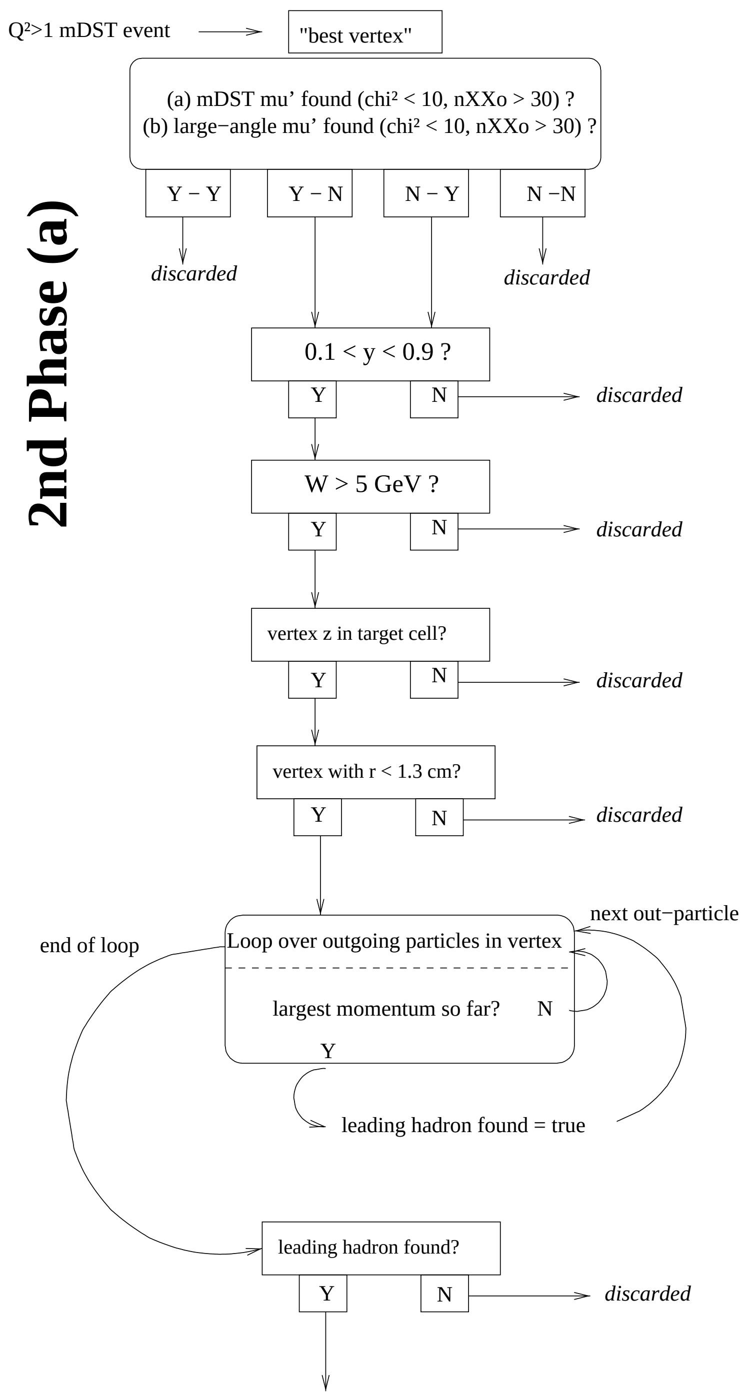

Figure A.2: Schematic depiction of the second phase of the Collins effect event-selection: nXX_0-, y-,W- and target cuts and selection of the leading hadron.

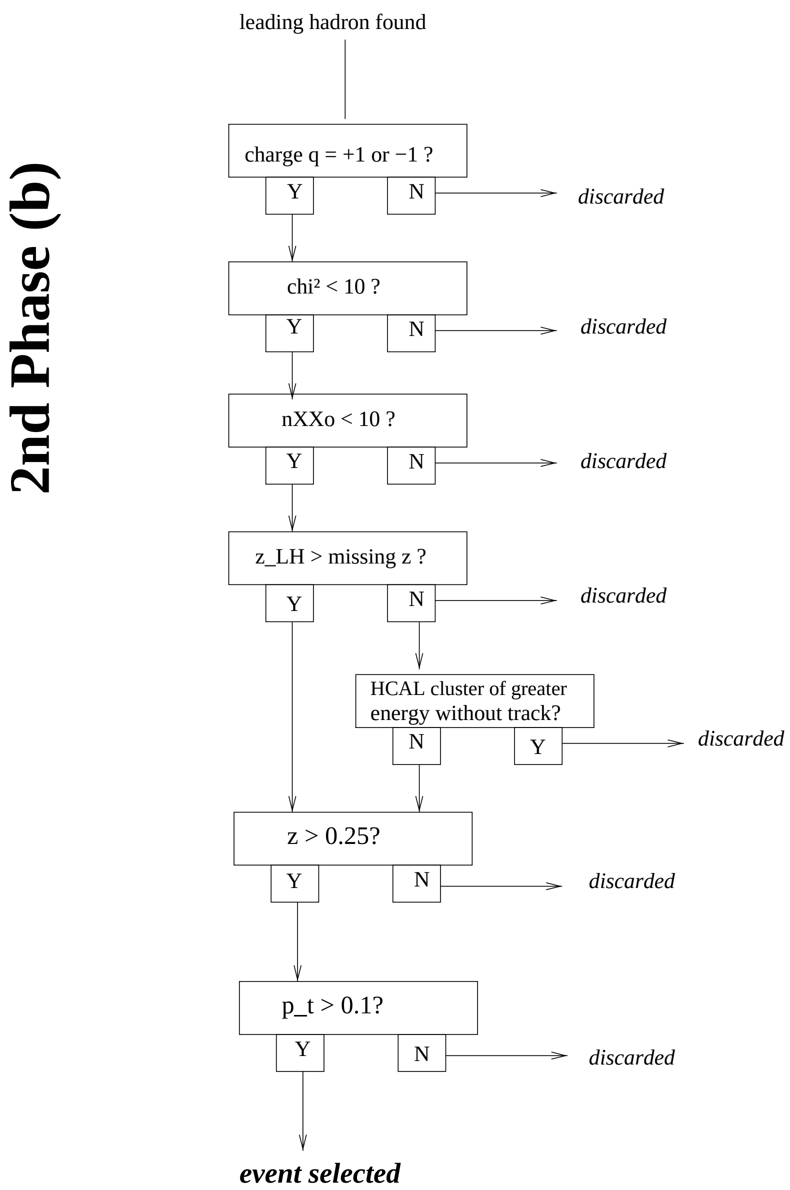

Figure A.3: Schematic depiction of the second phase of the Collins effect event-selection (continued): cuts on the leading hadron.

Appendix B

Collins Data-Sample in x- and z-bins; Scaling Factors

P2B $\Downarrow\Uparrow$	upstream				downstream			
x	pos	%	neg	%	pos	%	neg	%
$0-0.02$	45229	43.83	38231	45.34	5017	38.22	46314	41.17
$0.02-0.05$	42324	41.01	33828	40.14	60351	41.92	46416	41.26
$0.05-0.10$	11785	11.43	9363	11.11	20707	14.38	14605	12.98
$0.10-0.15$	2235	2.17	1719	2.04	4621	3.21	3077	2.74
$0.15-1$	1625	1.57	1144	1.36	3262	2.27	2092	1.86

P2C $\Uparrow\Downarrow$	upstream				downstream			
x	pos	%	neg	%	pos	%	neg	%
$0-0.02$	49012	43.85	40650	44.86	59687	38.15	49770	40.72
$0.02-0.05$	45433	40.65	36448	40.23	65369	41.78	50233	41.10
$0.05-0.10$	13021	11.65	10185	11.24	22351	14.29	16424	13.44
$0.10-0.15$	2603	2.33	1967	2.17	5252	3.36	3427	2.80
$0.15-1$	1704	1.52	1360	1.50	3788	2.42	2358	1.93

P2H.1 $\Downarrow\Uparrow$	upstream				downstream			
x	pos	%	neg	%	pos	%	neg	%
$0-0.02$	24271	43.64	20644	45.14	29359	38.23	25111	41.36
$0.02-0.05$	22059	39.66	17861	39.06	31005	40.36	24222	39.90
$0.05-0.10$	6936	12.47	5381	11.77	11562	15.05	8209	13.52
$0.10-0.15$	1460	2.63	1173	2.56	2882	3.75	1908	3.14
$0.15-1$	888	1.59	673	1.47	2011	2.62	1262	2.08

P2H.2 $\Uparrow\Downarrow$	upstream				downstream			
x	pos	%	neg	%	pos	%	neg	%
$0-0.02$	41790	43.89	35302	45.13	50306	38.65	42200	41.15
$0.02-0.05$	37656	39.55	30527	39.03	52366	40.23	40629	39.62
$0.05-0.10$	11752	12.34	9285	11.87	19341	14.86	14132	13.78
$0.10-0.15$	2547	2.67	1945	2.49	4867	3.74	3396	3.31
$0.15-1$	1478	1.55	1158	1.48	3274	2.52	2187	2.13

Table B.1: Division of the final sample into x-bins, separated for period and charge of the leading hadron.

P2B $\Downarrow\Uparrow$	upstream				downstream			
z	pos	%	neg	%	pos	%	neg	%
$0.25 - 0.4$	51480	49.88	45097	53.51	71968	49.99	59208	52.63
$0.4 - 0.6$	32787	31.77	25430	30.17	46249	32.13	34869	30.99
$0.6 - 0.8$	13272	12.86	9934	11.79	18116	12.58	13247	11.77
$0.8 - 1$	5659	5.48	3824	4.54	7625	5.30	5180	4.60
P2C $\Uparrow\Downarrow$	upstream				downstream			
z	pos	%	neg	%	pos	%	neg	%
$0.25 - 0.4$	55758	49.89	48109	53.09	77570	49.58	64135	52.48
$0.4 - 0.6$	35320	31.60	27705	30.58	50315	32.16	38084	31.16
$0.6 - 0.8$	14334	12.82	10559	11.65	20109	12.85	14423	11.80
$0.8 - 1$	6361	5.69	4237	4.68	8453	5.40	5570	4.56
P2H.1 $\Downarrow\Uparrow$	upstream				downstream			
z	pos	%	neg	%	pos	%	neg	%
$0.25 - 0.4$	27756	49.91	24251	53.03	38239	49.78	31807	52.39
$0.4 - 0.6$	17636	31.71	13936	30.47	24825	32.32	19023	31.33
$0.6 - 0.8$	7080	12.73	5241	11.46	9635	12.54	7042	11.60
$0.8 - 1$	3142	5.65	2304	5.04	4120	5.36	2840	4.68
P2H.2 $\Uparrow\Downarrow$	upstream				downstream			
z	pos	%	neg	%	pos	%	neg	%
$0.25 - 0.4$	48047	50.46	41505	53.06	65310	50.18	53789	52.45
$0.4 - 0.6$	29785	31.28	23853	30.50	41552	31.93	31780	30.99
$0.6 - 0.8$	12053	12.66	9051	11.57	16295	12.52	12002	11.70
$0.8 - 1$	5338	5.61	3808	4.87	6997	5.38	4973	4.85

Table B.2: Division of the final sample into z-bins, separated for period and charge of the leading hadron.

x	0 - 0.02	0.02-0.05	0.05-0.10	0.10-0.15	0.15-1
P2BC pos					
up 0	6.78223	5.73056	5.56918	5.54306	5.63816
down 0	7.14349	6.0184	5.81619	5.79495	5.79194
up 1	6.76309	5.7166	5.56771	5.55536	5.67642
down 1	7.1514	6.00642	5.79956	5.76631	5.79817
up 2	6.74231	5.71042	5.54781	5.56458	5.67624
down 2	7.15427	6.00953	5.79598	5.78155	5.81604
up 3	6.78267	5.71758	5.54686	5.58229	5.56531
down 3	7.18551	6.01568	5.79834	5.78383	5.76775
up 4	6.779	5.71521	5.56138	5.62149	5.70858
down 4	7.15173	6.01077	5.81083	5.81302	5.78386
up 5	6.80316	5.72998	5.59379	5.71125	5.84219
down 5	7.16125	6.00931	5.82631	5.78189	5.85723
up 6	6.76706	5.73121	5.60596	5.72899	5.94223
down 6	7.16325	6.01466	5.8244	5.80888	5.85443
up 7	6.75185	5.73861	5.60507	5.63564	5.73088
down 7	7.14169	6.00306	5.82075	5.79041	5.82827
P2H pos					
up 0	7.04682	5.87967	5.687	5.68084	5.7773
down 0	7.14638	5.91826	5.71448	5.64999	5.65718
up 1	7.04256	5.86514	5.69275	5.66896	5.88653
down 1	7.17688	5.9181	5.70447	5.64651	5.6235
up 2	7.08097	5.85362	5.68055	5.6886	5.72093
down 2	7.19651	5.92102	5.70347	5.62459	5.63109
up 3	7.1133	5.85092	5.66765	5.6483	5.65027
down 3	7.17347	5.92581	5.70121	5.65315	5.6157
up 4	7.13914	5.86393	5.66235	5.64966	5.72634
down 4	7.23132	5.91594	5.7179	5.64245	5.6682
up 5	7.07147	5.87267	5.70004	5.83555	6.01839
down 5	7.18212	5.92705	5.70133	5.6689	5.73929
up 6	7.0836	5.87544	5.72886	5.85162	6.08515
down 6	7.15495	5.91114	5.70806	5.70014	5.72247
up 7	7.05173	5.89053	5.71358	5.73352	6.00157
down 7	7.14572	5.91622	5.70314	5.67349	5.71663

Table B.3: Scaling factor $1/(D_{NN} \cdot f \cdot P)$ from raw to Collins asymmetry for positive leading hadrons: from left to right x-bins; from top to bottom eight (uniformly wide) bins in ϕ_C from $-\pi$ to $+\pi$ for upstream und downstream target cells.

x	0 - 0.02	0.02-0.05	0.05-0.10	0.10-0.15	0.15-1
P2BC neg					
up 0	6.78187	5.73556	5.54695	5.52452	5.56303
down 0	7.15476	6.01648	5.81255	5.76942	5.7525
up 1	6.78769	5.71316	5.5575	5.50356	5.53959
down 1	7.17686	6.01562	5.81345	5.77837	5.79042
up 2	6.795	5.70899	5.53434	5.51994	5.51001
down 2	7.17538	6.02176	5.79652	5.75912	5.76114
up 3	6.78712	5.69589	5.53343	5.49939	5.52231
down 3	7.18628	6.00797	5.81131	5.78149	5.75148
up 4	6.76033	5.70849	5.55882	5.63336	5.66392
down 4	7.1258	6.01068	5.79778	5.79638	5.78382
up 5	6.71996	5.71189	5.58633	5.66572	5.86313
down 5	7.1116	6.00445	5.80172	5.79828	5.83076
up 6	6.71538	5.73657	5.6246	5.77621	5.92015
down 6	7.0998	6.00645	5.81339	5.80658	5.83404
up 7	6.73255	5.73464	5.5641	5.59475	5.68515
down 7	7.13968	6.01238	5.81517	5.77854	5.79912
P2H neg					
up 0	7.02563	5.86606	5.67626	5.63463	5.68954
down 0	7.14832	5.92031	5.70657	5.67865	5.67822
up 1	7.08664	5.8659	5.66821	5.62846	5.62196
down 1	7.20039	5.92949	5.70475	5.6435	5.65821
up 2	7.11034	5.86396	5.65461	5.60851	5.58126
down 2	7.15776	5.92308	5.69388	5.6267	5.63054
up 3	7.06263	5.85484	5.64625	5.60059	5.63617
down 3	7.19712	5.92328	5.70052	5.639	5.62237
up 4	7.04732	5.84993	5.66268	5.65347	5.76656
down 4	7.13357	5.92867	5.69775	5.65932	5.68556
up 5	6.99289	5.86208	5.71286	5.80658	6.0746
down 5	7.10976	5.92408	5.70908	5.63915	5.68282
up 6	7.00051	5.87883	5.73711	5.86854	6.13333
down 6	7.13959	5.91816	5.71096	5.67466	5.81255
up 7	7.0453	5.8802	5.72906	5.70097	5.81423
down 7	7.13284	5.93211	5.7086	5.68506	5.71819

Table B.4: Scaling factor $1/(D_{NN} \cdot f \cdot P)$ from raw to Collins asymmetry for negative leading hadrons: from left to right x-bins; from top to bottom eight (uniformly wide) bins in ϕ_C from $-\pi$ to $+\pi$ for upstream und downstream target cells.

z	0.25-0.4	0.4-0.6	0.6-0.8	0.8-1.0
P2BC pos				
up 0	6.05701	5.95695	5.95985	6.17977
down 0	6.45346	6.36513	6.36252	6.60447
up 1	6.02056	5.95066	5.94582	6.05921
down 1	6.43043	6.3728	6.35288	6.55847
up 2	6.01733	5.88883	5.91821	6.00777
down 2	6.4332	6.37238	6.38834	6.46527
up 3	6.00996	5.92174	5.92224	6.20814
down 3	6.44466	6.36983	6.385	6.65051
up 4	6.02168	5.93054	5.92756	6.3542
down 4	6.4256	6.36548	6.39769	6.84016
up 5	6.06023	5.94587	5.97288	6.52117
down 5	6.42999	6.33434	6.40795	6.95326
up 6	6.06217	5.93807	5.99855	6.49519
down 6	6.43485	6.3602	6.36906	6.98801
up 7	6.06662	5.96346	5.94669	6.30995
down 7	6.42796	6.34848	6.3653	6.80584
P2H pos				
up 0	6.24159	6.13178	6.14105	6.38586
down 0	6.38074	6.29526	6.28506	6.55972
up 1	6.2225	6.11066	6.09697	6.24918
down 1	6.38309	6.27281	6.32579	6.46964
up 2	6.21451	6.10304	6.09015	6.21973
down 2	6.35815	6.29882	6.33774	6.51152
up 3	6.17381	6.08166	6.13082	6.63847
down 3	6.35092	6.30829	6.33281	6.70922
up 4	6.21598	6.10941	6.20944	6.85244
down 4	6.35794	6.27881	6.32888	7.0865
up 5	6.21638	6.12774	6.16826	6.89157
down 5	6.3978	6.2681	6.31489	7.01953
up 6	6.25929	6.12726	6.20046	6.75649
down 6	6.37052	6.28829	6.28197	6.86045
up 7	6.28413	6.14796	6.10701	6.61108
down 7	6.36262	6.29976	6.2701	6.752

Table B.5: Scaling factor $1/(D_{NN} \cdot f \cdot P)$ from raw to Collins asymmetry for positive leading hadrons: from left to right z-bins; from top to bottom eight (uniformly wide) bins in ϕ_C from $-\pi$ to $+\pi$ for upstream und downstream target cells.

z	0.25-0.4	0.4-0.6	0.6-0.8	0.8-1.0
P2BC neg				
up 0	6.06168	5.97957	5.98978	5.88976
down 0	6.48126	6.43086	6.38469	6.32516
up 1	6.02938	5.96467	5.98045	5.91896
down 1	6.49137	6.42692	6.40729	6.36027
up 2	6.0016	5.9515	5.96111	5.87341
down 2	6.4715	6.42527	6.45092	6.3674
up 3	6.0063	5.95191	5.95773	5.84165
down 3	6.47564	6.41815	6.43128	6.39636
up 4	6.04968	5.9716	5.95041	5.85979
down 4	6.47542	6.41704	6.38187	6.36952
up 5	6.0711	5.97865	5.92807	5.92686
down 5	6.4851	6.40248	6.38943	6.31191
up 6	6.11104	6.00661	5.97342	5.85499
down 6	6.47487	6.41906	6.3732	6.37853
up 7	6.08161	6.00085	5.94184	5.86042
down 7	6.49572	6.43105	6.37287	6.30882
P2H neg				
up 0	6.24902	6.14575	6.12062	6.04329
down 0	6.43211	6.35097	6.3373	6.28501
up 1	6.23445	6.15053	6.17395	6.05162
down 1	6.41197	6.37917	6.37568	6.31975
up 2	6.22417	6.17244	6.17521	6.02933
down 2	6.40496	6.34524	6.36189	6.27093
up 3	6.21163	6.11946	6.12827	6.01706
down 3	6.42536	6.35074	6.34992	6.27155
up 4	6.22824	6.17156	6.11761	5.98876
down 4	6.40743	6.35324	6.33948	6.25818
up 5	6.27163	6.17454	6.10058	6.0073
down 5	6.42261	6.37447	6.28822	6.23942
up 6	6.30327	6.17829	6.11379	6.06366
down 6	6.4662	6.36614	6.28328	6.25225
up 7	6.32172	6.15983	6.1285	6.04654
down 7	6.44221	6.33268	6.36854	6.33158

Table B.6: Scaling factor $1/(D_{NN} \cdot f \cdot P)$ from raw to Collins asymmetry for negative leading hadrons: from left to right z-bins; from top to bottom eight (uniformly wide) bins in ϕ_C from $-\pi$ to $+\pi$ for upstream und downstream target cells.

Appendix C

Collins Asymmetry: Numerical Values

The following 24 asymmetries were calculated and are shown in the following:

	Period	**LH charge**		(a)	(b)	(c)
1	P2BC	pos	x	upstream	downstream	average
2	P2H	pos	x	upstream	downstream	average
3	P2BC	neg	x	upstream	downstream	average
4	P2H	neg	x	upstream	downstream	average
5	P2BC	pos	z	upstream	downstream	average
6	P2H	pos	z	upstream	downstream	average
7	P2BC	neg	z	upstream	downstream	average
8	P2H	neg	z	upstream	downstream	average

1,2	(a) upstream			(b) downstream			(c) weighted mean		
P2BC pos x									
0 - 0.02	-0.018	$\pm$	0.033	-0.021	$\pm$	0.031	-0.020	$\pm$	0.022
0.02-0.05	0.002	$\pm$	0.027	-0.003	$\pm$	0.025	-0.001	$\pm$	0.018
0.05-0.10	-0.018	$\pm$	0.053	-0.010	$\pm$	0.045	-0.013	$\pm$	0.035
0.10-0.15	0.074	$\pm$	0.132	0.056	$\pm$	0.089	0.062	$\pm$	0.074
0.15-1.0	0.130	$\pm$	0.161	0.054	$\pm$	0.116	0.078	$\pm$	0.094
P2H pos x									
0 - 0.02	-0.044	$\pm$	0.039	0.044	$\pm$	0.037	0.004	$\pm$	0.027
0.02-0.05	0.051	$\pm$	0.034	0.004	$\pm$	0.029	0.024	$\pm$	0.022
0.05-0.10	0.031	$\pm$	0.057	0.040	$\pm$	0.048	0.036	$\pm$	0.037
0.10-0.15	0.132	$\pm$	0.132	0.018	$\pm$	0.093	0.057	$\pm$	0.076
0.15-1.0	-0.204	$\pm$	0.187	0.106	$\pm$	0.128	0.011	$\pm$	0.106

Table C.1: Collins asymmetry from the 2002 COMPASS data; positive leading hadrons, x-bins.

	upstream			downstream			weighted mean		
P2BC neg x									
0 - 0.02	0.004	$\pm$	0.035	-0.000(3)	$\pm$	0.035	0.001	$\pm$	0.024
0.02-0.05	0.030	$\pm$	0.033	-0.025	$\pm$	0.032	-0.002	$\pm$	0.023
0.05-0.10	0.017	$\pm$	0.060	0.016	$\pm$	0.054	0.016	$\pm$	0.040
0.10-0.15	0.038	$\pm$	0.145	-0.025	$\pm$	0.129	-0.002	$\pm$	0.096
0.15-1.0	-0.188	$\pm$	0.227	0.065	$\pm$	0.158	-0.026	$\pm$	0.129
P2H neg x									
0 - 0.02	0.098	$\pm$	0.041	0.047	$\pm$	0.038	0.070	$\pm$	0.027
0.02-0.05	-0.034	$\pm$	0.037	-0.012	$\pm$	0.034	-0.021	$\pm$	0.025
0.05-0.10	0.194	$\pm$	0.072	-0.117	$\pm$	0.058	0.006	$\pm$	0.045
0.10-0.15	-0.082	$\pm$	0.150	-0.144	$\pm$	0.125	-0.121	$\pm$	0.096
0.15-1.0	-0.221	$\pm$	0.228	-0.091	$\pm$	0.159	-0.136	$\pm$	0.130

Table C.2: Collins asymmetry from the 2002 COMPASS data; negative leading hadrons, x-bins.

	upstream			downstream			weighted mean		
P2BC pos z									
0.25 - 0.4	-0.036	$\pm$	0.027	0.005	$\pm$	0.025	-0.012	$\pm$	0.018
0.4 - 0.6	0.012	$\pm$	0.034	-0.020	$\pm$	0.030	-0.007	$\pm$	0.022
0.6 - 0.8	0.013	$\pm$	0.052	0.051	$\pm$	0.048	0.035	$\pm$	0.035
0.8 - 1	0.149	$\pm$	0.085	-0.070	$\pm$	0.078	0.024	$\pm$	0.058
P2H pos z									
0.25 - 0.4	0.027	$\pm$	0.034	-0.016	$\pm$	0.027	0.002	$\pm$	0.021
0.4 - 0.6	0.025	$\pm$	0.045	0.040	$\pm$	0.034	0.033	$\pm$	0.027
0.6 - 0.8	-0.089	$\pm$	0.065	0.100	$\pm$	0.056	0.020	$\pm$	0.042
0.8 - 1	0.012	$\pm$	0.110	0.113	$\pm$	0.092	0.069	$\pm$	0.071

Table C.3: Collins asymmetry from the 2002 COMPASS data; positive leading hadrons, z-bins.

	upstream			downstream			weighted mean		
P2BC neg z									
0.25 - 0.4	0.043	$\pm$	0.030	-0.004	$\pm$	0.029	0.016	$\pm$	0.021
0.4-0.6	-0.040	$\pm$	0.039	-0.047	$\pm$	0.038	-0.044	$\pm$	0.027
0.6-0.8	-0.031	$\pm$	0.067	0.049	$\pm$	0.055	0.0150	$\pm$	0.042
0.8-1	0.029	$\pm$	0.094	0.110	$\pm$	0.091	0.0749	$\pm$	0.065
P2H neg z									
0.25 - 0.4	0.0071	$\pm$	0.038	-0.076	$\pm$	0.034	-0.040	$\pm$	0.025
0.4-0.6	0.095	$\pm$	0.045	0.050	$\pm$	0.042	0.069	$\pm$	0.031
0.6-0.8	0.030	$\pm$	0.074	0.106	$\pm$	0.066	0.073	$\pm$	0.049
0.8-1	0.163	$\pm$	0.111	-0.012	$\pm$	0.101	0.065	$\pm$	0.074

Table C.4: Collins asymmetry from the 2002 COMPASS data; negative leading hadrons, z-bins.

Bibliography

[1] F. Halzen and A.D. Martin. *Quarks and leptons : an introduction course in modern particle physics*. John Wiley & Sons, 1984.

[2] R.G. Roberts. *The Structure of the Proton: Deep Inelastic Scattering*. Cambridge University Press, 1990. Cambridge Monographs on Mathematical Physics.

[3] Jörg Pretz. *Messung der polarisierten Quarkverteilungen in semi-inklusiver Myon-Nukleon Streuung*. PhD thesis, Fachbereich Physik der Johannes Gutenberg-Universität Mainz, 1997.

[4] Mario Leberig. *Das COMPASS Triggersystem zur Messung von ΔG*. PhD thesis, Fachbereich Physik der Johannes Gutenberg-Universität Mainz, 2002.

[5] L.G. Greeniaus. Deep inelastic scattering with spin, June 2001. Lectures presented for the Troisieme Cycle de la Physique en Suisse Romande.

[6] J.D. Bjø rken. Inelastic electron-proton and gamma-proton scattering and the structure of the nucleon. *Physical Review*, 185(5), 1969.

[7] Richard P. Feynman. Very high-energy collisions of hadrons. *Physical Review Letters*, 23(24), 1969.

[8] M. Gell-Mann. A schematic model of baryons and mesons. *Physics Letters*, (8):214, 1964.

[9] C. Zweig. An SU3 model for strong interaction symmetry and its breaking. *CERN Report*, TH(401,412), 1964.

[10] Leader E. Anselmino M., Efremov A. The theory and phenomenology of polarized deep inelastic scattering. *Phys. Rep*, (261):1, 1995.

[11] John Ellis and Robert Jaffe. Sum rule for deep inelastic electroproductions from polarized protons. *Physical Review D*, 9(5), 1974.

[12] J. Ashman et al. A measurement of the spin asymmetry and determination of the structure function g_1 in deep inelastic muon-proton scatering. *Phys. Letters*, B(206):364, 1988.

[13] J. Ashman et al. An investigation of the spin structure of the proton in deep inelastic scattering of polarised muons on polarised protons. *Nuclear Physics*, B(328):1, 1989.

[14] B. Adeva et al. Next-to-leading order QCD analysis of the spin structure function g_1. *Physical Review D*, 58(112002), 1998.

[15] C. Adloff et al. Deep inelasitc inclusive e p scattering at low x and a determination of α_s. *Europ. Phys. J.*, C(21):33, 2001.

[16] A. Simon et al. Recent spin physics results from the HERMES experiment. *Nucl. Phys.*, B(86):112, 2000.

[17] The Compass Collaboration. *COMPASS - a proposal for a Common Muon and Proton Apparatus for Structure and Spectroscopy*. CERN, spsc/p 297 edition, March 1996.

[18] D. von Harrach. The COMPASS experiment at CERN. *Nucl. Phys.*, A(629):245, 1998.

[19] A. Bravar et al. Large gluon polarization from correlated high p_t hadron pairs in polarized electro-production. *Phys. Lett.*, B(421):349, 1998.

[20] NuPECC. Long range plan, 2002. Chapter 'QCD'.

[21] P Barone V. und Ratcliffe. *Transverse Spin Physics*. World Scientific, 2003.

[22] Xiangdong Ji Jaffe R.L. Chiral-odd parton distributions and drell-yan processes. *Nucl. Phys.*, B(375):521–560, 1996.

[23] Tangerman R.D. Mulders P.J. The complete tree-level result up to order 1/q for polarized deep-inelastic leptoproduction. *Nucl. Phys.*, B(461):197–237, 1996.

[24] C. Berger. *Teilchenphysik: Eine Einführung*. Springer-Verlag, 1992.

[25] R. Jaffe. Transversity: A primer, 2000. Riken/BNL Research Center Workshop on Transversity.

[26] Soffer J. Positivity constraints for spin-dependent parton distribution functions. *Phys. Rev. Lett.*, 74:1292–1296, 1995.

[27] S. Aoki et al. Tensor charge of the nucleon in lattice QCD. *Phys.Rev. D*, 56:433–436, 1997.

[28] He Ji. *Phys.Rev. D*, 52:2960, 1995.

[29] A. Ioffe, B.L. und Khodjamiraian. *Phys.Rev. D*, 51:3373, 1995.

[30] Goeke K. Hyun-Chul Kim, Polyakov M.V. Tensor charges of the nucleon in the SU(3) chiral quark soliton model. *Phys. Lett*, B(387):577–581, 1996.

[31] Bunce G.et al. Prospects for spin physics at RHIC. *Ann. Rev. Nucl. Part. Sci.*, 50:525–575, 2000.

[32] Hatanaka K. et al. Proceedings of the 14th international spin physics symposium, 2001. Contrib. von Goto, Y. p.442.

[33] M. Grosse Perdekamp. Transversity measurement with the PHENIX detector at RHIC, 2000. Proceedings of 8th International Workshop on Deep Inelastic Scattering and QCD, Liverpool.

[34] D.L. Adams et al. High x_t single spin asymmetry in pi0 and eta production at $x_f = 0$ by 200-gev polarized anti-protons and protons. *Phys. Lett.*, B(276):531–535, 1992.

[35] Bravar A. et al. Single-spin asymmetries in inclusive charged pion production by transversely polarized antiprotons. *Phys. Rev. Lett.*, 77(13):2626–2629, 1996.

[36] Dong H. et al. Energy dependence of the single spin asymmetries in inclusive pion production processes. *arXiv:hep-ph*, (0311121), 2003.

[37] Collins J. Fragmentation of transversely polarized quarks probed in transverse momentum distributions. *arXiv:hep-ph*, (0302008), 2003.

[38] Ladinsky G. Collins J., Heppelmann S. Measuring transversity densities in singly polarized hadron-hadron and lepton-hadron collisions. *Nucl. Phys.*, B(420):565–582, 1994.

[39] Yabuki H. Artru X., Czyzewski J. Single spin asymmetry in inclusive pion production, collins effect and the string model. *Zeitschrift für Physik*, C(73):527–534, 2003.

[40] Sivers D. Single-spin production asymmetries from the hard scattering of pointlike constituents. *Phys. Rev. D*, 41(1):83–90, 1991.

[41] A. Bravar. Hadron azimuthal distributions and transverse spin asymmetries in DIS of leptons off transversely polarized targets from smc. *Nucl. Phys.*, B(79):520–522, 1999.

[42] Airapetian A. et al. Evidence for a single-spin azimuthal asymmetry in semi-inclusive pion electroproduction. *Phys. Rev. Lett.*, 84(18):4047–4051, 2000.

[43] Avakian H. Azimuthal single-spin-asymmetries in semi-inclusive DIS from HERMES. *Nucl. Phys.*, B(79):523–525, 1999.

[44] Murgia F Anselmimo M. Spin effects in the fragmentation of a transversely polarized quark. *Phys. Lett.*, B(483):74, 2000.

[45] Schweitzer P. Efremov A., Goeke K. Azimuthal asymmetry in electroproduction of neutral pions in semi-inclusive DIS. *Phys. Lett.*, B(522):37–48, 2002.

[46] Schweitzer P. Efremov A., Goeke K. *erratum to* azimuthal asymmetry in electro-production of neutral pions in semi-inclusive DIS. *Phys. Lett.*, B(544):389–392, 2002.

[47] Schweitzer P. Efremov A., Goeke K. Collins effect and single spin azimuthal asymmetries in the HERMES and COMPASS experiments. *arXiv:hep-ph*, (0309209), 2003.

[48] Lao Gatignon. User guide for the m2 beam. http://gatignon.home.cern.ch/gatignon/M2manual.html.

[49] H.W. Atherton et al. Precise measurement of particle production by 400 GeV/c protons on beryllium targets / cern. *Yellow report*, 80, 07 1980.

[50] R.L. Garwin. Observations of the failure of conservation of parity and charge conjugation in meson decays: the magnetic moment of the free muon. *Phys. Rev.*, (105):1415, 1957.

[51] G. Backenstoss. Helicity of μ^- mesons from π-meson decay. *Phys. Rev. Lett.*, (6):415, 1961.

[52] N. Doble et al. The upgraded muon beam at the SPS. *Nuclear Instruments and Methods*, A(328):351, 1994.

[53] D. Adams et al. Measurement of the SMC muon beam polarisation using the asymmetry on the elastic scattering of polarised electrons. *Nuclear Instruments and Methods*, A(443):1, 2000.

[54] B. Adeva et al. Measurement of the polarisation of a high energy muon beam. *Nuclear Instruments and Methods*, A(343):363, 1998.

[55] J. Kyynärainen. The SMC polarized target. *Nuclear Instruments and Methods*, A(356):47, 1995.

[56] D. Adams et al. The polarized double cell target of the SMC. *Nuclear Instruments and Methods*, A(437):23, 1999.

[57] Jaakko Koivunniemi et al. Dilution refrigerator for COMPASS polarized target. *Physica*, B(284-288):2012–2013, 2000.

[58] G. Abragam and M. Goldman. Principles of dynamic nuclear polarisation. *Rep. Prog. Phys.*, (41):395, 1978.

[59] The COMPASS Target Group. *Online Target Documentation.* http://wwwcompass.cern.ch/compass/detector/target/, Nov 2002.

[60] Takabayashi et al. First results of the large COMPASS ^{6}LiD polarized target. *Nuclear Instruments and Methods*, 2003. Article in Press.

[61] Robert Marcus Wagner. Commisioning of silicon detectors for the COMPASS experiment at CERN. Diplomarbeit, Physik-Department E18 Technische Universtät München, 2001.

[62] A. Magnon et al. Tracking with 40x40 cm^2 Micromega detectors in the high energy, high luminosity COMPASS experiment. *Nuclear Instruments and Methods*, A(478):210–214, 2002.

[63] Fabienne Kunne et al. Micromegas as a large microstrip detector for the COMPASS experiment. *Nuclear Instruments and Methods*, A(469):133–146, 2001.

[64] F. Sauli et al. Performance of GEM detectors in high intensity particle beams. *Nuclear Instruments and Methods*, A(470):548–561, 2001.

[65] F. Sauli et al. Constructing, test and commissioning of the triple-GEM tracking detector for COMPASS. *Nuclear Instruments and Methods*, A(490):177–203, 2002.

[66] V.N Bychkov. Construction and manufacture of large size straw-chambers of the COMPASS spectrometer tracking system. *Particles and Nuclei Letters*, 2(111):64–73, 2002.

[67] Silvia Dalla Torre et al. The COMPASS RICH project. *Nuclear Instruments and Methods*, A(433):207–211, 1999.

[68] Fulvio Tessarotto et al. COMPASS RICH-1. *Nuclear Instruments and Methods*, A(478):340–343, 2002.

[69] Claus Grupen. *Teilchendetektoren*. BI Wissenschaftsverlag Mannheim Leipzig Wien Zürich, 1993.

[70] The Muon Trigger Group. *Muon Trigger Documentation*. http://wwwcompass.cern.ch, July 2002.

[71] Lars Schmitt et al. Statusbericht zum Datennahmesystem des COMPASS-Experiments am CERN, 1999.

[72] F.H. Heinsius et al. The COMPASS data acquisition system, 2001.

[73] Martin Freiherr von Hodenberg. A first reconstruction of COMPASS data. Diplomarbeit, Fakultät für Physik der Albert-Ludwigs-Universität Freiburg, 2002.

[74] Boris Grube. The trigger control system and the common gem and silicon readout for the COMPASS experiment. Diplomarbeit, Technische Universität München, 2001.

[75] G. Braun et al. TDC Chip and readout driver developments for COMPASS and LHC-experiments. *hep-ex*, (9810048), 1998.

[76] Horst Fischer. *CATCH Users manual (preliminary)*, 2001.

[77] The Alice Collaboration. *ALICE Date v3.5 Users guide*, 1999. Alice internal note INT-99-64.

[78] H. Fischer. Report of the offline coordinator, 2003. COMPASS Collaboration Meeting, Lisbon.

[79] Rene Brun. *ROOT - An object-oriented Data Analysis Framework*. CERN, 3.1c edition, September 2001.

[80] T.O. White. Scintillating fibres. *Nuclear Instruments and Methods*, A(273):820, 1988.

[81] Kuraray. *Scintillating Materials*, 1998. Produktkatalog.

[82] E. Gatti and V. Svelto. Theory of time resolution in scintillating counter : Experimental results. *Nuclear Instruments and Methods*, A(4):189, 1959.

[83] I Daito. Time resolution of multi-cladding scintillating fiber detector. *Nuclear Instruments and Methods*, A(433):587–591, 1999.

[84] Andreas Teufel. *Entwicklung und Bau von Hodoskopen aus szintillierenden Fasern für das COMPASS-Experiment*. PhD thesis, Physikalisches Institut der Friedrich-Alexander Universität Erlangen-Nürnberg, 1996.

[85] Joel Heersink. Investigation of the effects of magnetic fields on a multichannel photomultiplier and the construction and testing of a scintillating fibre hodoscope. Diplomarbeit, Physikalisches Institut der Friedrich-Alexander Universität Erlangen-Nürnberg, 2000.

[86] Friedrich Stinzing et al. A scintillating fibre hodoscope for high rate aplications. *Nuclear Instruments and Methods*, A(490):101–111, 2002.

[87] Ole Nähle. *Faserhodoskope im COMPASS Experiment zum Nachweis von Teilchenspuren innerhalb des Primärstrahls*. PhD thesis, Mathematisch-Naturwissenschaftliche Fakultät der Rheinischen Friedrich-Wilhelms-Universität Bonn, 2002.

[88] Hamamatsu. *Photomultiplier Tubes*, 1997. Produktkatalog.

[89] Marc Wagner. Entwicklung und Bau eines intermediären Szintillatorfaser-Hodoskops für COSY-TOF. Diplomarbeit, Physikalisches Institut der Friedrich-Alexander Universität Erlangen-Nürnberg, 1997.

[90] Teufel A. Improvement of scifi time resolution SciFis, 2004. COMPASS Note to be released.

[91] van der Waerden. B.L. *Die Grundlehren der mathematischen Wirtschaften 87: Mathematische Statistik*. Springer-Verlag, 1971.

[92] P. Pagano. Production and stability checks for year 2002 transversity data, 2003. COMPASS internal note.

[93] K. Schoenning. Study of the compass spectrometer performance using k_s^0 events. Diplomarbeit, Department of Radiation Science, University of Uppsala, 2003.

[94] K. Hagiwara. Review of particle physics. *Physical Review D*, 66(010001), 2002.

[95] Arneodo et al. Measurements of the u valence quark distribution function in the proton and u quark fragmentation functions. *Nucl. Phys. B*, (321):541, 1995.

[96] Bisplinghoff J. et al. Collins asymmetry from the 2002 COMPASS transversity data, 2004. COMPASS Release Note.

[97] Jean-Marc Le Goff. Plans for transversity measurement at COMPASS, 2002. QCD Ferrara 02.

[98] Martin A. Bradamante F. A method to compute the Collins angle in transversely polarised DIS, 2002. COMPASS Note 2002-5.

[99] K. Gustafsson. Computation of the dilution factor for the year 2002 COMPASS data, 2003. COMPASS Note 2003-3.

[100] P. Pagano. Status of transversity analysis, 2004. COMPASS Analyse-Meeting Januar.

Thanks...

Many people have contributed a great deal to the successful completion of my doctorate. In particular I would like to thank the people that follow.

- As is traditional and only right, firstly I would like to thank my supervisor, Prof. Wolfgang Eyrich, for the pleasant working atmosphere created by him and for his continual interest in the progess of my work. Even when this, with the beginning of the transversity analysis, entered what was for him as well *terra incognita* he was seldom short of good advice.

- My colleagues in Erlangen, past and present, are due a special thanks for the good professional and personal co-operation. To name names: Stefan Wirth, Fidi Stinzing, Marc Wagner, Wolfgang Schroeder, Cecilia Pizzolotto, Albert Lehmann und Luigi Pinna. Above all I would like to thank my "office-mate" and closest COMPASS colleague Andreas Teufel, not only for the first proof-reading of the original German version of this thesis, but more importantly for his constant helpfulness and support during my whole doctoral studies. His impressive calm and healthy optimism in what were for him in part difficult times were always exemplary.

- Prof. Jens Bisplinghoff and members of his research group at the University of Bonn, especially Ralf Ziegler and Ole Nähle are to be thanked especially for their company in the commissioning phase of COMPASS, which ensured that those weeks in Geneva were always, to use Ralf's phrase, "fast wie Urlaub" - "almost like being on holiday". Rainer Joosten, also from the University of Bonn, must as official "godfather" of my thesis be thanked for his frequent assistance which made the transversity analysis possible. His - always constructive - scepticism when faced with the absurdities of the daily life of the physicist brightened up many an otherwise cheerless evening in front of the computer screen at CERN.

- I would like to thank Prof. Franco Bradamante and the members of his research group, Anna Martin and especially Paolo Pagano, for the excellent cooperation in the course of the transversity analysis. Horst Fischer of the University of Freiburg as well always concerned himself above and beyond his office as "Offline-Coordinator" of COMPASS for our work and was a constant source of good ideas (and relevant facts extracted from his seemingly bottomless laptop).

- Finally I would like to thank the many people who actually have nothing to do with this work but without whose moral and practical support it would never have come this far. Above all that is my family, in particular my parents and my sister, who have always "been there for me", but also my friends at home (England), at home (Erlangen) and elsewhere. A heartfelt thanks to all.

Curriculum Vitae

Personal Details

Name	Webb
Forenames	Richard John
Date of Birth	16.10.1978
Place of Birth	Maidstone (Kent)/England
Parents	Anthony William Webb, teacher
	Diana Mary Webb, née Barron, university lecturer
Family status	single
Religion	none

School Education

1983-1986	St Philip's Church of England Infants' School, Maidstone
1986-1990	Southborough County Primary Junior School, Maidstone
1990-1991	Vinters Boys' High School, Maidstone
1991-1996	Maidstone Grammar School, Maidstone
	1994 General Certificate of Secondary Education (GCSE) in 13 subjects
	1996 A Levels in Latin, Mathematics, Physics and Politics

University Education

1996-2000	Imperial College of Science, Technology and Medicine, University of London: First Degree in Physics
	1998-99 ERASMUS exchange year at the University of Erlangen
	2000 Masters Degree M.Sci. "with 1st class Honours"
	2000 Rector's Prize for Scientific Communication
2000-	Doctorate at the University of Erlangen as part of the international COMPASS collaboration at CERN, Geneva
	2003 Prize of the German Academic Foreign Exchange Service (DAAD) for outstanding work as a foreign student

Work Experience

2000-	Research Assistant at the University of Erlangen
2002-	Teaching Assistant at the Vocational School for Clinical Assistants, Erlangen

Other Qualifications

2003	"Großes Deutsches Sprachdiplom" (certifying fluent written and spoken German) from the University of Munich/the Goethe Institut
2002-4	Correspondence course in Sub-Editing from the *National Council for the Training of Journalists*